SOLID-STATE DEVICES FOR DETECTION OF DNA, PROTEIN BIOMARKERS AND CELLS

by

WASEEM ASGHAR

Presented to the Faculty of the Graduate School of
The University of Texas at Arlington in Partial Fulfillment
of the Requirements
for the Degree of

DOCTOR OF PHILOSOPHY

THE UNIVERSITY OF TEXAS AT ARLINGTON
May 2012

ACKNOWLEDGEMENTS

First, I would like to thank my parents and family members for their support in every part of my life. I would like to express my deepest gratitude to my advisor, Dr. Samir M. Iqbal, for his guidance, encouragement and support in my research work as well as all the help that he provided me in preparing this dissertation. I am grateful to Dr. Young-tae Kim, Dr. Richard B. Timmons and Dr. Ali Raza Butt for their technical guidance at different stages of my research projects. I also thank Dr. Donald Butler, Dr. Jung-Chih Chiao, and Dr. Robert Magnusson for reviewing my dissertation and being on my doctoral committee.

I would like to thank my co-workers Yuan Wan, Azhar Ilyas, Sri Divya Vidyala, Jeyantt Sankaran, Chaudhary Amir Arafat, Joseph Billo, Chetan Bhuwania, Muhymin Islam, Arif Iftakher, Motasim Bellah, Melissa Johnson, Mohammud Noor, Priyanka Ramachandran, Swati Goyal, Hassan Shah, Ahmed Shahid, Deepika Tamuly, Srikanth Vasudevan for their advice and helpful discussions during my research work. A special thanks to Thanh Bui, Dennis Bueno and other staff at Nanotechnology Research and Teaching Facility for giving me trainings on cleanroom equipment and providing me technical help at different stages of my research projects. I would also like to acknowledge the staff members at Characterization Center For Materials And Biology (C^2MB), UT-Dallas cleanroom facility and University of North Texas cleanroom facility.

Above all, I am indebted to my GOD, “ALLAH”, who has blessed my life abundantly and given my life meaning and purpose.

March 8, 2012

ABSTRACT

SOLID-STATE DEVICES FOR DETECTION

OF DNA, PROTEIN BIOMARKERS

AND CELLS

Waseem Asghar, PhD

The University of Texas at Arlington, 2012

Supervising Professor: Samir M. Iqbal

Nanobiotechnology and BioMEMS have had tremendous impact on biosensing in the areas of cancer cell detection and therapeutics, disease diagnostics, proteomics and DNA analysis. Diseases are expressed on all levels including DNA, protein, cell and tissue. Therefore it is very critical to develop biosensors at each level. The power of the nanotechnology lies in the fact that we can fabricate devices on all scales from micro to nano.

This dissertation focuses on four areas: 1) Development of nanopore sensors for DNA analysis; 2) Development of micropore sensors for early detection of circulating tumor cells (CTCs) from whole blood; 3) Synthesis of nano-textured substrates for cancer isolation and tissue culture applications; 4) Fabrication of nanoscale break-junctions. All of these sensors are fabricated using standard silicon processing techniques. Pulsed plasma polymer deposition is also utilized to control the density of the biosensor surface charges. These devices are then used for efficient detection of DNA, proteins and cells, and can be potentially used in point-of-care systems. Overall, our designed biosensing platforms offer improved selectivity, yield and reliability. Novel approaches to nanopore shrinking are simple, reliable and do not change the material composition around the pore boundary. The micropores provide a direct interface to

distinguish CTCs from normal cell without requiring fluorescent dyes and surface functionalization. Nano-textured surfaces and break-junctions can be used for enhanced adhesion of cells and selective detection of proteins respectively.

TABLE OF CONTENTS

ACKNOWLEDGEMENTS iii

ABSTRACT iv

LIST OF ILLUSTRATIONS xi

LIST OF TABLES xxi

Chapter Page

1. INTRODUCTION 1

1.1 Structure of Dissertation 1

1.1.1 Introduction (Chapter 1) 1

1.1.2 Background and Literature Review (Chapter 2) 2

1.1.3 Nanopore Based Solid-State Sensors for DNA Analysis (Chapter 3) 2

1.1.4 Solid-state Micropore Sensors for Detection of Cancer Cells (Chapter 4) 3

1.1.5 Nanotextured Scaffold from Chicken Eggshells (Chapter 5) 3

1.1.6 Rapid Nano-manufacturing of Break-Junctions using Focused Ion Beam (FIB) and Electromigration (Chapter 6) 4

1.1.7 Future Research Directions (Chapter 7) 4

2. BACKGROUND AND LITERATURE REVIEW 5

2.1 DNA Sequencing and Analysis 5

2.1.1 Structure of DNA 5

2.1.2 DNA Sequencing and Analysis 5

2.2 Nanopore Biosensors for DNA and Protein Analysis 7

2.2.1 Nanopore Biosensors 7
2.2.2 Protein Nanopores 7
2.2.3 Solid-State Nanopores (SSNs) 10
2.2.4 Fabrication of Solid-State Nanopores 10
2.3 Detection of Circulating Tumor Cells (CTCs) 19
2.3.1 Metastasis 19
2.3.2 Circulating Tumor Cells (CTCs) 19
2.3.3 CTCs Detection Techniques 21
2.4 Nano-Textured Scaffolds and Surfaces 25
2.4.1 Nano-Patterning and Nano-Texturing 25
2.4.2 Cell Response to Textured Surfaces 26
2.5 Break-junctions 27
2.5.1 Break-junctions for Biosensing 27
2.5.2 Fabrication of Break-junctions 30
3. NANOPORE BASED SOLID-STATE SENSORS FOR DNA ANALYSIS 34
3.1 Thermal Shrinking of Solid-State Nanopores by Direct Heating 34
3.1.1 Introduction 34
3.1.2 Materials and Methods 36
3.1.3 Conclusions 43
3.2 Nanopore Shrinking with Pulsed Plasma Polymer Deposition 43
3.2.1 Introduction 43
3.2.2 Materials and Methods 45
3.2.3 Results and Discussion 47
3.2.4 Conclusions 58
3.3 Real-time Detection and Analysis of DNA Translocation using Graphical Processing Unit (GPU) 58

3.3.1 Introduction 58
3.3.2 Problem Statement 62
3.3.3 GPU Architecture 63
3.3.4 Why GPU for our Problem? 65
3.3.5 Design Challenges 66
3.3.6 System Overview 67
3.3.7 Pulse Detection Algorithms 68
3.3.8 Detailed Architecture 78
3.3.9 Implementation 80
3.3.10 Evaluation 81
3.3.11 Conclusion 88
4. SOLID-STATE MICROPORES FOR DETECTION OF CANCER CELLS 90
4.1 Introduction 90
4.2 Materials and Methods 91
4.2.1 Micropore Device Fabrication 92
4.2.2 Measurement Setup 94
4.2.3 Effects of Oxide Membrane Thickness 95
4.2.4 Primary Renal Cancer Cell Culture (Human Derived) 96
4.2.5 Isolation of Red Blood Cells (RBCs) and White Blood Cells (WBCs) from Bovine Blood 96
4.3 Results and Discussions 97
4.4 Conclusions 106
5. NANOTEXTURED SCAFFOLD FROM CHICKEN EGGSHELLS 108
5.1 Introduction 108
5.2 Materials and Methods 109
5.2.1 Synthesis of Chicken Eggshell Scaffold 109

5.2.2 Gold Sputtering for SEM Imaging....110

5.2.3 Energy-Dispersive X-ray Spectroscopy (EDS) and Composition Mapping....110

5.2.4 X-ray Diffraction Analysis for Chicken Eggshell Samples....110

5.2.5 Polydimethysiloxane Casting....110

5.2.6 Atomic Force Microscope (AFM) Surface Analysis....111

5.2.7 Human-derived Primary Immortalized Fibroblast Cell Culture....111

5.2.8 In vitro Fibroblast Cell Culture Studies and Laminin Coating on PDMS Scaffolds....111

5.2.9 Immunostaining of Human Fibroblast Cells....112

5.2.10 Laminin Staining....113

5.2.11 Cell Sample Preparation for SEM Imaging....113

5.3 Results and Discussions....113

5.3.1 Wet Etching of Chicken Eggshells....113

5.3.2 EDS Elemental Analysis and Mapping of Eggshell....115

5.3.3 XRD Crystal Analysis of Eggshell....118

5.3.4 Polymer Casting and AFM Analysis....119

5.3.5 Laminin Coating on PDMS Samples....121

5.3.6 In vitro Fibroblast Cell Growth....122

5.3.7 Cell Morphology on Flat and Nano-textured PDMS....124

5.4 Conclusions....125

6. RAPID NANO-MANUFACTURING OF BREAK-JUNCTIONS USING FOCUSED ION BEAM (FIB) AND ELECTROMIGRATION....126

6.1 Introduction....126

6.2 Materials and Methods....127

6.3 Results and Discussions....128

6.4 Conclusions 134

7. FUTURE RESEARCH DIRECTIONS 135

7.1 Introduction 135

7.2 Selective Detection of Epidermal Growth Factor Receptor (EGFR) using PPPF Nanopores 135

7.3 Selective Enumeration of CD4+ T Lymphocytes 137

7.4 Nano-Textured Surfaces for Efficient Cancer Detection and Cytology 139

REFERENCES 140

BIOGRAPHICAL INFORMATION 151

LIST OF ILLUSTRATIONS

Figure Page

2.1 Workflow of conventional Sanger DNA sequencing. Reprinted by the permission from Nature Publishing Group Ltd: Nature Biotechnology [12], copyright (2008) 6

2.2 Shows a typical α-HL protein nanopore is shown (right). And characteristic current pulses are shown at left. When target molecule passes through the nanopore, it give distinctive current blockage pulses. Reprinted by the permission from Nature Publishing Group Ltd: Nature Biotechnology [44], copyright (2008) 8

2.3 Shows current pulses of 10 events recorded from a mixture of equal molar concentrations of poly$(dA)_{100}$ and poly$(dC)_{100}$. The individual events are identified, on the basis of t_D (translocation time/pulse width). $\varkappa$ represents the confidence in the molecule identification, Reprinted by permission from PNAS [45], copyright (2000) 9

2.4 when perfect complementary target DNA translocates through the nanopore. (b) Translocation pulses when single base mismatch target DNA translocates through the pore. Reprinted by permission from Nature Publishing Group: Nature Biotechnology [34], copyright (2001) 10

2.5 Process flow of fabricating oxide membrane, used for ion/electron drilling. The process starts with a bare silicon wafer which is oxidized at a temperature > 900 ^{o}C. Resist is then applied to one side of the wafer. Photolithography, buffered hydrofluoric acid etching, acetone wash, and tetramethylammonium hydroxide (TMAH) etching completes the process flow [66]. Reprinted by permission from Springer, coypright (2011) 11

2.6 Etching rates of Si (h k l) planes in TMAH solution vs. TMAH concentration, T = 80 ^{o}C: Solid lines, T = 70 ^{o}C: Dotted lines. Reprinted by permission from Elsevier: Sensors and Actuators A: Physical [69], copyright (2001) 13

2.7 Etching rate of Si (h k l) planes in TMAH vs. TMAH+IPA concentration at 80 ^{o}C [69]. The plots shows that etch rate is reduced by addition of IPA into TMAH solution. Reprinted by permission from Elsevier: Sensors and Actuators A: Physical [69], copyright (2001) 14

2.8 Ion beam sculpting process. (a) Schematic showing the thin nitride membrane fabrication and 60 nm pore drilled using ion beam. (b) The feedback controlled ion beam milling setup. Reprinted by permission from Nature Publishing Group: Nature [62], copyright (2001) 15

2.9 (a) cross-sectional view of the nanopore and the membrane. (b) Scanning electron microscope image for the fabricated nanopore after oxidation. (c) Cross-sectional view of the nanopore under electron beam irradiation. (d-g) Sequence of micrographs show the electron beam induced shrinking process. The final nanopore diameter is 3 nm. Reprinted by permission from Nature Publishing Group: Nature Materials [64], copyright (2003) 16

2.10 Solid-state nanopore functionalized with hair-pin loop DNA probes. The diameter of the nanopore is reduced to 2 nm after probe attachment. Reprinted by permission from Nature Publishing Group: Nature Nanotechnology [55], copyright (2007) 18

2.11 Main steps involved in the development of metastases, Reprinted by permission from Elsevier: Cancer Letters [89], copyright (2007) 20

2.12 Different type of blood cells and their density in whole blood. Reprinted by permission from IEEE: IEEE Pulse [110], copyright (2011) 21

2.13 The blood from cancer patients is processed with different methods for CTCs isolation. Immunostaining for specific marker, FISH for genomic amplification and quantitative RT-PCR for specific DNA/RNA sequencing can be applied to CTCs. Printed with permission [111] 22

2.14 Different concentration of magnetic beads incubated with whole blood. The beads are attached with tumor cells. Reprinted with permission [112] 23

2.15 Setup for isolation of CTCs from whole blood using microchip technology. Reprinted with permission from Nature Publishing Group: Nature [122], copyright (2007) 25

2.16 Process flow to synthesize nano-textured PLGA scaffold with eliminated chemical change effects. Reprinted by permission from Elsevier: Biomaterials [132], copyright (2004) 27

2.17 Schematic of electrical conduction through single molecule chemically attached to two facing electrodes. Reprinted with permission [135]. 28

2.18 Setup for controlled mechanical bending to fabricate break-junctions. Reprinted by permission from American Institute of Physics: Applied Physics Letters [136], copyright (1995) 29

2.19 (a) Metallic line before electromigration. (b) Break-junction formed after electromigration. Reprinted by permission from American Institute of Physics: Applied Physics Letters [137], copyright (2005) 29

2.20 (a) Si chip after dry and wet chemical etching. (b) SEM image of two cantilevers connected by Au wire. Reprinted by permission from American Institute of Physics: Applied Physics Letters [136], copyright (1995) 30

2.21 FESEM micrographs of break-junctions (a) before and (b) after electromigration. Reprinted by permission from American Institute of Physics: Applied Physics Letters [138], copyright (1999) 31

2.22 Schematic showing the fabrication process of gold break-junctions using e-beam deposition. (1) Si wafer (2) Si dioxide (3) Si nitride (4) gold (5) e-beam deposited carbon electrode. Reprinted by permission from American Institute of Physics [139], copyright (1997) 32

2.23 SEM micrograph of two carbon electrodes fabricated with e-beam deposition. Reprinted by permission from American Institute of Physics [139], copyright (1997) 33

2.24 Process flow for the fabrication of step junctions. (a) After evaporation of first electrode/step layer. (b) After evaporation of second electrode layer/finger layer. The lift off was performed after evaporation of first electrode. Reprinted by permission from American Chemical Society: Nano Letters [140], copyright (2004) 33

3.1 Schematic shows the free standing oxide membrane having small pore drilled with FIB. Reprinted with permission [48] 37

3.2 EDS spectrum for oxide membrane is shown which confirms the presence of only Si and O. TEM micrograph shows the nanopore drilled in oxide membrane (Inset). Reprinted with permission [48] 38

3.3 (a) TEM micrograph of nanopore as drilled with FIB. Its diameter is ~250 nm. (b) After 5 minutes of thermal shrinking at 1150 ^{o}C. Nanopore diameter is ~150 nm. (c) After 10 minutes of thermal shrinking at 1150 ^{o}C. Nanopore diameter is ~20 nm. (d) After 10 minutes and 40 secs of thermal shrinking at 1150 ^{o}C. Nanopore diameter is ~3 nm. Reprinted with permission [48]] 39

3.4 (a) TEM micrograph of nanopore as drilled with FIB with diameter of ~270 nm. (b) Nanopore closed after 4 minutes of thermal shrinking at 1250 ^{o}C. Reprinted with permission [48] 39

3.5 (a) SEM micrograph of the nanopore as drilled with FIB in 300 nm thick oxide membrane. The nanopore diameter was ~300 nm. (b) Nanopore diameter increased to ~650 nm when processed at 1150 ^{o}C for 15 minutes. (c) Nanopore diameter was further increased to ~1.5 µm when processed at 1150 ^{o}C for 50 minutes. Reprinted with permission [48] 40

3.6 Plot shows the nanopore shrinking rates at different processing temperatures. The nanopore neither shrink nor expand at 900 ^{o}C. The nanopore shrinking rate increased with increasing processing temperature. Thermal shrinking processes show almost linear behavior at all temperatures. Reprinted with permission [48] 41

3.7 Process flow for nanopore fabrication. (a) oxidized Si chip. (b) After photolithography. (c) After BHF wet etching and acetone wash. (d) After TMAH anisotropic etching of Si. (e) Si chip after nanopore drilled with FIB. Reprinted with permission [49] 47

3.8 (a) FTIR spectrum of plasma polymerized MAA films. The duty cycle during this deposition was 3 ms on and 30 ms off (b) High resolution C(1s) spectra of polymer films obtained from plasma polymerization of MAA under Continuous Wave plasma (CW) and pulsed plasma conditions (on/off pulse plasma ratio of 1/5 and 3/30). Reprinted with permission [49]....49

3.9 Plot shows film thickness control with pulsed plasma deposition. The deposition of the polymer was linear with respect to time. Reprinted with permission [49] 50

3.10 (a) The starting nanopore diameter was 320 nm as fabricated with FIB. (b) After 12 minutes PPPF deposition (~160 nm diameter). (c) After 15 minutes PPPF deposition (~120 nm diameter). (d) After 18 minutes PPPF deposition (~80 nm diameter). SEM micrographs became blurry due to nonconductive nature of polymer. Reprinted with permission [49]....51

3.11 (a) AFM micrograph of the nanopore (300 nm) as fabricated with FIB. (b) After 8 minutes of PPPF deposition (~190 nm diameter). (c) After 13 minutes of PPPF deposition (~120 nm diameter). (d) After 21 minutes of PPPF deposition (~10 nm diameter). All scale bars are 200 nm. Reprinted with permission [49] 51

3.12 Shows the *I-V* current measurements with the PPPF deposition. The initial nanopore diameter was 180 nm. The nanopore diameter was reduced to 140, 100, 70, 30 and 10 nm after 3, 6, 8, 11 and 13 minutes of polymer deposition respectively. Reprinted with permission [49]....52

3.13 Shows the conductance plot for after successive deposition steps of PPPF deposition. The calculations are for 10 mV of applied potential and 1 M KCl concentration (blue dotted line). Measured data (red large dots) shows good fit to the model curve. The plot sows two regions of linear current behavior which was due to the conical geometry of the nanopore. Reprinted with permission [49] 54

3.14 Shows *I-V* characterization of 10 nm nanopore at KCl concentrations of 0.1 M (diamonds) and 1 M (circles). The current scaled linearly with the voltage at both of the salt concentrations. Reprinted with permission [49]....55

3.15 The plot shows the nanopore diameter (circles) and channel length (squares) with respect to PPPF deposition time. The starting nanopore diameter and channel length were 180 nm and 100 nm respectively. After approximately 4 minutes of deposition the channel length and diameter became equal in dimension. The measured current (triangles) also scaled almost linearly with the nanopore diameter which again

showed uniform deposition rate with time. Reprinted with permission [49] 56

3.16 Shows DNA translocation through the PPPF nanopore. Current blockades were seen when λ-DNA at was added to the *cis* compartment and 100 mV of applied potential was applied. The inset shows the baseline current before the introduction of λ-DNA. Reprinted with permission [49] 57

3.17 Overview of GPU application showing data copying from host to GPU memory, launching GPU kernel, and copying results back to the CPU memory. Reprinted by permission from Elsevier [168] 63

3.18 Shows the thread organization of the GPU. Threads are organized into blocks, while blocks are organized into grids. Reprinted by permission from Elsevier [168] 64

3.19 Shows the memory hierarchy of NVIDIA GPU. Reprinted by permission from Elsevier [168] 65

3.20 Shows flow diagram of GPU-enabled pulse detection in the data flood created by biosensors when DNA is translocated through the solid-state nanopore. The resulting scatter plot is used for decision making regarding presence of specific genes and biomarkers. Reprinted by permission from Elsevier [168] 66

3.21 Shows high-level overview of the software components of our system. Reprinted by permission from Elsevier [168] 68

3.22 Shows the date preparation algorithm. Reprinted by permission from Elsevier [168] 69

3.23 Shows the flow chart for pulse detection algorithm(s). Reprinted by permission from Elsevier [168] 70

3.24 Shows parallel version of detection algorithms: Each thread calculates the initial threshold, and detects peaks in its chunk. Reprinted by permission from Elsevier [168] 71

3.25 Shows algorithm for fixed threshold technique. Reprinted by permission from Elsevier [168] 73

3.26 Shows the algorithm for baseline tracker technique. Reprinted by permission from Elsevier [168] 75

3.27 Shows algorithm for rolling average technique. Reprinted by permission from Elsevier [168] 77

3.28 Shows the pulses detected in 120 million points of data using Moving Average technique; Threshold is kept 1596 nano-Amperes below baseline, window size kept is 500 points, minimum acceptable width is

5 micro-Amperes, and maximum acceptable width is 100 micro-Amperes. Reprinted by permission from Elsevier [168] 80

3.29 Shows the plots for static and dynamic threshold (baseline-tracker) techniques, (a) static threshold (selected 1000 nanoamperes below baseline) cannot detect pulses when the baseline is very noisy. (b) baseline-tracker technique shows how it keeps track of the baseline. Reprinted by permission from Elsevier [168].....83

3.30 Shows the plots of moving average without Roll-back technique, tolerance: 0.3% (1143 nano-amperes below baseline), sampling rate of data: 75 µseconds, tracking for window size: (a) window-size: 750 µses, (b) window-size: 900 µses without rolling-back on data-points. Reprinted by permission from Elsevier [168].....84

3.31 Shows the comparison of manual detection with automated approach. (a) Static technique vs. manual approach, (b) baseline-tracker technique vs. manual approach, (c) Moving Average vs. manual approach. Reprinted by permission from Elsevier [168].....86

4.1 Shows the process flow of solid-state micropore fabrication. (a) After oxidation of Si wafer. (b) After photolithography, square window is opened in photoresist. (c) After BHF etching, pattern is transferred to oxide. (d) After TMAH wet etching. (e) Cross-section view of the pyramid structure holding oxide membrane. (f) After FIB drilling to make micropores in thin oxide membranes. Reprinted by permission of The Royal Society of Chemistry [179] 93

4.2 Shows the solid state micropore drilled in 200 nm thick $Si0_2$ membrane using FIB. (a) The micropore just after drilling. The red circle shows the rough structure inside and on the edges of the pore walls. (b) The sample heated at 1050 ^{o}C for 5 minutes in furnace having nitrogen flow of 10 sccm. It clearly shows that the micropore edges and inner wall surface became smooth which helped in cell translocation and reduced probability of the breaking of the cell outer membrane. The pore became more circular after heat treatment. (Scale bar = 10 µm). Reprinted by permission of The Royal Society of Chemistry [179] 94

4.3 Shows the micropore device measurement setup. (a) Syringe pump connected to one of the reservoirs made with teflon blocks. The chip with single micropore is sandwiched between two teflon blocks using PDMS gaskets to avoid any leakage. One Ag/AgCl electrode is inserted in tubing at inlet and another at the outlet. The biasing and data collection is done with LabView software routines using data acquisition cards. (b) The top view of the teflon blocks, showing the PDMS gaskets used for sealing the micropore device. Reprinted by permission of The Royal Society of Chemistry [179].....95

4.4 Shows the optical micrographs of the cell suspensions on glass slide. (a) Whole blood diluted with PBS. (b) Renal cancers cells suspended in PBS. (c) Renal cancer cells mixed with whole blood and suspended in PBS solution. All the images were taken with same lens and

magnification. The scale bar is 50 µm. Reprinted by permission of The Royal Society of Chemistry [179].....96

4.5 Shows concentration comparison between micropore device and hemocytometer cell counter device for 5 different concentrations of renal cancer cells (5 to 500 cells/50 µL). The plot is for 12 µm pore at flow rate of 10 µL per min. The dot line (purple) is a linear regression of 5 samples (R^2= 0.9999) and indicates good correlation between the two methods. Reprinted by permission of The Royal Society of Chemistry [179].....97

4.6 Shows the translocation pulses for all cell types (Cancer Cell, WBCs, RBCs) at different time points (1, 10 and 25 mins). The device shows the stable behavior. Reprinted by permission of The Royal Society of Chemistry [179].....98

4.7 Shows the distribution of the cell data according to their size while translocating through 12 µm pore. (a) This plot points out the distribution of cancer cells from the other cell types. (b), (c) and (d) show pulses for Cancer cells, WBCs and RBCs, respectively. It depicts that the pulses for cancer cells showed more current blockage and more translocation time when compared with other cell suspensions. (e-g) Show the close-up of the RBCs pulses. Almost all of the pulses were double spiked or irregular shaped in contrast to the pulses from cancer cells which were smooth and bell shaped. It suggested that the device only showed signals for RBCs when they were clumped together. Reprinted by permission of The Royal Society of Chemistry [179].....100

4.8 Shows the distribution of the cells according to their size while translocating through 20 µm pore. (a) Plot shows reduction in pulse magnitudes in comparison to those for the 12 µm pore. The plot shows distinct behavior for cancer cells in contrast to other cell types. (b-d) Shows the pulse data from pClamp software. (b), (c) and (d) show example pulses for cancer cells, peripheral mononuclear cells and RBCs, respectively. Reprinted by permission of The Royal Society of Chemistry [179].....102

4.9 Shows the distribution of the cells data according to their size while translocating through 20 µm pore at flow rate of 25 µL per min. This data points out the distinct distribution of cancer cells from the other cell types. The average translocation times and current blockade amplitudes for renal cancer cells were significantly higher than other cells types. Only few WBCs and RBCs were detected at higher flow rate of 25 µL per min. Reprinted by permission of The Royal Society of Chemistry [179].....103

4.10 Shows the density plots for mixed cell suspensions. (a) Shows the density plot of the whole blood diluted with PBS at a ratio of 1:10 for 12 µm pore. The colormap at right of each plot shows the density distribution of cells according to their translocation time and pulse amplitude. (b) Shows the density plot when mixture of whole blood with

renal cancer cells was processed using the pore chip. Because of size difference the cancer cells showed distinctive current pulses as highlighted by dashed oval. Analysis of the pulse shapes further reduced the background noise. The cancer cells gave smooth bell shaped pulses, while the other cells and clumps gave spiked pulses because of their irregular orientation. (c) Shows the density plot of diluted whole blood with PBS buffer for 20 µm pore. All the other parameters were same as for 12 µm pore. (d) Shows the density plot, when renal cancer cells were mixed with the solution of whole blood with PBS and whole mixture was process with 20 µm pore. The cancer cells can be differentiated easily form other cells based on their current pulse characteristics. Characteristic pulses were detected form the data and are shown for different data distributions. Reprinted by permission of The Royal Society of Chemistry [179] 105

4.11 Shows the density plots for mixed cell suspension. (a) Shows the density plot of the whole blood diluted with PBS at a ratio of 1:10 for 20 µm pore. The flow rate was 25 µL per min. (b) Shows the density plot when mixture of whole blood with renal cancer cells was processed using the micropore chip of 20 µm diameter. Because of size difference the cancer cells showed distinctive current pulses as highlighted by dashed oval. At flow rate of 25 µL per min, detection efficiency was reduced to 40%, and pulse characterizing based on pulse shape became more challenging. Reprinted by permission of The Royal Society of Chemistry [179] 106

5.1 Shows the SEM micrographs for original and chemically treated eggshell surfaces. (a) Original eggshell surface. (b) Eggshell treated with 25% H_2SO_4 solution for 30 minutes. (c) Eggshell treated with 15% HCl solution for 5 minutes 114

5.2 Shows the SEM micrographs of micro-needles synthesized by the chemical reaction of eggshell with sulfuric acid. (a) Shows single micro-needle with width of ~800 nm. (b) The lengths of micro-needles ranged between 25–60 µm 114

5.3 Shows SEM micrograph of the eggshell treated with HCl. The diameter of most of the nanopores is less than ~100 nm 115

5.4 EDS elemental analysis of original and chemically treated eggshell samples. (a) EDS spectrum of original eggshell. (b) EDS spectrum of eggshell sample treated with diluted H_2SO_4. (c) EDS spectrum of eggshell sample treated with diluted HCl 116

5.5 Elemental mapping of sulfuric acid treated eggshell samples. (a) SEM micrographs of the sample area used for mapping. Mapping micrographs show: (b) Mapping of calcium; (c) Mapping of carbon; (d) Mapping of oxygen; (e) Mapping of sulfur 117

5.6 X-ray diffraction spectra for original and chemically treated eggshell samples. (a) Comparison between XRD spectra of original eggshell and H_2SO_4 treated eggshell. The peaks represented by arrows show

the characteristics of crystalline calcite phase having *hkl* (104), (113), (202), (018) and (116). Stars represent the peaks not associated with calcites. (b) Comparison between XRD spectra of original eggshell and HCl treated eggshell 119

5.7 Shows AFM micrographs of PDMS samples casted form native and processed eggshells. (a) Sample-1, PDMS casted on plain glass surface. (b) Sample-2, PDMS casted on eggshell with micro-needles. (c) Sample-3, PDMS casted from eggshell with nano-texture....120

5.8 Shows SEM micrographs of PDMS samples. (a) Sample-2 with nano to micron range features. (b) Sample-3 with nano-texture 121

5.9 Shows fluorescent intensity (a.u.) after laminin coating of PDMS samples. There were significant statistical differences between flat and textured PDMS samples (**p* <0.0001, n=4). Nano-textured PDMS samples were also statistically different from micro-structured PDMS samples (#*p* <0.0001, n=4)....122

5.10 hows fluorescently labeled human fibroblasts on different PDMS surface types. (a) Fibroblast growth on cell culture. (b) Fibroblast growth on flat PDMS, Sample-1. (c) Fibroblast growth on Sample-2. (d) Fibroblast growth on Sample-3. Human fibroblast cells were cultured for 3 days before fluorescent imaging 123

5.11 Shows human fibroblast growth density on all three types of PDMS samples. The cells were imaged and counted after 3 days of cell growth. There was significant statistical differences between Sample-1 and other samples (**p* <0.01, n=4), while Sample-2 and Sample-3 were not statistically significant different (#*p* = 0.12, n=4)....124

5.12 Shows SEM micrographs showing human fibroblast morphology on all types of PDMS surfaces. (a) Fibroblast morphology on flat PDMS sample (spherical). (b) Fibroblast morphology on PDMS Sample-2 (elongated). (c) Fibroblast morphology on PDMS Sample-3 (elongated and spread out)....125

6.1 Shows the SEM micrograph of the gold lines as patterned with optical photolithography. Reprinted with permission [209]....128

6.2 Shows the SEM micrographs for FIB scratches at different accelerating voltages, milling currents and time of scracthing exposure; (a) 30 kV, 100 pA, 120 sec (b) 30 kV, 20 pA, 120 sec, and (c) 30 kV, 1 pA, 60 sec. Magnified view of scratch is shown in inset of (c). Reprinted with permission [209]....129

6.3 Shows the *I-V* data of metal lines after the FIB scratch. Inset shows the sudden drop in current through metal line describing the complete break of the metal. Reprinted with permission [209] 130

6.4 Shows the SEM micrograph with the nano-gap between metallic line. Reprinted with permission [209] 130

6.5 Shows the *I-V* plot before and after break in metallic lines due to electromigration. Reprinted with permission [209] 131

6.6 Shows the distribution of the devices according to conductance and nano-gap distance. The most of the gaps were in the range of 100 to ~300 nm. Reprinted with permission [209] 132

7.1 Shows the nanopore structure after PPPF deposition and anti-EGFR functionalization 136

7.2 Shows the expected current translocations pulses from EGFR and BSA proteins through aptamer functionalized solid-state nanopore 137

7.3 Shows the schematic for experimental setup that can be used for selective enumeration of CD4+ lymphocytes. The inset shows the translocation of a cell (red) through the micropore functionalized with CD4+ antibody 138

7.4 Shows the schematic for PDMS device having nano-textured bottom. The hGBM cells can be captured efficiently with aptamer functionalized, nano-textured surfaces 139

LIST OF TABLES

Table Page

3.1 EDS Analysis of the Nanopore after Different Processing Steps. Reprinted with permission [48] 42

3.2 Time taken by GPU kernel: GPU kernel with data transfers and corresponding CPU code using Static threshold Technique. Reprinted by permission from Elsevier [168]....87

3.3 Time taken by GPU kernel: GPU kernel with data transfers and corresponding CPU code using Baseline-tracker threshold technique. Reprinted by permission from Elsevier [168]....88

3.4 Time taken by GPU kernel: GPU kernel with data transfers and corresponding CPU code using moving average technique. Reprinted by permission from Elsevier [168]....88

3.5 Time taken by GPU for different input sizes using the moving average algorithm, and overall system time. Reprinted by permission from Elsevier [168] 88

4.1 Translocation time and amplitude for different cell types for 12 µm pore. Where *P<0.01 between CTCs and others; #P<0.01 between WBCs and RBCs. Reprinted by permission of The Royal Society of Chemistry [179] 101

4.2 Translocation time and amplitude for different cell types for 2o µm pore. Where *P<0.01 between CTCs and others; #P<0.01 between WBCs and RBCs. Reprinted by permission of The Royal Society of Chemistry [179] 103

CHAPTER 1

INTRODUCTION

The field of nanotechnology has seen unprecedented growth and development in last few years. It has been even termed as a “disruptive technology”, a technology that can sustainably overturn the existing dominant technological paradigms in the act of its evolution. These areas hold some of the greatest promises, drawing up contributions from chemistry, physics, biology, materials science, medicine and engineering. Integration of biology and silicon at the micro and nano scale offers tremendous opportunities for solving important problems in biology and medicine and enables a wide range of applications in diagnostics, sensing, therapeutics, and tissue engineering. Much of current research focuses on the integration of biomedical engineering, nanoscience and nanotechnology, with particular focus towards their application in diverse areas like bio-sensors, proteomics and detection of CTCs. The sensing and characterization of biological entities, processes and interactions, by electrical means and novel nanoscale devices will have an immediate and far reaching impact in life sciences.

1.1 Structure of Dissertation

The overall goal of this work is to design highly sensitive solid-state devices for analyzing the DNA, detection of circulating tumor cells (CTCs), rapid fabrication of break-junctions and synthesis of nano-textured surfaces from chicken eggshell. This dissertation is divided into 7 chapters. The breakdown of chapters is given below:

1.1.1 Introduction (Chapter 1)

This chapter is meant to introduce the reader to the drive and objective behind the entire research work. It also explains the advantages of using nanotechnology in medicine.

1.1.2 Background and Literature Review (Chapter 2)

Chapter 2 reviews the literature about the state of art in nanopore fabrication methods, etching process, DNA analysis, pulsed plasma polymer deposition, CTCs properties, cancer detection and isolation significance, current biosensors and their limitations, recent developments in nano-textured surfaces and methods to fabricate break-junctions.

1.1.3 Nanopore Based Solid-State Sensors for DNA Analysis (Chapter 3)

Solid-state nanopores are important candidates to be used as biosensor platforms. The nanopore shrinking is done using electron or ion beam sculpting. Both of these processes are time consuming and require expensive equipment. We developed a nanopore shrinking method using direct thermal heating. We have successfully reduced the nanopore diameter to sub-ten nanometers using direct heating. Our fabrication method can be used to batch fabricate an array of nanopores.

Pulsed plasma polymer deposition is used to control the surface charges and composition of polymer films. We have developed a process to reduce nanopore diameter using pulsed plasma assisted deposition of methacrylic acid films. The surface charges on the nanopore walls have been controlled by this process. The nanopore surface charges plays very important role in controlling the DNA translocation through the nanopore. The translocation velocity of DNA can be controlled by nanopore wall charges. We have also showed the DNA translocation through these nanopores.

Passing DNA through the solid-state nanopore generates millions of recorded data points. Processing of such a huge amount of data is beyond the capabilities of an individual computer machine, especially for real-time processing. Furthermore, the process of finding pulses in the data is currently performed offline using manual analysis, which is subjective, tedious, time-consuming, and error prone. In order to address these issues, we have developed a solution by coupling advanced input/output (I/O) techniques of computer architecture with graphical processing unit (GPU) based algorithms. Our approach has shown significant

improvements in real-time pulse detection and can be used as an integral part of the next-generation production systems.

1.1.4 Solid-state Micropore Sensors for Detection of Cancer Cells (Chapter 4)

The circulating tumor cells (CTCs) are believed to detach from the solid tumor and spread through blood to secondary tissues. Precise quantification of CTCs in the peripheral blood can be used for early-diagnosis and to help against metastasis of disease. Current CTC detection and quantification approaches either give lower than desired yield or involve fluorescent tags for counting. Some of the processes are laboratory dependant and very expensive requiring equipment like optical flow cytometry. We developed solid-state micropore based detection systems for precise quantification of CTCs from whole blood. Our method does not require fluorescent tags and give higher detection efficiency. Chapter 4 covers the micropore fabrication process, platform development, CTCs quantification and detection experiments.

1.1.5 Nanotextured Scaffold from Chicken Eggshells (Chapter 5)

The surfaces with nano-structures, dense nanopores and high surface area are considered ideal in many detection and tissue engineering applications because of the topographical resemblance with extracellular matrix (ECM). Therefore processes to make surfaces with nano-texture are highly desirable. Secondly, the textured surfaces have found a lot of application in biosensors, proteomics and light emitting diodes. We have developed a simple and inexpensive process to make nano- and micro-textured substrates using chicken eggshell. Chapter 5 describes the synthesis of micro and nano-textured surfaces from chicken eggshell using wet chemical etching. Standard material characterization techniques were used to perform pre- and post- composition analysis of eggshell scaffolds. Chapter 5 also covers the laminin protein attachment and fibroblast cell proliferation studies on micro and nano-textured surfaces.

1.1.6 Rapid Nano-manufacturing of Break-Junctions using Focused Ion Beam (FIB) and Electromigration (Chapter 6)

Nano break-junctions are composed of two metal wires with nanogap between them. They have been used to study the electrical transport properties of the molecules. These are typically fabricated using e-beam lithography or electromigration. Both of these processes are either limited by long processing times or give less that desired yield. We have developed a break-junction fabrication process using FIB scratching followed by electromigration. The fabrication method is rapid and gives higher yield. We can control the location of the FIB scratch and hence the final nanogap. Chapter 6 covers the fabrication process of gold break-junctions in details.

1.1.7 Future Research Directions (Chapter 7)

Chapter 7 covers the future directions and potential use of developed biosensing platforms. It includes the scope of more work that could supplement/complement current work.

CHAPTER 2

BACKGROUND AND LITERATURE REVIEW

2.1 DNA Sequencing and Analysis

2.1.1 Structure of DNA

Deoxyribonucleic acid (DNA) is the genetic material found in all living organisms [1-3]. It is present inside the nucleus of the cell. It encodes the architecture and functions of cells [4, 5]. The DNA is composed of two polynucleotide strands wrapped together to form a helical structure, called the DNA double helix [6-8]. It consists of four building blocks also called bases naming Adenine (A), Thymine (T), Guanine (G) and Cytocine [6]. The two DNA strands are held together by hydrogen bonds between two pairs of bases, A and T (2 hydrogen bonds), and G and C (3 hydrogen bonds). For instance, if the sequence of one strand is 5'-ATGCAAGG-3', the sequence of other strand will be 3'-TACGTTCC-5'. The two nucleotide strands run antiparallel to each other and form DNA helix structure. Each nucleotide consists of phosphate group, 5-carbon sugar and nitrogenous base.

2.1.2 DNA Sequencing and Analysis

As many diseases and phenotypic characteristics are first expressed at DNA level, it is highly desirable to sequence the DNA base by base. Since 1990s, DNA sequencing has been carried out with capillary based Sanger biochemistry [9-11]. DNA to be sequenced is prepared by polymerase chain reaction (PCR) amplification with primers that flank the target. The output of the PCR reaction is many PCR amplicons present within same reaction volume. The primer is complementary to the known sequence immediately flanking the region of interest. Each round of primer extension is terminated by the attachment of fluorescently labeled dideoxynucleotides (ddNTPs). In the resulting mixture, the label on the ddNTPs of any given

fragment corresponds to nucleotide identity. Capillary based polymer gel electrophoresis is used to separate single-stranded, end labeled extensions. As fragments of discrete lengths exit the capillary, laser excitation is used to detect the fluorescent labels. The recorded data is further analyzed by computer software to build the DNA sequence. The whole process is described briefly in Figure 2.1. In DNA microarray sequencing, oligonucleotide probes are tethered to the chip with many possible combinations. Labeled target nucleic acid fragments are hybridized to the array of tethered oligonucleotides. Image scanning and post data analysis techniques are used to sequence the target fragments.

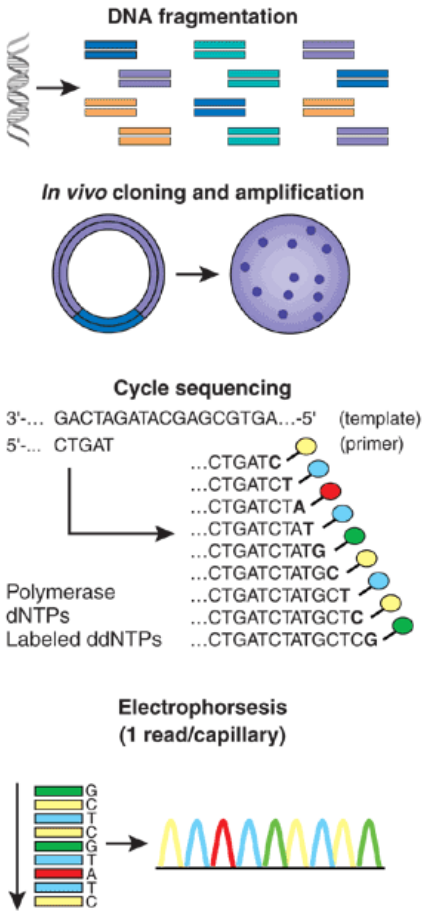

Figure 2.1 Workflow of conventional Sanger DNA sequencing. Reprinted by the permission from Nature Publishing Group Ltd: Nature Biotechnology [12], copyright (2008)

2.2 Nanopore Biosensors for DNA and Protein Analysis

2.2.1 Nanopore Biosensors

Despite major advancements in the field of DNA sequencing, there is still a lot of room to develop an inexpensive and efficient platform. One of the most compelling advantages of possible nanopore sequencing and analysis is the prospect of inexpensive sample preparation requiring minimal chemistries or enzyme-dependent amplification. Nanopore based biosensor can eliminate the need for nucleotides and polymerases or ligases during readout. Thus, the costs of nanopore sequencing are projected to be far lower than ensemble sequencing by the Sanger method, or any of the recently commercialized massively parallel approaches. Nanopores have emerged as novel platforms for DNA and protein analysis [13-20]. In these studies, translocations of biological molecules are monitored using a dual compartment setup, with the compartments separated by a membrane having a single nanopore [21-31]. An applied potential produces a steady-state ionic current flow from one compartment to the other. For example, passage of negatively charged DNA molecules through the nanopore provides characteristic current blockade pulses for each particular analyte. Nanopore biosensors have been used to study various biophysical properties including sequence based DNA detection and stretching [32-34]. Such a label free electrical detection platform is adapted for protein biomarkers and other larger macromolecules.

2.2.2 Protein Nanopores

The biological nanopores, also called ion-channels, are important parts of living organisms; providing paths for specific transport of ions or macromolecules in cells and organelles. The functionalization of synthetic nanopore channels can also be used to explore the nature of cationic selectivity in the regulation of cellular processes [35-42]. The graphic for α-Hemolysin (α-HL) protein is shown in Figure 2.2. α-HL is a protein toxin from bacteria Staphylococcus Aureus, with diameter of 2.6 nm [43]. An artificial lipid bilayer of diphytanoyl phosphatidylcholine was formed across an orifice of 0.1 mm. The orifice was separating two

buffer filled compartments. Once α-HL was added to one of the compartments, it reconstructed into an ion-channel. When DNA was added to *cis* side of the protein channel, it translocated towards the positive electrode under applied potential. DNA moved towards the positive side as it has net negative charge. When DNA passed through the protein nanopore, it gave distinctive current blockage pulses. The length of the DNA was correlated to the pulse width and pore blockage was correlated to pulse height or magnitude [43].

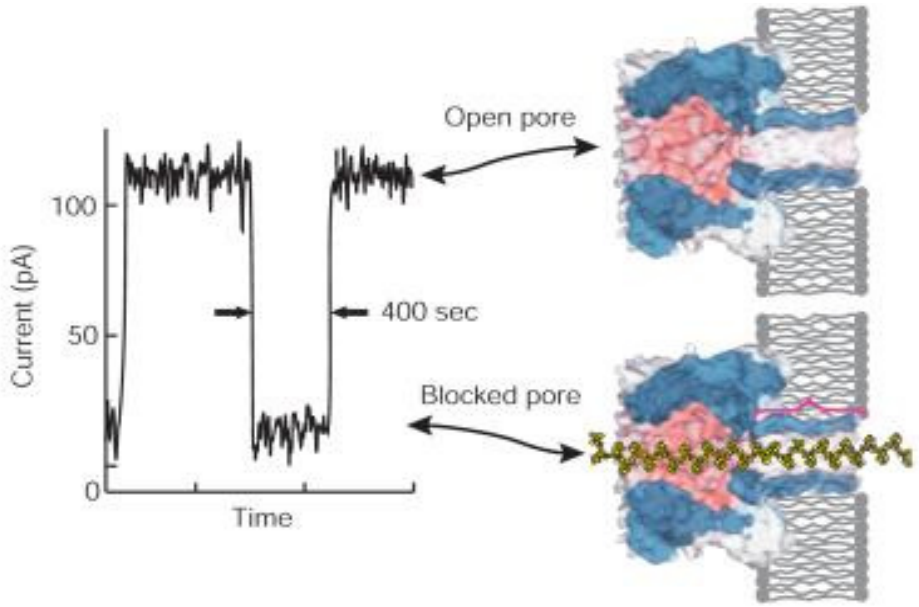

Figure 2.2 Shows a typical α-HL protein nanopore is shown (right). And characteristic current pulses are shown at left. When target molecule passes through the nanopore, it give distinctive current blockage pulses. Reprinted by the permission from Nature Publishing Group Ltd: Nature Biotechnology [44], copyright (2008)

Meller et al. showed that nucleotide of different sequences could be differentiated from each other based on their current blockage pulse shape [45]. Polymers with the same length but different sequences were analyzed. The translocation events were characterized by their pulse shape. The pulse width of poly$(dA)_{100}$ and poly$(dC)_{100}$ were analyzed to be different although these had same length as shown in Figure 2.3. The different polymers could be discriminated in a mixture.

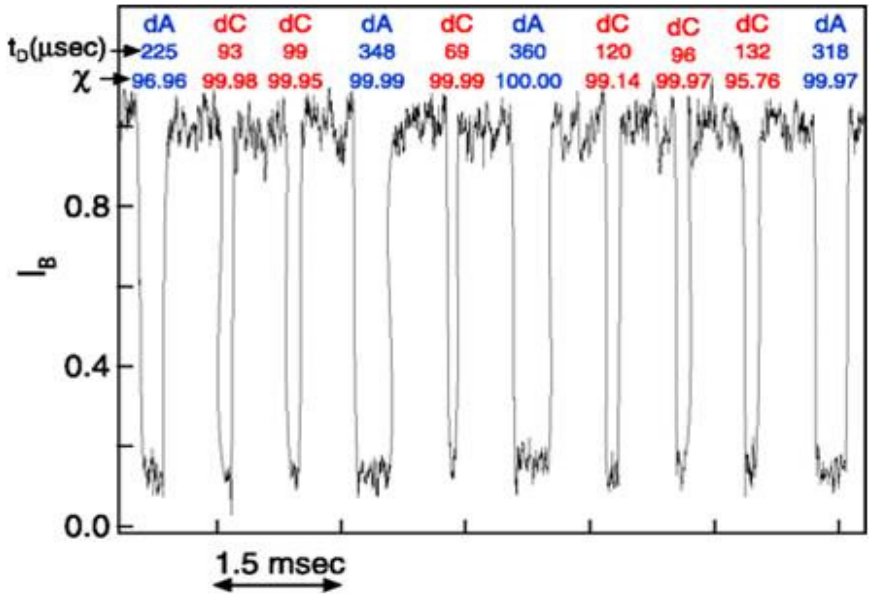

Figure 2.3 Shows current pulses of 10 events recorded from a mixture of equal molar concentrations of poly(dA)$_{100}$ and poly(dC)$_{100}$. The individual events are identified, on the basis of t_D (translocation time/pulse width). $\varkappa$ represents the confidence in the molecule identification, Reprinted by permission from PNAS [45], copyright (2000)

In another report, Bayley et al. demonstrated the attachment of single strand DNA (ssDNA) inside protein nanopore [34]. Two ssDNA targets, one complementary to the tethered DNA and other with just a single base mismatch, were used for translocation study. The binding of the target ssDNA with tethered ssDNA affected the shape of current blockade pulses. Two targets could easily be discriminated based on their pulse width and pulse magnitude as shown in Figure 2.4 [34]. Using an array of protein nanopores with tethered DNA, complete codon in an individual DNA strand was sequenced. They did not look into the differences in translocation events for a target DNA through a nanopore without the tethered DNA. Some other research groups have analyzed the effects of applied voltage, temperature and salinity of buffer solution on translocation characteristics of DNA [46, 47].

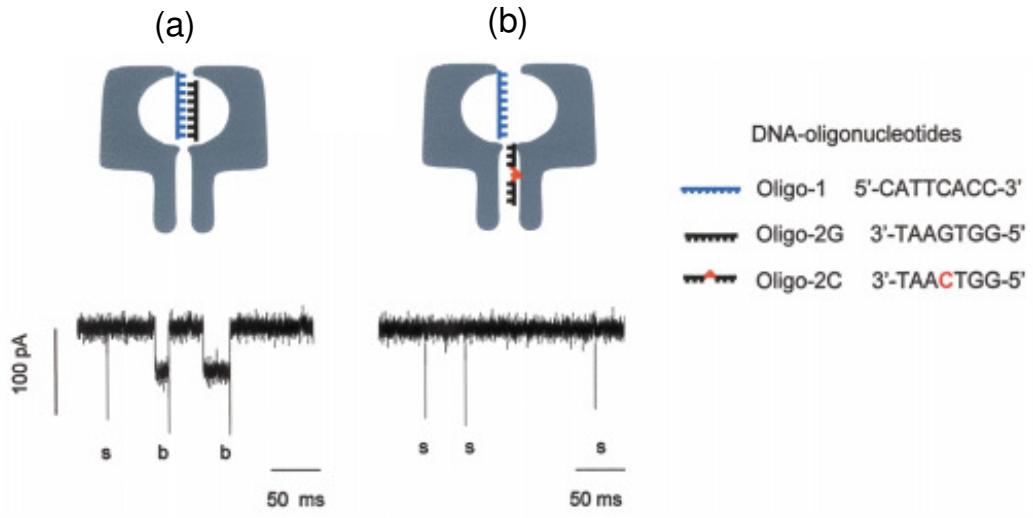

Figure 2.4 when perfect complementary target DNA translocates through the nanopore. (b) Translocation pulses when single base mismatch target DNA translocates through the pore. Reprinted by permission from Nature Publishing Group: Nature Biotechnology [34], copyright (2001)

2.2.3 Solid-State Nanopores (SSNs)

Protein nanopores have inspired the fabrication of solid-state nanopores [13, 21, 23, 24, 44, 48-58]. Solid-state nanopores have advantages over protein nanopores as these can be fabricated easily on large scale. Solid-state nanopores can withstand varying experimental conditions including higher temperature, higher salinity and solution with higher pH values [58]. We have more control on nanopore diameter, channel length and material selection. These also have power to detect specific genes, thus ability to forewarn susceptibility to different diseases. Methods to fabricate and functionalize solid-state nanopores are already well developed. The functionalization of solid-state nanopores provides the ability to discriminate single base mismatch in any single strand of DNA [55].

2.2.4 Fabrication of Solid-State Nanopores

Researchers have developed many fabrication methods for efficient synthesis of SSNs [18, 24-26, 28-31, 48, 59, 60]. Researcher at Harvard University pioneered the drilling of nanopores in silicon nitride thin films using argon ion beam [61, 62]. They found that ion

interactions with thin films involved surface erosion and surface diffusion. Surface erosion resulted in opening of a pore while surface diffusion involved matter transport resulting in closing or shrinking of a pore. Since then a lot of different processes are developed such as feedback controlled chemical etching, ion sculpting, electron beam sculpting, and laser heating [52, 63-65]. The typical nanopore fabrication process involves standard silicon fabrication methods such as oxidation, photolithography, dry and wet chemical etching, ion/electron beam drilling and scanning electron microscope (SEM) analysis. Most of the processes involve the fabrication of thin membranes as the first step. The process flow to fabricate thin oxide membrane is shown in Figure 2.5.

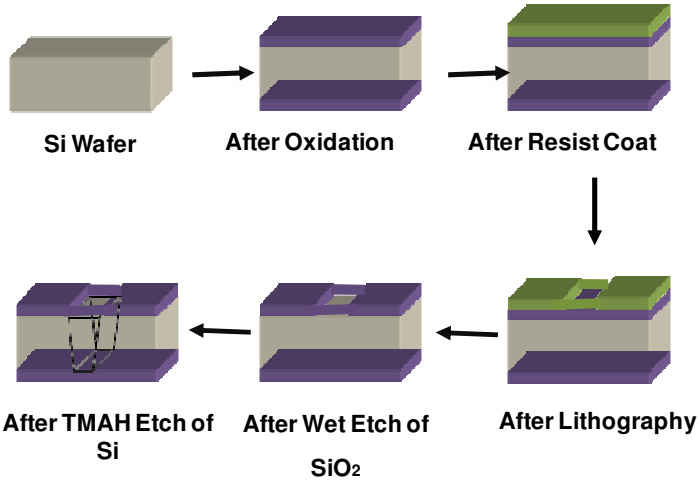

Figure 2.5 Process flow of fabricating oxide membrane, used for ion/electron drilling. The process starts with a bare silicon wafer which is oxidized at a temperature > 900 ^{o}C. Resist is then applied to one side of the wafer. Photolithography, buffered hydrofluoric acid etching, acetone wash, and tetramethylammonium hydroxide (TMAH) etching completes the process flow [66]. Reprinted by permission from Springer, coypright (2011)

2.2.4.1 Anisotropic Wet Chemical Etching

One of the fundamental processes in the fabrication of SSNs is the fabrication of thin membrane. The free standing membranes can be fabricated by anisotropic wet chemical etching using tetra-methyl-ammonium-hydroxide (TMAH) [67-69]. A variety of microelectromechanical devices, diaphragms, structures and cantilevers are fabricated by an

anisotropic etching of (100) silicon wafers. Other chemicals such as potassium hydroxide (KOH), ethylenediamine-pyrocatechol-water (EDP), and hydrazine-water solutions are also used for directional etching of Si [70]. Some of the etchants are not CMOS compatible, for example, the presence of potassium ions during KOH etching can destroy the device because potassium ions are fast diffuser in Si. Therefore, a lot of research groups have been working with TMAH. The addition of TMAH into etching solution produces excess of OH^- ions which are necessary for the formation of water soluble silicate complex. The whole chemical reaction is shown by Equations 2.1-2.5.

$$(CH_3)_4 NOH \rightarrow (CH_3)_4 N^+ + OH^- \quad (2.1)$$

The etching of Si occurs in series of chemical reactions which involves first the oxidation of Si surface and then chelation process that forms water soluble product [71]. The oxidation process is expressed as

$$Si + 2OH^- \rightarrow Si(OH)_2^{++} + 4e^- \quad (2.2)$$

$$Si(OH)_2^{++} + 4OH^- \rightarrow SiO_2(OH)_2^{--} + 2H_2O \quad (2.3)$$

And the chelation process is expressed as

$$4H_2O + 4e^- \rightarrow 4OH^- + 2H_2 \quad (2.4)$$

The overall process is expressed as

$$Si + 2OH^- + 2H_2O \rightarrow SiO_2(OH)_2^{--} + 2H_2 \quad (2.5)$$

The Si etch rate increases as the concentration of TMAH increases from 2% to 4% and decreases with further increase in TMAH concentration. The etch rate of p-type Si is slightly lower that n-type Si [72]. The etch rate is affected by TMAH concentration and solution temperature, as shown in Figure 2.6.

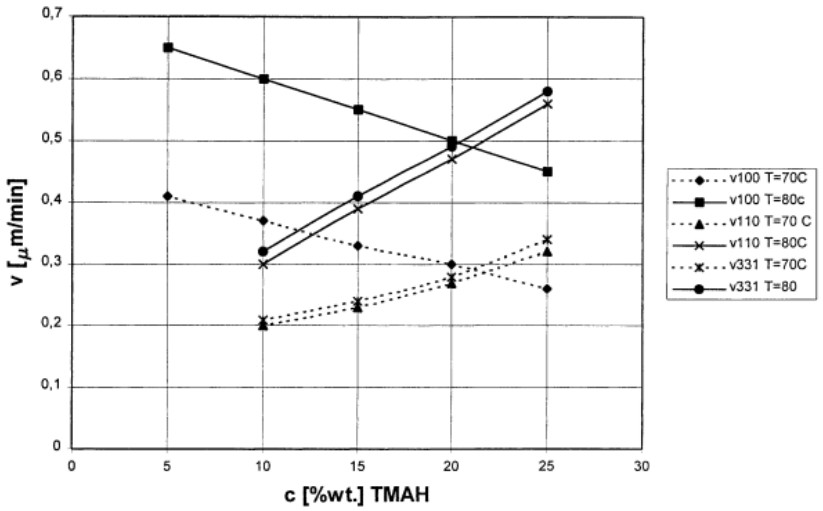

Figure 2.6 Etching rates of Si (h k l) planes in TMAH solution vs. TMAH concentration, T = 80 ^{o}C: Solid lines, T = 70 ^{o}C: Dotted lines. Reprinted by permission from Elsevier: Sensors and Actuators A: Physical [69], copyright (2001)

Isopropyl alcohol (IPA) is found to be very affective additive to increase the smoothness of Si etched in TMAH solution. It is also known that IPA decreases the etch rate of Si wafer as shown in Figure 2.7. It is suggested that reduced etch rate by IPA addition is due to the physical adsorption of IPA ions onto Si surface which blocks the contact of hydroxyl ions to react. This results in reduced chemical activity and hence reduces the overall etch rate [69]. The resulted smooth Si surface is believed to be due to less aggressive Si etching after IPA addition [69]. Addition of IPA in KOH solution has also been found to reduce the Si surface roughness.

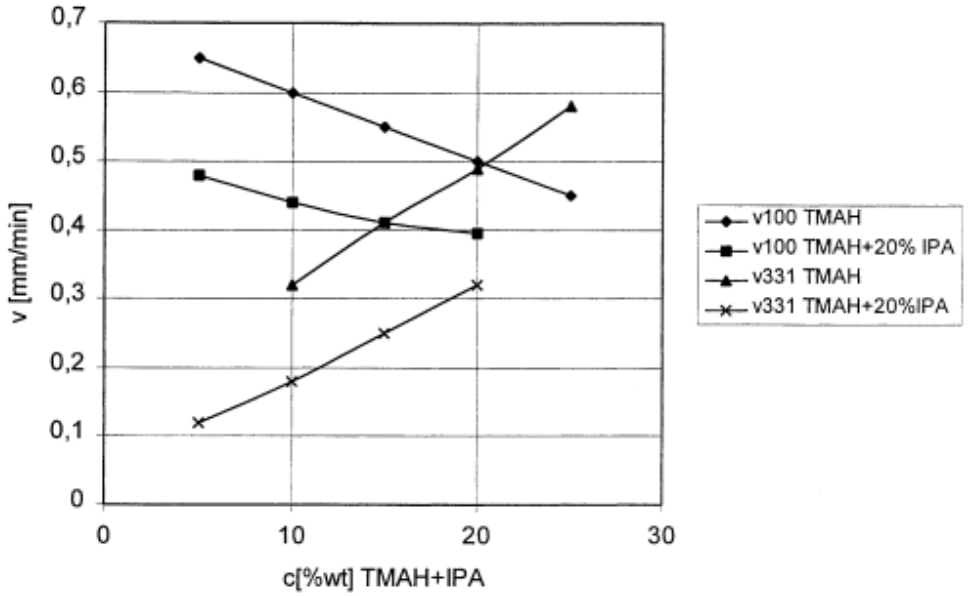

Figure 2.7 Etching rate of Si (h k l) planes in TMAH vs. TMAH+IPA concentration at 80 ^{o}C [69]. The plots shows that etch rate is reduced by addition of IPA into TMAH solution. Reprinted by permission from Elsevier: Sensors and Actuators A: Physical [69], copyright (2001)

2.2.4.2 Ion and Electron Beam Sculpting processes

Once the free standing membrane is fabricated, nanopore needs to be drilled. Electron and ion beam sculpting processes are used to drill nanopores [62, 73]. During the sculpting process, the ion or electron beam is focused on small area of thin membrane; it melts the surface locally and drills a nanopore inside a membrane. The beam intensity and shape play very important role in determining the initial pore diameter. Li et al. had used feedback controlled ion beam sculpting process to make a nanopore in silicon nitride (SiN) membrane [62]. The ion beam sculpting system is shown in Figure 2.8. They made a bowl shaped cavity at one side of the membrane and then used ion beam to sputter SiN layer by layer until a 60 nm pore was opened. They found that continuous ion beam exposure had started shrinking the pore. Two processes of ion beam erosion and atomic flow of matter were putatively occurring at the same time.

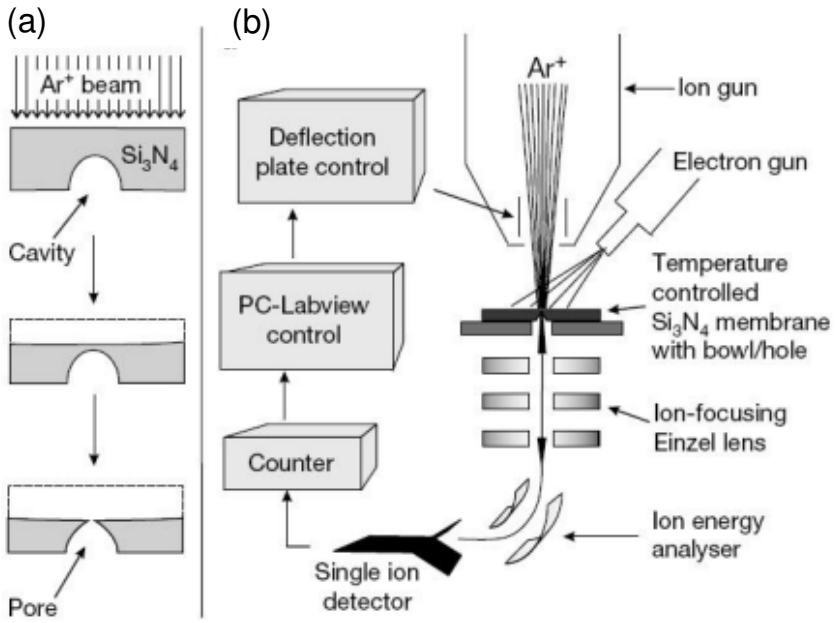

Figure 2.8 Ion beam sculpting process. (a) Schematic showing the thin nitride membrane fabrication and 60 nm pore drilled using ion beam. (b) The feedback controlled ion beam milling setup. Reprinted by permission from Nature Publishing Group: Nature [62], copyright (2001)

Dekker and coworkers at Delft University used electron beam sculpting to first drill a nanopore and then to reduce its diameter as shown in Figure 2.9 [64]. Their process allowed *in situ* imaging of the nanopore during drilling. The electron beam softened the material around the nanopore which flowed to shrink the pore. They found that nanopore shrinking was possible if $r < h/2$, where "*r*" was the radius of the nanopore and "*h*" was the channel length or thickness of the membrane. The soft material flowed in a direction to achieve morphology of minimum surface free energy. Chang et al. also showed similar results with field emission scanning electron microscope (FESEM) [52]. They used silicon on insulator (SOI) wafer to make thin membrane. They reported shrinking of 50 nm pores to 10 nm. They proposed "radiolysis" as the mechanism for nanopore shrinking under FESEM. They proposed that previous assumption of pore shrinking due to electron beam irradiation was not applicable to porous and polycrystalline Si.

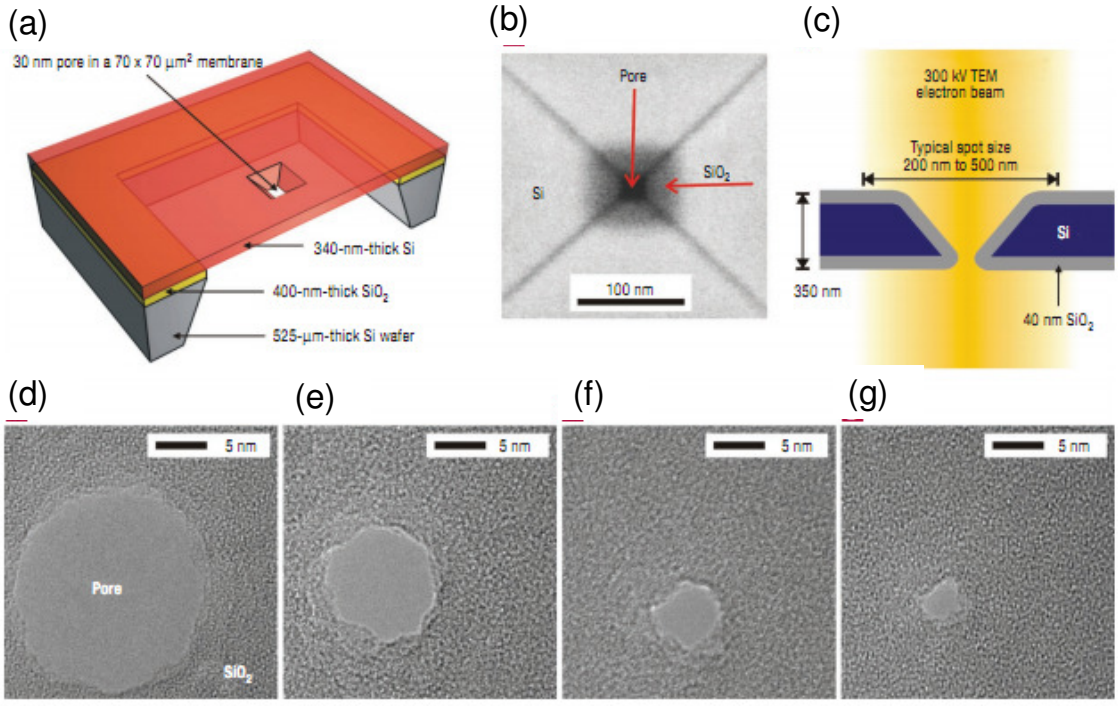

Figure 2.9 (a) cross-sectional view of the nanopore and the membrane. (b) Scanning electron microscope image for the fabricated nanopore after oxidation. (c) Cross-sectional view of the nanopore under electron beam irradiation. (d-g) Sequence of micrographs show the electron beam induced shrinking process. The final nanopore diameter is 3 nm. Reprinted by permission from Nature Publishing Group: Nature Materials [64], copyright (2003)

2.2.4.3 Nanopore Shrinking with Material Deposition

Besides electron and ion beam shrinking processes, diameter of SSNs can also be reduced using thin layer of deposited material. In one report, nanopore diameter was reduced to sub ten nm by selective electron-beam-assisted deposition of silicon dioxide [24]. Tetraethyl orthosilicate was decomposed by electron beam and deposited inside the nanopore to reduce the pore diameter. The reservoir for gas precursor was maintained at constant temperature to have stable gas pressure. Ion beam can also be used to deposit silicon dioxide inside the nanopore [74]. Chen et al. used atomic layer deposition to fine tune the nanopore surface

composition and reduced SSN diameter [54]. Alumina was deposited layer by layer to control the shrinking process. Alumina coating on nanopores reduced the defects made by FIB and eliminated the surface charges.

2.2.4.4 Functionalization of Solid-State Nanopores

Solid-state nanopores are functionalized for selective sensing of DNA and other biomarkers. Attachment of selective probes and surface charges on nanopore walls plays very critical rule in selective bio-sensing. Siwy et al. proposed the idea of protein biosensors. They attached biotin at the entrance of gold nanotubes for selective sensing of biomarkers. When target molecule tried to translocate through the nanopore, it got attached with the molecular recognition agent that resulted in complete blockage of ionic current [75-77]. They also attached thiol modified DNA probes inside the gold nanotube [20]. Nilsson et al. functionalized the SSN with acrylamide-terminated ssDNA probes. The attachment of ssDNA probes inside the SSN reduced the pore diameter which was confirmed with *IV* measurements [78]. Iqbal et al. used 3-aminopropyltrimethoxysilane, forming a silane layer, and the nanopore channel was further functionalized with a homo-bifunctional agent [55]. SSN was functionalized with an amine-modified ssDNA probe. In order to make a hair-pin loop out of the probe DNA, the probe was engineered to have complementary sequences at both ends of the molecule as shown in Figure 2.10. The hair-pin loop orientation was used to further analyze single-mismatch base pairs of DNA during translocation. They successfully discriminated perfect complementary DNA from single-base mismatched DNA.

The sequence of a DNA segment can't be determined at high translocation velocity. At higher translocation velocity, it's almost impossible to get useful information about a single base pair of DNA due to the limitations of the electronic detection systems. The typical translocation velocity through 10 nm nanopore is about 27-30 nucleotides/μs [21]. DNA translocation velocity

can be controlled by varying the electrolyte temperature, applied potential, and electrolyte viscosity, but these variations also reduce signal-to-noise ratio due to reduced ion mobility [29, 45, 79]. Kim et al. proposed the idea of reducing the translocation velocity by functionalizing the nanopore surface with positive charges [80]. They used atomic layer deposition of alumina for shrinking the SSN diameter to 30 nm. The alumina deposition provided the conformal coating on all sides of the nanopore walls. After piranha cleaning, the chip was left for one hour in ethanolic solution containing 1% (v/v) aminopropyltriethoxysilane (APTES). The APTES functionalization produced positive charges on the nanopore walls. When negatively charged DNA translocated through positively charged nanopore, its velocity was reduced due to opposite charge interactions [80, 81]. Umehara et al. suggested the idea of ion current rectification with a quartz nanopipette coated with positively charged poly-L-lysine (PLL). Stable ayer was achieved by adsorption of PLL molecules on the negatively-charged surface [82, 83]. It was reported that functionalization of nanopore below 5 nm tended to clog upon simple immersion of the chip in saline solution [84]. This challenge could be handled using conductive cell salination. In conductive cell salination, the flow of ions disturbed clogging due to saline molecules.

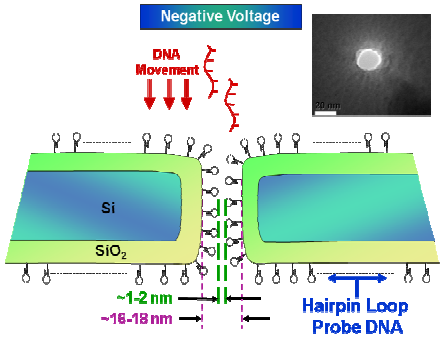

Figure 2.10 Solid-state nanopore functionalized with hair-pin loop DNA probes. The diameter of the nanopore is reduced to 2 nm after probe attachment. Reprinted by permission from Nature Publishing Group: Nature Nanotechnology [55], copyright (2007)

2.3 Detection of Circulating Tumor Cells (CTCs)

2.3.1 Metastasis

Carcinogenesis is a process by which normal cells are transformed into cancer cells on cellular and genetic level. It can be induced by chemical and physical factors [85-87]. Cancer cells can migrate into surrounding tissue and vasculature, travel in blood circulation to distant organs and form a secondary cellular colony. This process is called metastasis as shown in Figure 2.11. Epithelial cells which play very important structural and functional role in body organs are attached with each other and the tissue by cell-to-cell and cell-to-extracellular matrix (ECM) adhesion molecules. Cell-to-cell adhesion molecules include cadherins, while cell-to-ECM attachment involves integrins. Cadherins and integrins rely on rigid structure formed by actin and cytokeratin filaments. Normal epithelium cells are intact and immobile. Whereas mesenchymal cells like leukocytes and fibroblasts, have very relaxed organization. Tumor cell invasion involves transition from epithelial to mesenchymal cells (EMT). This transition is induced by transcriptional factor Twist. This transition also involves degradation of cell-to-cell adhesion, characterized by decrease in E-cadherins expression and epithelial markers like cytokeratin and increase in mesenchymal markers like vimentin. Mesenchymal like cancer cells can readily intravasate and extravasate by traversing basement membrane and endothelial barriers. During traversing, cancer cell has to adhere to ECM via appropriate integrins, which can allow cell to survive and proliferate. Otherwise, unattached cell not only stop growing but commit suicide [88-93].

2.3.2 Circulating Tumor Cells (CTCs)

When cancer cells traverse into blood stream, these are called circulating tumor cells (CTCs). The CTCs flow in the peripheral blood vessels with other cells. CTCs may cause subsequent growth of additional tumor in secondary tissues. The presence of CTC was first found by Ashworth in 1869 [94]. CTCs have high clinical diagnostic potential in oncology. Detection of CTCs can provide cancer progression information. Precise quantification of CTCs

can help in personalized medicine and monitoring the effectiveness of treatment. The number of CTCs in blood correlates with the survival rate of cancer patients. In one report, breast cancer patients who had less than 5 CTCs per 7.5 ml blood survived for an average of 7 months or more; while patients with 5 or more CTCs per 7.5 ml blood had just 2.7 survival months. The overall survival durations in these two groups were 10.1 month and 18 months respectively [95]. The detection of CTCs in the peripheral blood can be used for prognosis in breast, prostate and colorectal cancers [96-102].

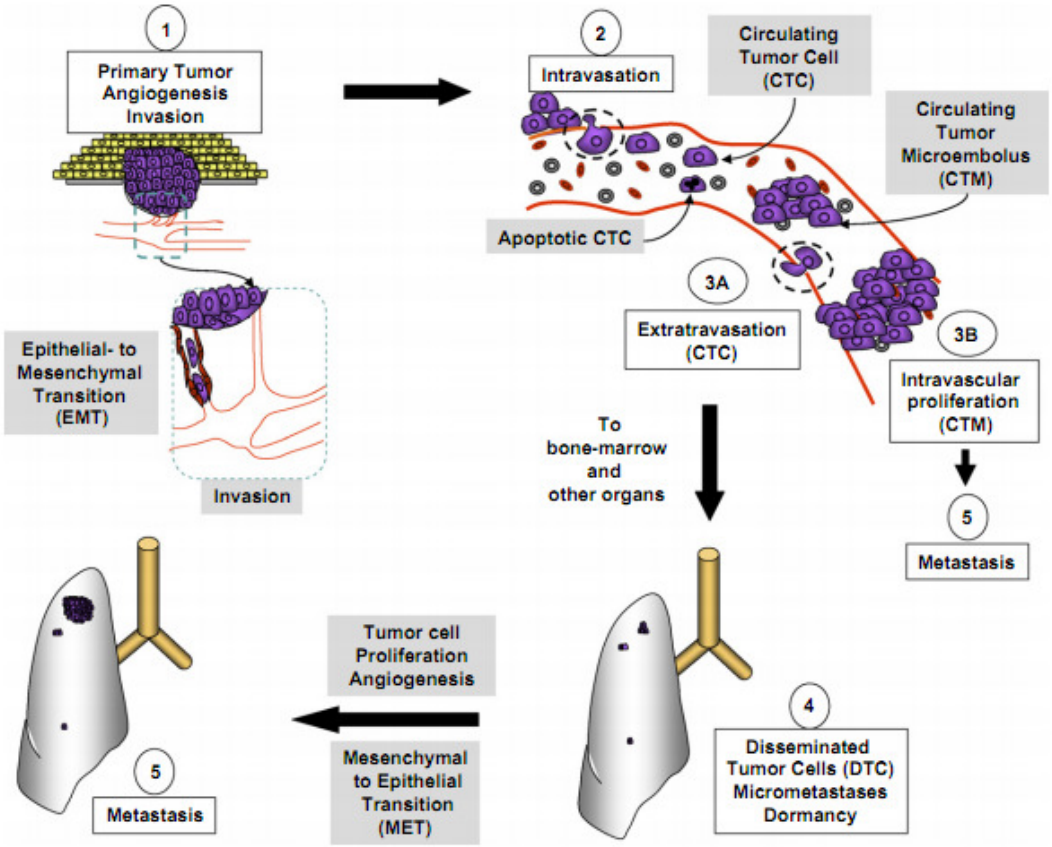

Figure 2.11 Main steps involved in the development of metastases, Reprinted by permission from Elsevier: Cancer Letters [89], copyright (2007)

2.3.3 CTCs Detection Techniques

There has been extensive work done for the detection of CTCs from blood stream. Early stage detection and quantification of CTC is a challenge as the CTCs are very low in number ranging 1 – 100 per milliliter of blood [103-108]. While there are approximately 10^6 white blood cells (WBCs) and 10^9 red blood cells (RBCs) in just 1 ml of blood [109]. All different cell types and their number is shown in Figure 2.12 [110]. Current CTC detection approaches either give lower than desired yield or involve fluorescent tags for counting. An illustration for current CTC detection methods is shown in Figure 2.13 [111]. Some of the processes are laboratory dependant and are very expensive requiring specialized equipment like optical flow cytometry. Description, advantages and limitations of current detection methods are covered in the following paragraphs.

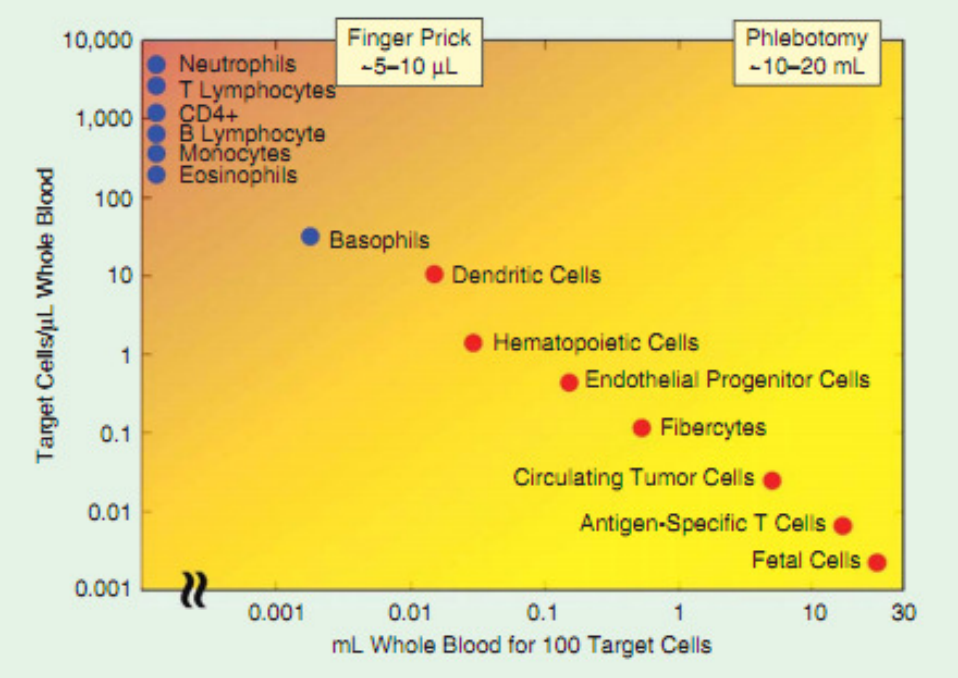

Figure 2.12 Different type of blood cells and their density in whole blood. Reprinted by permission from IEEE: IEEE Pulse [110], copyright (2011)

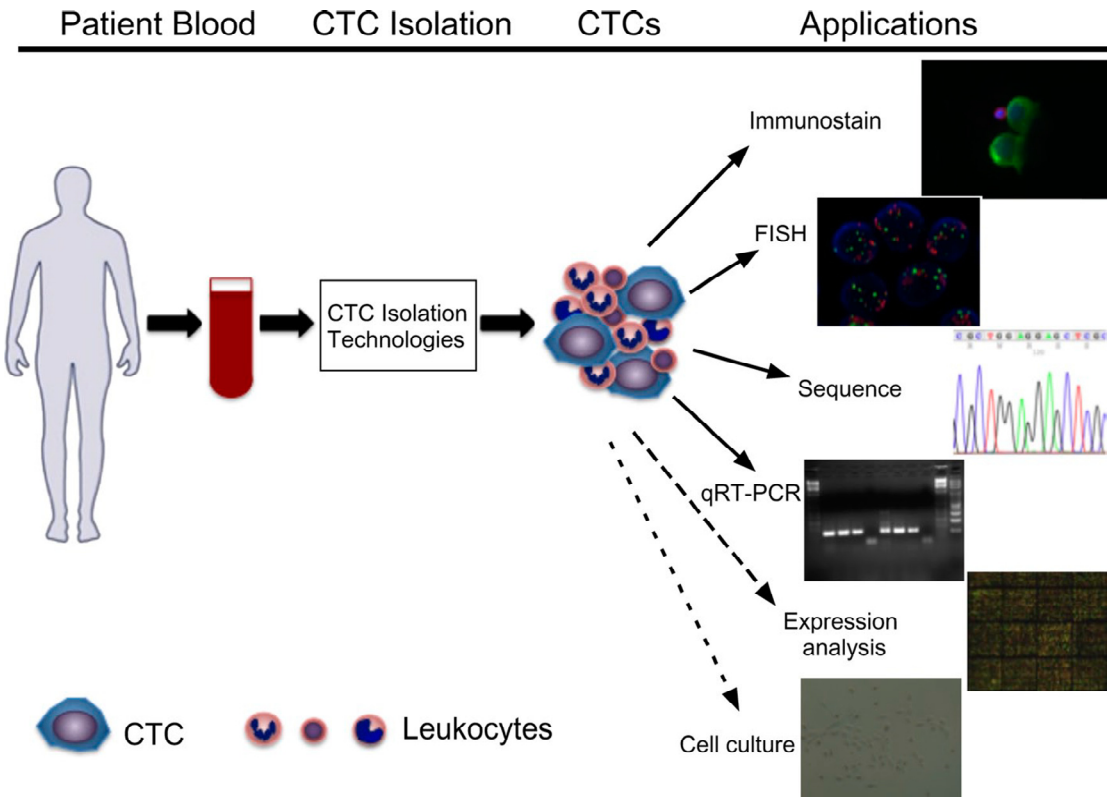

Figure 2.13 The blood from cancer patients is processed with different methods for CTCs isolation. Immunostaining for specific marker, FISH for genomic amplification and quantitative RT-PCR for specific DNA/RNA sequencing can be applied to CTCs. Printed with permission [111]

In immunomagnetic detection methods (MACS systems, magnetic beads), magnetic particles (bead or ferrofluids)-bound antibodies are mixed with whole blood or isolated mononuclear cells [112-114]. The mononuclear cells can be isolated using density gradient and centrifugation. Cells attached to beads due to antibody interactions are collected by magnetic force while other cells are left in the supernatant. A large number of leucocytes are still present with the target cells. Some immunomagnetic methods get rid of leucocytes by including negative selection of leucocytes with anti-CD 45 combined with positive selection with antibodies specific to epithelial cells such as EpCAM and Cytokeratins [115]. The output still

retains non malignant epithelial cells and loses tumor cells which do not show epithelial antigens. Cells separated using immunomagnetic method, are shown in Figure 2.14.

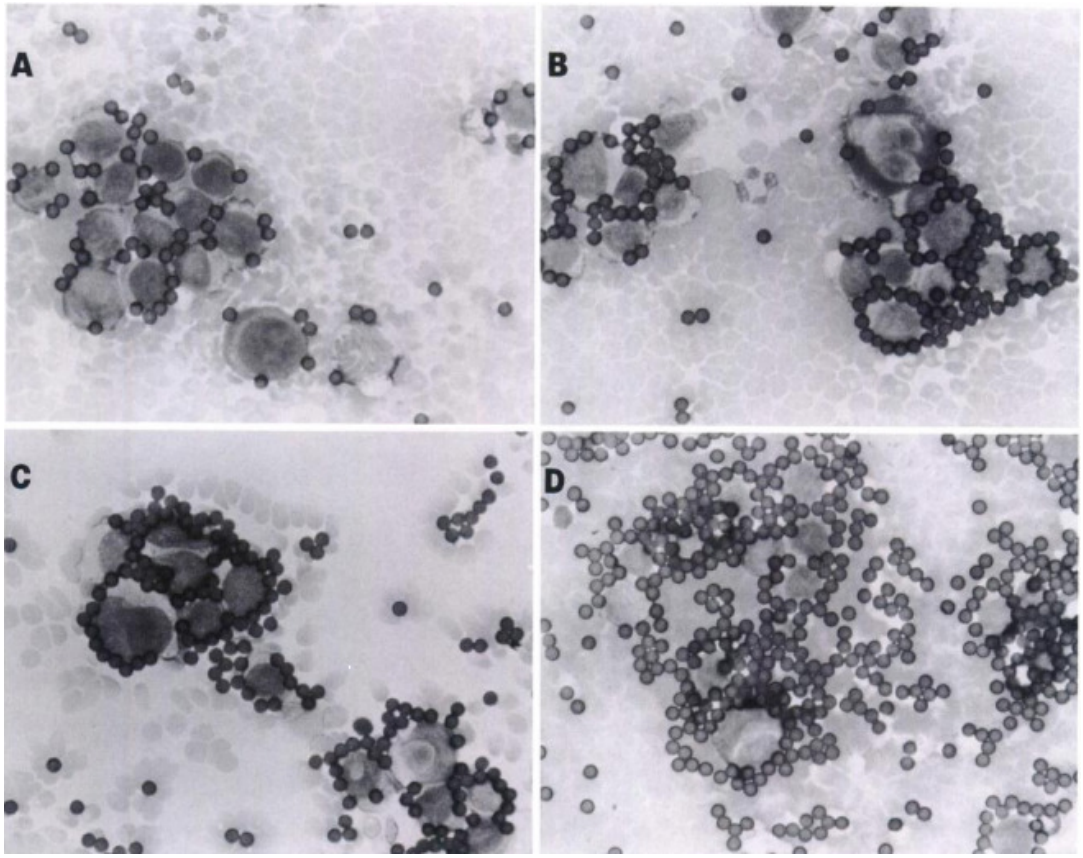

Figure 2.14 Different concentration of magnetic beads incubated with whole blood. The beads are attached with tumor cells. Reprinted with permission [112]

The CellSearch™ assay is a commercial system. It uses ferrofluids coated with EpCAM antibody to immunomagnetically capture epithelial cells. After separation and fixing, cells are labeled with fluorescent nuclear dye (DAPI), a fluorescent antibody (CD45) specific to leucocytes and fluorescent antibodies to cytokeratin, specific for epithelial cells. Cell-Spotter Analyzer is a fluorescent microscope which identifies the epithelial cells from other based on fluorescent colors [116].

Reverse Transcription Polymerase Chain Reaction (RT-PCR) method analyzes specific genes from CTCs. The important advantage of this technique is its sensitivity which is

considered highest, compared to other detection methods including immunomagnetic or CellSearch^{TM} assay. Sample is first enriched with epithelial cells followed by extraction of ribonucleic acid (RNA). Complementary DNA is synthesized and amplified from RNA followed by PCR product analysis using gel electrophoresis. RT-PCR can identify one cancer cell out of 10^7 normal cells. The use of this method is limited because it is almost impossible to get quantifiable data in the blood sample using RT-PCR; it gives false positives and is prone to physical contamination [117, 118].

Isolation by Size of Epithelial Tumor cells (ISET) is very simple CTC detection approach. It is based on the fact that most of the epithelial cells are larger in size than other peripheral blood cells. The blood is diluted with the buffer and filtered using polycarbonate membrane with the mean diameter of 8 µm. The epithelial cells being larger in size remain on the membrane after filtration [119, 120]. The cells are fluorescently labeled and scanned with laser cytometry. The diameter of cancer cell found in the breast cancer patient ranges from 29.8 µm to 33.9 µm. The breast tumor cells have been successfully isolated using ISET method [121]. In one report, Zabaglo et al. used ISET technique to isolate breast cancer cells (MCF7 and T47D) and reported more that 85% recovery [119]. It was found that not all the WBCs were smaller than 8 µm, their diameter ranged from 7 to 20 µm. So cells left on the polycarbonate membrane were mixture of WBCs, RBCs and target cells. Although the ISET method is very attractive but it needs laser scanning for post analysis.

Microchip technology and microfluidics are also used for CTCs detection. Nagrath et al. developed a unique microchip platform that had an array of microposts functionalized with EpCAM antibody [122]. When the whole blood was allowed to flow through the microposts at precisely controlled laminar flow conditions, the epithelial cells got attached with antibody as shown in Figure 2.15. They successfully identified CTCs in peripheral blood of the cancer patients with metastatic lung, prostate, pancreatic, breast and colon cancers. They identified

CTCs from 115 out of 116 patients with cancer. Their method looks attractive because it does not require any preprocessing of the whole blood but it require surface functionalization and post identification of captured cells with fluorescent tags.

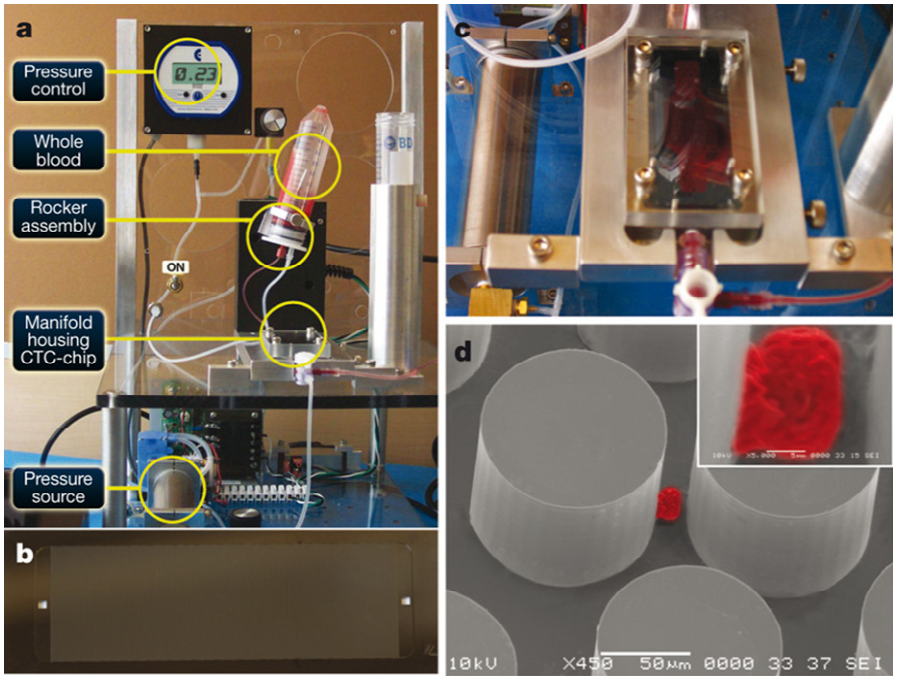

Figure 2.15 Setup for isolation of CTCs from whole blood using microchip technology. Reprinted with permission from Nature Publishing Group: Nature [122], copyright (2007)

2.4 Nano-Textured Scaffolds and Surfaces

2.4.1 Nano-Patterning and Nano-Texturing

Cell growth, orientation, adhesion and migration are greatly influenced by surface topographical features at micro and nanoscale [123, 124]. These features can be of any shape such as nanopores, fibers and ridges. Basement membrane is found as underlying layer for cellular structure and consists of extracellular matrix (ECM). ECM has porous structure with

fibrous collagen network [124]. ECM structure has many features at micro and nanoscale. Mimicking the ECM features can play crucial rule in understanding the cell behavior which would help in designing efficient artificial tissue and body implants. Nano-features also find a lot of applications in biosensing, nanoelectronics, proteomics and next generation light emitting diodes [22, 125, 126]. In biosensing applications, the nano-textured surfaces offer increased surface area for biomolecule attachment which can increase the efficiency of detection systems.

2.4.2 Cell Response to Textured Surfaces

It is well known that the surface topography and substrate mechanical properties play important role in cell response. Grooves are one of the most commonly used features used to study cell responses. Generally grooves are patterned in an array form with certain orientation [127-129]. Orientation of the cells has been found to increase with increasing depth of the grooves, and it has been seen to decrease with increasing groove width [130]. Martinez et at. studied the effects of pore size and hydrophobicity of the surface on the fibroblast cell growth. They found that pore size played a larger role than hydrophobicity of the material in determining the tissue response [131]. In general, cell adhesion, migration and growth rates are greater on the rougher surfaces as compared with the smooth ones. Cell response on the wet etched and reactive ion etched surfaces was also studied in this report. It has been found that the primary cell line preferred rougher surfaces created by reactive ion etching while transformed cells preferred wet etched smoother surfaces [131]. Miller et al. studied the effects of nano-texturing on endothelial and smooth muscle cells [132]. They synthesized two type of substrates, one conventional poly(lactic-co-glycolic acid) (PLGA) substrate and one NaOH treated PLGA substrate. The NaOH treatment of PLGA substrates produced nano-texturing. They reported more smooth muscle cell growth on the NaOH treated PLGA substrate as compared with the conventional PLGA substrate [132]. While endothelial cells showed lesser growth on NaOH treated nano-textured substrate as compared with the conventional one. They also synthesized PLGA substrate by first casting PDMS on NaOH treated PLGA substrate and then casting

PLGA again on the PDMS substrate to eliminate the changes in chemical composition of NaOH treated PLGA substrates as shown in Figure 2.16. They further investigated and found that lesser endothelial cell growth was due to chemical changes of the substrate due to NaOH treatment (not the nano-texturing). They concluded that nano-texturing of PLGA substrate had increased the cell growth of both of the endothelial and smooth muscle cells [132].

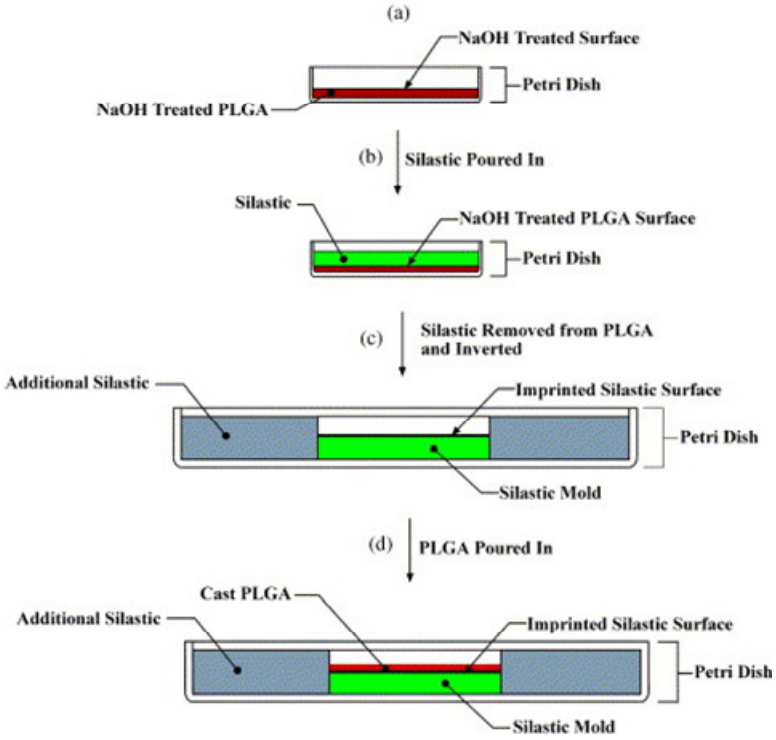

Figure 2.16 Process flow to synthesize nano-textured PLGA scaffold with eliminated chemical change effects. Reprinted by permission from Elsevier: Biomaterials [132], copyright (2004)

2.5 Break-junctions

2.5.1 Break-junctions for Biosensing

Break-junctions are used to electrical detection of DNA, protein biomarkers and other pathogens [133]. The break-junctions are fabricated by inducing a nanogap between two metallic lines [134]. The nanogap area is the most important part of the break-junctions as the target molecule has to get attached on this place. This is the simplest method to study single

molecule charge conduction and analyze their electrical properties. When the target molecule makes a bridge between two electrodes, current starts flowing through the molecule under applied voltage as shown in Figure 2.17 [135]. The amplitude of the current is correlated to electrical properties of bio-molecules.

As the gap between the break-junctions should be few nanometers, therefore its fabrication is a challenging process. There are two basic methods to make the break-junctions from already patterned electrodes, mechanical method and electromigration method. In a mechanical break-junction fabrication process, a bridge of metal is suspended over flexible substrate [136]. The junctions can be broken by bending the flexible substrate as shown in Figure 2.18. In electromigration technique, a large current density or electron movement is produced in metallic electrodes by the application of external electric field. If there is any charged defect in the metal layer, the momentum of electron is transferred to the defect. The transferred momentum builds up larger and larger with the passage of time and eventually results into movement of metal atoms away from the defect causing the fabrication of break-junctions as shown in Figure 2.19 [137].

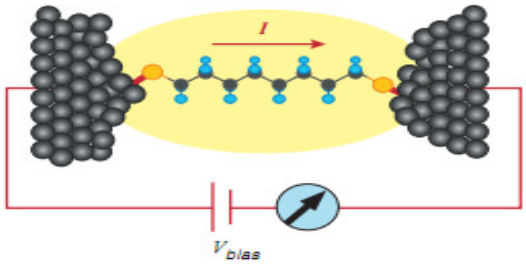

Figure 2.17 Schematic of electrical conduction through single molecule chemically attached to two facing electrodes. Reprinted with permission [135].

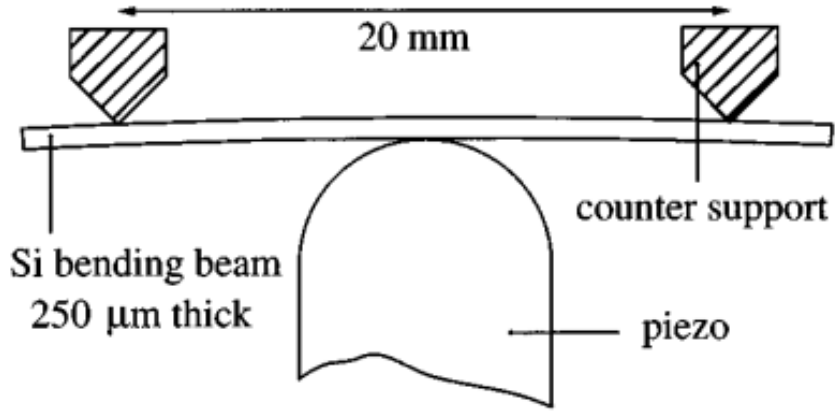

Figure 2.18 Setup for controlled mechanical bending to fabricate break-junctions. Reprinted by permission from American Institute of Physics: Applied Physics Letters [136], copyright (1995)

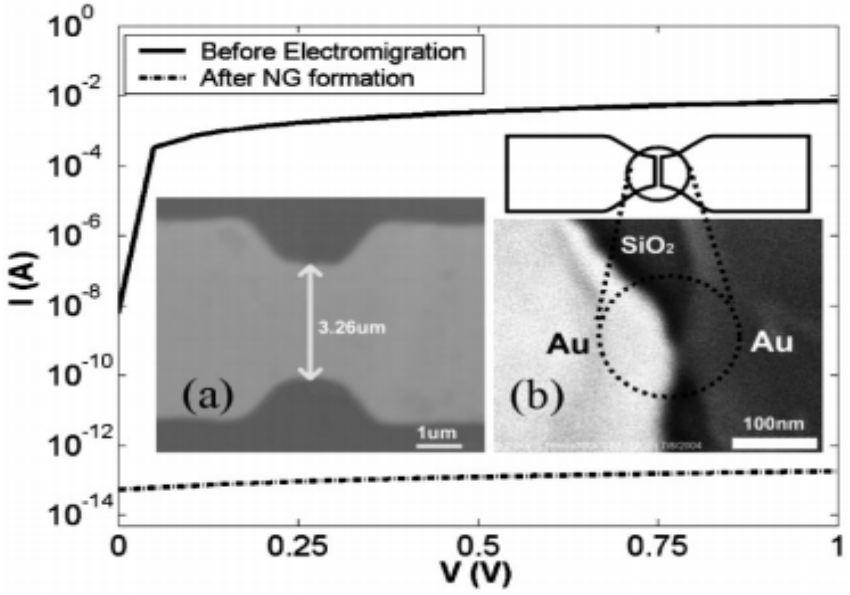

Figure 2.19 (a) Metallic line before electromigration. (b) Break-junction formed after electromigration. Reprinted by permission from American Institute of Physics: Applied Physics Letters [137], copyright (2005)

2.5.2 Fabrication of Break-junctions

There are many fabrication processes to make metallic break-junctions. Their advantages and disadvantages are described in following sub sections.

2.5.2.1 Mechanically Controllable Fabrication of Break-junctions

Break-junctions can be fabricated by microfabrication methods to make mechanically controllable break-junctions [136]. In one report, oxidized Si wafer was patterned using e-beam lithography followed by the evaporation of 80 nm gold layer. The second layer of Al was deposited over the whole except gold features. This can be achieved using photolithography. Dry etching was used to etch silicon dioxide while metallic layers were acting as a mask. After RIE, wet chemical etching was used to etch Si in inverted pyramid shape. The final device consisted of two cantilever beams connected by 100 nm wide wire. The mechanical bending created a fracture in gold wire, thus breaking the junction with a small nanogap as shown in Figure 2.20.

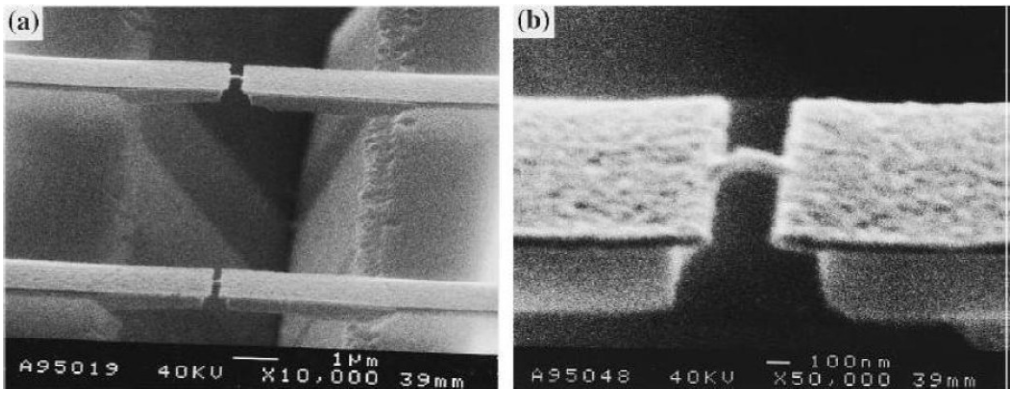

Figure 2.20 (a) Si chip after dry and wet chemical etching. (b) SEM image of two cantilevers connected by Au wire. Reprinted by permission from American Institute of Physics: Applied Physics Letters [136], copyright (1995)

2.5.2.2 Shadow Evaporation Fabrication of Break-junctions

Break-junctions can be fabricated with e-beam lithography and shadow evaporation followed by electromigration. In one report, Park et al. used e-beam lithography to a 200 nm

long suspended resist bridge, 400 nm above the oxide surface. A film of chrome (3.5 nm) was evaporated followed by 10 nm Au deposition at an angle of ±15^{o} with respect to the normal of the substrate [138]. The two gold wires were fabricated by the same shadow deposition of the Au. Another 3.5 nm of chrome and 80 nm of Au were deposited without any angle to connect the nanowires and gold pads patterned with photolithography. The nanogap was created by using the electromigration. A voltage was applied across the two Au pads which resulted into flow of electrical current. At certain voltage, sudden drop in current was noticed that indicated the breakdown of Au junctions. The break-junctions were generally fractured at regions where two shadow-evaporated electrodes overlapped because the thin metal layer had highest resistance. The SEM micrographs of break-junctions before and after electromigration are shown in Figure 2.21 [138].

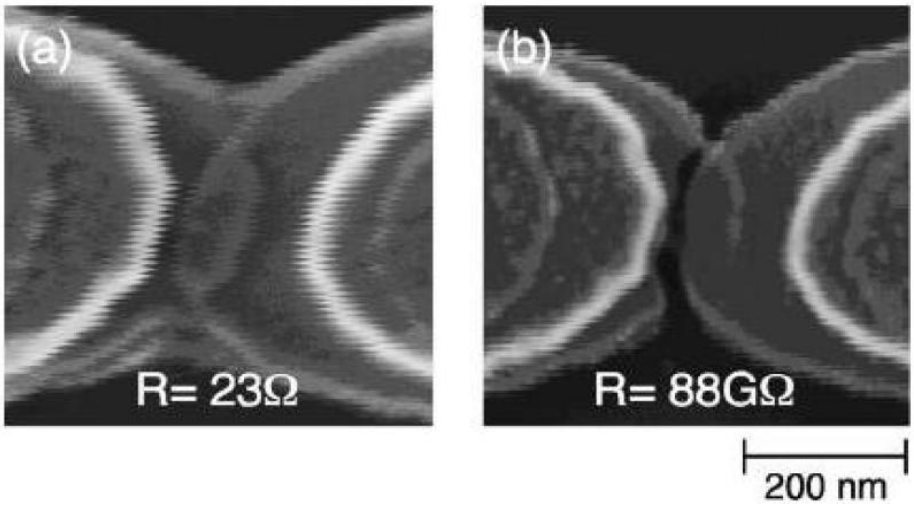

Figure 2.21 FESEM micrographs of break-junctions (a) before and (b) after electromigration. Reprinted by permission from American Institute of Physics: Applied Physics Letters [138], copyright (1999)

2.5.2.3 E-Beam Deposition for Fabrication of Break-junctions

In this fabrication process, silicon wafer was oxidized to the thickness of 1 µm followed by low pressure chemical vapor deposition (LPCVD) of silicon nitride film. First, e-beam lithography

was used to pattern a few mm long slit with a diameter of 100-150 nm. The pattern was transferred to underlying layer of nitride using RIE. The wet chemical etching of oxide using BHF etching process left two overhanging silicon nitride structures as shown in Figure 2.22 [139]. Thin layer of Au was sputtered onto the nitride membrane. Free standing carbon nanowire was deposited on the overhanging Au/Si nitride structure using e-beam exposure. The carbon had started growing from the edge of one overhanging gold layer towards the opposite overhanging structure. The growth of carbon nanowires could be stopped at any time to have break-junction of specific nanogaps. The minimum gap fabricated by using this method was less than 3 nm as shown in Figure 2.23 [139].

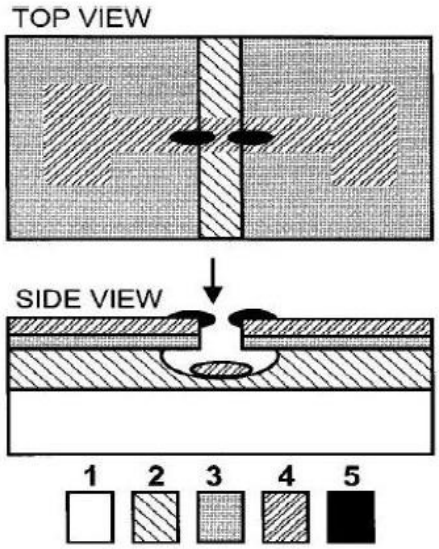

Figure 2.22 Schematic showing the fabrication process of gold break-junctions using e-beam deposition. (1) Si wafer (2) Si dioxide (3) Si nitride (4) gold (5) e-beam deposited carbon electrode. Reprinted by permission from American Institute of Physics [139], copyright (1997)

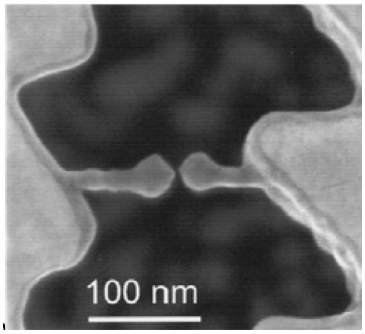

Figure 2.23 SEM micrograph of two carbon electrodes fabricated with e-beam deposition. Reprinted by permission from American Institute of Physics [139], copyright (1997)

2.5.2.4 Fabrication of Step Junctions

Choi et al. reported a simple method to fabricate a nanoscale gap between two metal electrodes without e-beam lithography and electromigration. They made use of positive slope of the pattern edge in the positive photoresist. The gold was evaporated followed by lift-off process. The negative slope of metal feature acted as a shadow for second deposition of thin gold film. Using this method, a nanoscale gap was successfully made, denoted as step junction. The process flow of step junction method is shown in Figure 2.24 [140].

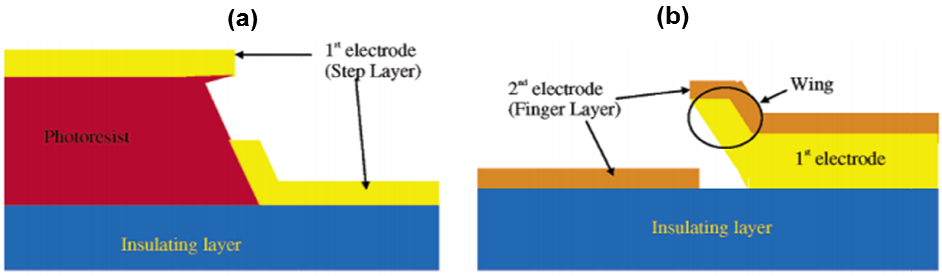

Figure 2.24 Process flow for the fabrication of step junctions. (a) After evaporation of first electrode/step layer. (b) After evaporation of second electrode layer/finger layer. The lift off was performed after evaporation of first electrode. Reprinted by permission from American Chemical Society: Nano Letters [140], copyright (2004)

CHAPTER 3

NANOPORE BASED SOLID-STATE SENSORS FOR DNA ANALYSIS

3.1 Thermal Shrinking of Solid-State Nanopores by Direct Heating

3.1.1 Introduction

Biological nanopores inspired the fabrication of solid-state nanopores. Solid-state nanopores have emerged as novel platform for single molecule analysis [141, 142]. Solid-state nanopores have many advantages over protein nanopores because they are more stable than protein nanopores under various experimental conditions including pH, salinity and temperature [143].

A biomolecule give significant current blockade pulsed during translocation through the nanopore. The nanopore diameter should be comparable to the size of the translocating species. The conventional nanopore fabrication processes can only synthesize nanopores with initial diameters larger than the size of species of interest [63, 144, 145]. The solid-state nanopore diameter is generally reduced using Transmission Electron Microscope (TEM) and Field Emission Scanning Electron Microscope (FESEM) to induce the electronic shrinking [64] and Focused Ion Beam (FIB) for the ion beam sculpting processes [62]. The viscous flow of SiO2 membrane is induced by TEM electron beam exposure of optimal intensity during shrinking process. The nanopore can shrinks or expands based on the surface-tension-driven mass flow. The nanopore obeying the condition of $r < t/2$, would shrink during TEM e-beam exposure where r is the radius of the nanopore and t is the thickness of the membrane in which nanopore is made. TEM e-beam exposure depletes oxygen content from the oxide area surrounding the nanopore [64].

The solid-state nanopore shrinking with FESEM is due to radiolysis. High energy FESEM electron beam disturbs crystalline structure of the nanopore. During FESEM shrinking process, Si and oxygen atoms are diffused towards the edge of the nanopore to overcome the crystalline defects present at the edge. Different acceleration voltages during FESEM exposure offer varying shrinking rates [52]. Under FESEM e-beam, the nanopore was reported to be shrinking irrespectively of the ratio of the nanopore's diameter and membrane thickness [52].

The nanopore is exposed to an energetic ion beam during FIB sculpting process. The accelerating ions can drill a nanopore in a thin membrane due to sputtering of the surface. The FIB beam can also cause nanopore shrinking due to atom diffusion or surface-tension-driven mass flow [62]. The FIB sculpting process is also dependent on the substrate temperature. It was reported that the nanopore shrank at room temperature while it expanded at temperatures close to 0 ^{o}C [62].

Material's chemical composition around the nanopore periphery changes during TEM or FESEM shrinking methods. This produces random modifications of nanopore surface properties. These shrinking methods make the nanopore unfavorable for bio-analysis due to increased surface charge and electrical noise. Secondly, these shrinking processes can only process one nanopore at a time and hence its time consuming. We report a simple to shrink nanopores using direct thermal heating. High temperature treatment (>1000 ^{o}C), or annealing, promoted the viscous flow of the silicon dioxide (SiO_2) membrane and resulted in morphological changes that depend on the ratio of nanopore diameter to membrane thickness. During high temperature annealing process, residual stress in the SiO_2 membrane was also reduced. Surface material composition of the nanopore did not change during thermal shrinking porcess. High temperature annealing has been used extensively in semiconductor industry to reduce leakage current [146], repair gate oxide damage [147] and to minimize residual stress [148].

3.1.2 Materials and Methods

3.1.2.1 Solid-State Nanopore Fabrication and Characterization Process

First of all, double-side-polished, boron-doped silicon (100) wafer (Wafer World, Inc) was oxidized to thickness of 400 nm. Positive photoresist (PR) S1813 (Shipley Microposit J2 PR) was spin coated on one side of the wafer. The wafer was exposed to G-line photolithography equipment and square windows were opened after development process. Then PR was coated on the other side. Buffered hydrofluoric acid wet etching process was used to remove oxide from square windows. The wafer was then washed with de-ionized (DI) water and dried with nitrogen. PR was removed by leaving wafer inside acetone solution for 15 minutes. Free-standing oxide membranes were fabricated by anisotropic etching using 20% tetramethylammonium hydroxide (TMAH) in DI water at 90 ^{o}C (J.T. baker, Inc). TMAH etching was stopped once 30x30 μm^2 square windows were achieved in SiO_2. Reactive Ion Etching (RIE) was used to reduced the thickness of oxide membrane to 300 nm by using tetraflouromethane (CF_4) at 100 watts power and gas flow rate of 15 sccm. The etch rate of the RIE was characterized using a reflectometer (Ocean Optics NC-UV-VIS Reflectometer). All samples were cleaned with piranha solution before FIB (ZEISS 1540XB) drilling. The free-standing oxide membranes were drilled with the FIB to create the initial nanopores. The FIB process was first optimized in terms of drilling time and milling current keeping acceleration voltage (30 kV) fixed. HRTEM (Hitachi H-9500) operating at 300 kV was used to image and characterize nanopores.

3.1.2.2 High temperature shrinking process

The thermal heating furnace (Lindberg Furnace) was turned on and temperature was raised to desired range. All nanopore samples were put together in a horizontal carrier inside the heating furnace. The samples were allowed to heat up for 30 seconds before starting the

actual processing time. The flow rate of nitrogen gas was maintained at 20 sccm throughout the thermal shrinking process. At fixed time points, the samples were taken out of furnace and allowed to cool down to room temperature. All the samples were cleaned with argon-oxygen plasma (Technics Micro-RIE Series 800 plasma system) for 5 minutes before and after every thermal processing step. The plasma cleaning was used to avoid hydrocarbon contamination.

3.1.2.3 Results and discussion

The schematic in Figure 3.1 depicts the membrane formed after TMAH etching. Bulk membrane composition was determined by energy dispersive X-ray spectroscopy (EDS). It was reported that the free standing membranes contained only Si and O, with 31% Si and 69% O as shown in Figure 3.2. This is in good agreement with the expected SiO_2 stoichiometric ratio of 33.33% Si and 66.66 % O (SiO_2). FIB was used to drill nanopores in free-standing SiO_2 membranes [74]. FIB drilled nanopores in the diameter range of 100-300 nm. The high resolution transmission electron microscope (HRTEM, Hitachi H-9500) operating at 300 kV was used to image the nanopores after FIB drilling as shown in Figure 3.2 (inset). The nanopore chips were kept in heating furnace (Lindberg Furnace) at specific temperatures during shrinking process while flow rate of nitrogen was maintained at 20 sccm.

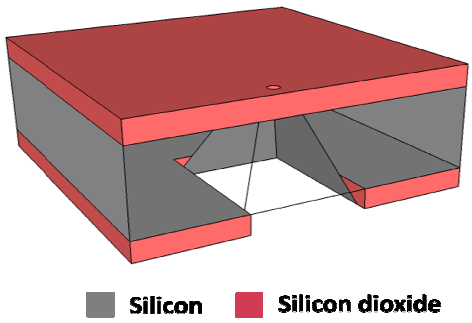

Figure 3.1 Schematic shows the free standing oxide membrane having small pore drilled with FIB. Reprinted with permission [48]

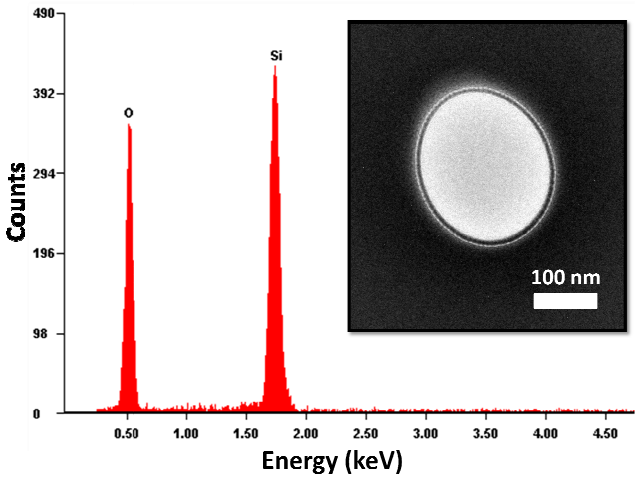

Figure 3.2 EDS spectrum for oxide membrane is shown which confirms the presence of only Si and O. TEM micrograph shows the nanopore drilled in oxide membrane (Inset). Reprinted with permission [48]

Nanopores start shrinking or expanding when left at high temperature (1000 ^{o}C - 1250 ^{o}C), contradicting previous findings [64]. The nanopore with a diameter of 250 nm was reduced to 3 nm at 1150 ^{o}C as shown in Figure 3.3. The nanopores were imaged with TEM after each temperature processing step to characterize the process. After each thermal shrinking step, the chips were unloaded from furnace and allowed to cool down to room temperature. It was observed that the thermal shrinking process had very little or no effect on the diameter of the nanopore at temperatures below 1000 ^{o}C. At low temperature, the oxide layer would not be relaxed to an extent that it would start changing pore morphology. When the nanopores were processed at a higher temperature (> 1250 ^{o}C), the oxide membranes either broke down due to high thermal stress or the shrinking process was too fast to control. At higher temperatures, it was difficult to control the shrinking process especially for nanopores with diameters in few tens of nm [149]. For example, a nanopore having initial diameter of 270 nm, when processed at 1250 ^{o}C, the nanopore was closed after 4 minutes due to an increased shrinking rate as shown in Figure 3.4.

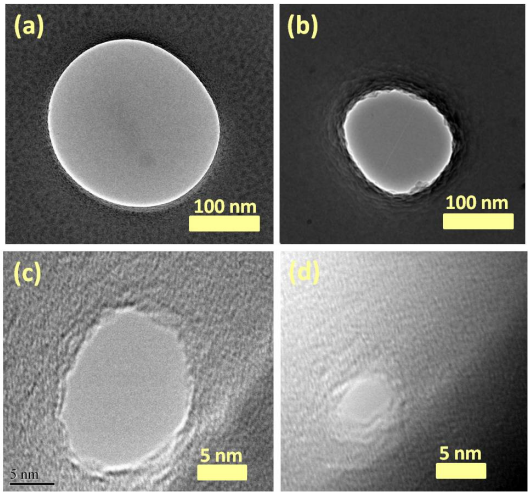

Figure 3.3 (a) TEM micrograph of nanopore as drilled with FIB. Its diameter is ~250 nm. (b) After 5 minutes of thermal shrinking at 1150 ^{o}C. Nanopore diameter is ~150 nm. (c) After 10 minutes of thermal shrinking at 1150 ^{o}C. Nanopore diameter is ~20 nm. (d) After 10 minutes and 40 secs of thermal shrinking at 1150 ^{o}C. Nanopore diameter is ~3 nm. Reprinted with permission [48]]

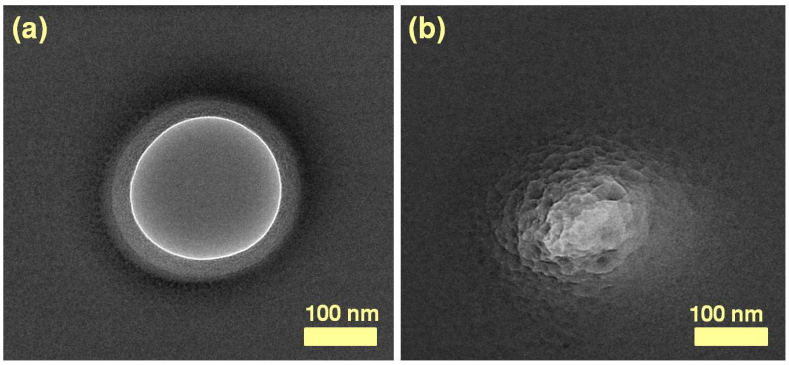

Figure 3.4 (a) TEM micrograph of nanopore as drilled with FIB with diameter of ~270 nm. (b) Nanopore closed after 4 minutes of thermal shrinking at 1250 ^{o}C. Reprinted with permission [48]

It was concluded that shrinking and expansion rates increased at higher processing temperature. When the nanopore diameter was larger than the membrane thickness, the nanopore was found to be expanding in diameter instead of shrinking. The nanopore diameter

increased from 350 nm to 1.5 µm when processed for 50 minutes at 1150 °C (Figure 3.5). It was due to the fact that initial nanopore diameter was larger (350 nm) than the membrane thickness (300 nm). It was reported that direct heating can be used to shrink or expand the nanopore based on the ratio of initial nanopore diameter to oxide membrane thickness in which nanopore was drilled. The temperature itself had no effect on whether the nanopore would shrink or expand. These shrinking and expanding mechanisms can be explained by the surface-tension-driven mass flow which induced viscous flow of oxide film.

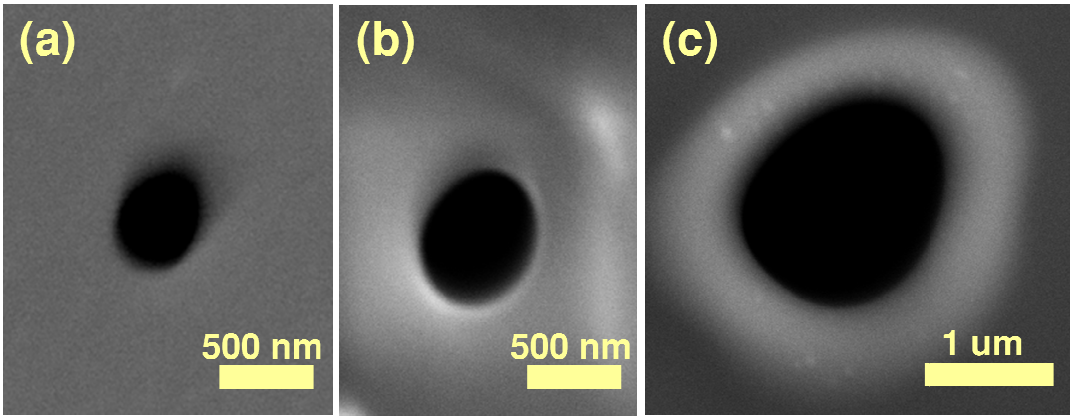

Figure 3.5 (a) SEM micrograph of the nanopore as drilled with FIB in 300 nm thick oxide membrane. The nanopore diameter was ~300 nm. (b) Nanopore diameter increased to ~650 nm when processed at 1150 °C for 15 minutes. (c) Nanopore diameter was further increased to ~1.5 µm when processed at 1150 °C for 50 minutes. Reprinted with permission [48]

The thermal process for nanopore shrinking was characterized at different processing temperatures as shown in Figure 3.6. The nanopore was found to have no shrinking or expansion when processed at 900 °C. When the processing temperature was increased above 1000 °C, the nanopore morphology started changing due to the diffusion and the viscous flow of oxide film. The average shrinking rate was approximately 22 nm/min at 1150 °C, which increased to 80 nm/min at 1250 °C. The shrinking process was difficult to control at higher

processing temperatures. When the nanopore diameter was reduced to below ~20 nm, processing temperature < 1150 ^{o}C was used to accurately control the shrinking.

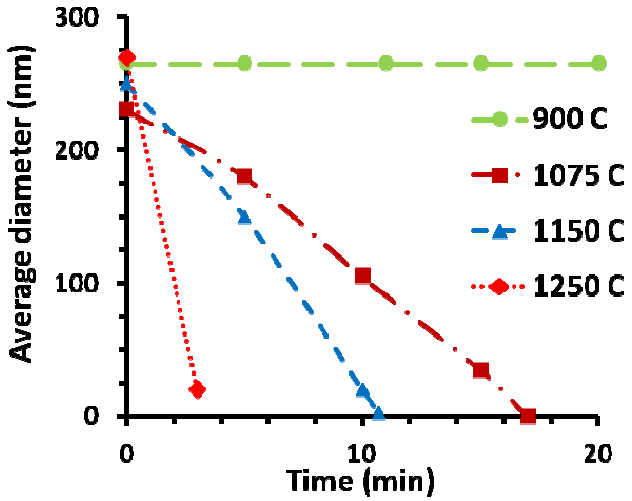

Figure 3.6 Plot shows the nanopore shrinking rates at different processing temperatures. The nanopore neither shrink nor expand at 900 ^{o}C. The nanopore shrinking rate increased with increasing processing temperature. Thermal shrinking processes show almost linear behavior at all temperatures. Reprinted with permission [48]

During nanopore shrinking process, there is the possibility of hydrocarbon contamination that can affect nanopore shrinkage dynamics. For that, all the chips were cleaned with Piranha solution (1:1, sulfuric acid:hydrogen peroxide) before nanopore drilling with FIB. The chips were cleaned with argon-oxygen plasma for 5 minutes before and after each shrinking step. The chips were also cleaned with piranha solution for 5 minutes after TEM imaging to find out whether the cleaning had any effect on the nanopore diameter. TEM images revealed that the nanopore diameter remained the constant after piranha cleaning. The local EDS analysis did not show any traces of hydrocarbons as shown in Table 3.1. Secondly, the nanopore opened or closed based on the ratio of nanopore radius to oxide membrane thickness, which was a strong indication that hydrocarbon contamination was not involved in the shrinking process.

Table 3.1 EDS Analysis of the Nanopore after Different Processing Steps. Reprinted with permission [48]

Processing Condition	Element	Weight %	Atomic %
Before FIB Drilling	O	55.97	69.06
	Si	44.03	30.94
After FIB Drilling	O	55.60	68.73
	Si	44.40	31.27
After Heating	O	56.33	69.37
	Si	43.67	30.63

The solid-state nanopore shrinkage and expansion due to thermal heating can be explained by taking into account the surface tension of the viscous oxide membrane [64]. At higher temperature, the oxide membrane softens and deforms to find a structural morphology with lowest possible surface free energy *F*. For simplicity, we considered nanopore is of cylindrical shape with radius *r* and membrane thickness *t*. The change in free energy with respect to radius can be calculated using the mathematical relation $\Delta F = \gamma \Delta A = 2\pi\gamma\ (rt - r^2)$, where γ is the surface tension of the fluid and ΔA is the change in surface area [64, 150]. It can be deduced from the above equation that surface free energy of the nanopore having $r < t/2$ can be lowered by reducing *r*, whereas it can be lowered for nanopores having $r > t/2$ by increasing *r* [150]. The ratio of nanopore radius to oxide membrane thickness is considered most important factors in determining whether the nanopore will shrink or expand. The ratio phenomenon was also verified experimentally. A nanopore with a diameter of 250 nm drilled in 300 nm oxide membrane shrank (Figure 3.3) whereas a 350 nm diameter nanopore in 300 nm membrane expanded (Figure 3.5). Nanopore shrinking process similar to TEM shrinking can be achieved by direct thermal heating of the nanopore. But TEM can only process one nanopore at a time whereas this approach can process a whole wafer in one run. We believe that viscous flow is induced in the oxide membranes which results in nanopores shrinking or expanding. Similar dynamics of nanopore closing and opening have been reported in films of mercury and air holes

in water sheets [151]. The micrometer scale holes were used in these studies. The larger holes increased in size while the smaller holes closed down due to surface tension [151]. Similar shrinking mechanism have been observed when 20 nm thick gold sheets with 10-30 nm pores were subjected to an high temperature annealing process [149]. It was reported that nanopores with diameters smaller than the thickness of gold film tend to shrink whereas nanopores with diameters larger than the film thickness tend to expand during the thermal annealing process [149]. Similar diffusion kinetics may be applicable during high temperature process of nanopore shrinking.

3.1.3 Conclusions

In conclusion, we demonstrated a new technique to shrink nanopores in oxide membranes with few nanometer precision. The shrinking process is controlled and repeatable. In comparison with other methods, our shrinking process can be used to shrink many nanopores chips in one run. We processed 5-10 dyes in one run and achieved similar shrinking rates. Chemical composition of the nanopore walls remained unchanged during thermal shrinking process. This is one of the biggest advantage of our method as nanopore surface charges and its chemical composition play very critical role during DNA and protein translocation experiments. The oxide layer is softened under high temperature and is allowed to diffuse due to surface-tension-driven mass flow of viscous oxide.

3.2 Nanopore Shrinking with Pulsed Plasma Polymer Deposition

3.2.1 Introduction

The use of α-Hemolysin protein nanopore for DNA translocations has inspired development of solid-state nanopores for DNA and protein analysis [19, 58, 152, 153]. Fabrication of solid state nanopores have been stimulated by limited capabilities of biological

nanopores under varying experimental conditions like temperature, PH, salinity and mechanical properties. Fabrication of solid-state nanopore has been reported with good control on nanopore diameter and channel length. The techniques used to fabricate the solid state nanopores include focused ion or electron beam sculpting, transmission electron beam (TEM) drilling, and feedback chemical etching [59, 63]. Translocation of DNA molecules through nanopores is performed by using two compartments setup separated by nanopore device. When the negatively charged DNA passes through the nanopore under applied potential, it gives characteristic current blockade pulses. Nanopore biosensors have been used to study various biophysical properties including DNA stretching [32], transducing ligand binding mechanism into electrochemical signals [154], DNA charge measurements [17], and discriminating single base mismatch between target DNA molecules [55]. The nanopore diameter can be reduced by using shrinking or deposition processes. TEM or field emission scanning electron microscope shrinking has been investigated by different research groups but only smaller nanopores can be reduced by these approaches. It has been reported that nanopore radius would shrink only when it satisfies the condition $r < h/2$, where r is the radius of the nanopore and h is the thickness of the oxide membrane [64]. Conventional deposition method requires atomic layer deposition technique which is a relatively time consuming process [54]. Moreover, nanopore are fabricated in SiO_2 or Si_3N_4 membranes which limits the control on the nanopore surface properties. Thus further functionalization steps are required for nanopore surface treatment and modification. Therefore there is a need for nanopore fabrication approaches that are not limited to the initial size of the nanopore and which can give control on surface composition while reducing the nanopore diameter.

We report a rapid solid-state nanopore fabrication and shrinking process with *in situ* control of surface properties. Pulsed plasma polymer film (PPPF) deposition technique has been employed to control the surface properties of deposited layer. Nanopore surface wettability, surface cross linking chemistry and density of surface functional groups were

controlled by changing the duty cycle of applied voltage. The nanopores showed linear current-voltage (I-V) characteristics at reduced diameter with desired surface functional group density. Our approach also has capabilities of shrinking easily-fabricated larger nanopores to nanometer diameter with control on the deposition rate. An array of nanopores can be shrinked uniformly by using this approach.

3.2.2 Materials and Methods

3.2.2.1 Fabrication Process

The process started with 300 nm oxidation of double side polished Si wafer. Photolithography was used to open square etch-start windows on one side of the Si wafer. The process continued with wet etching of SiO_2 with buffered hydrofluoric acid (BHF). Silicon was etched through square openings using tetramethylammonium hydroxide (TMAH) anisotropic wet etching at 90 ^{o}C and 20% concentration in DI water. TMAH etch stopped once a square window of 70 x 70 µm in SiO_2 was reached. The thickness of SiO_2 membrane was then reduced to 30 nm by reactive ion etching (RIE) using tetraflouromethane at 100 watts. The gas flow pressure of 20 sccm was maintained during RIE process. Dry etch rate of RIE was characterized using ellipsometer before processing the membranes. Dry etching of both side (Front and Back) was considered to estimate the membrane thickness after RIE process. Focused ion beam (FIB) was used to drill small pores of diameter ranging 100 – 400 nm. A 30 kV acceleration voltage was used for FIB drilling using gallium ions. Different milling currents (1 pA, 2 pA, 5 pA and 10 pA) and FIB drilling times (10 – 30 secs) were used to drill nanopores of diameters ranging between 100–400 nm.

3.2.2.2 Pulsed Plasma Polymer Film (PPPF) Deposition

Plasma polymer film deposition was carried out using a home built plasma reactor system [155]. The chips with the nanopores to be coated were placed on the center of the base plate of the 6 inch conical reactor. The chips were subjected initially to 30 second exposure to a pulsed

Ar plasma for cleaning purpose. After cleaning step, the Ar flow was terminated and the plasma polymerization of the methacrylic acid (MAA) monomer was initiated. The RF frequency used for plasma discharge was 13.56 MHz. The power inputs were 160 W and 200 W for pulsed and continuous wave plasma respectively. The plasma pulse widths used, were in millisecond range, with specific plasma on/off ratio for each run set independently. MAA monomer pressure employed was 160 mTorr for all deposition runs. The MAA was outgassed two times by freeze drying before using for deposition. Prime Si wafer substrates were used for the XPS and polymer deposition rate studies. Transparent KBr disks were used for obtaining the FT-IR spectra of polymer film. The polymer deposition process was characterized before employing onto oxide membrane containing SiO_2 nanopore.

3.2.2.3 Measurement Setup

The *I-V* measurements were performed in aqueous solution of 1 M potassium chloride (KCl), using Ag/AgCl electrodes. All measurements were recorded using an Axon 200B amplifier operated in resistive feedback mode. The whole measuring device was placed inside a grounded metallic Faraday cage to reduce the environmental noise. The recorded amplified signal was fed to a Digidata 1440A data acquisition system (Axon Instruments). The data acquisition system was controlled with PClamp 2.0 software. All the measurements were carried out by using a two compartment setup where the nanopore chip was sandwiched between two teflon blocks [55]. PDMS) gaskets were used to make sure that there was no leakage current. The PDMS gaskets were synthesized by mixing PDMS base and curing agent at 10:1 (w/w) ratio in a petri dish. The base and curing agent mixture was left on the hot plate at 100 ^{o}C for 12 hours. The PDMS solidified due to polymerization. The solid PDMS was cut into the gaskets of required dimensions.

3.2.2.4 DNA Translocation Experiment

Double-stranded λ-DNA was used as received. The length of λ-DNA was 48.5 kbp. The λ-DNA concentration used in translocation experiment was 3 nM. The current was first allowed to stabilize for few minutes before putting λ-DNA into the *cis* chamber of the measurement setup [55]. Voltage was applied and current was measured during translocation experiments. The applied voltage was ranged from 10 mV to 200 mV. All the λ-DNA translocation experiments were performed at room temperature.

3.2.3 Results and Discussion

Solid-state nanopores were drilled in 30 nm thick SiO_2 membrane using FIB. The nanopore fabrication process flow is shown in Figure 3.7.

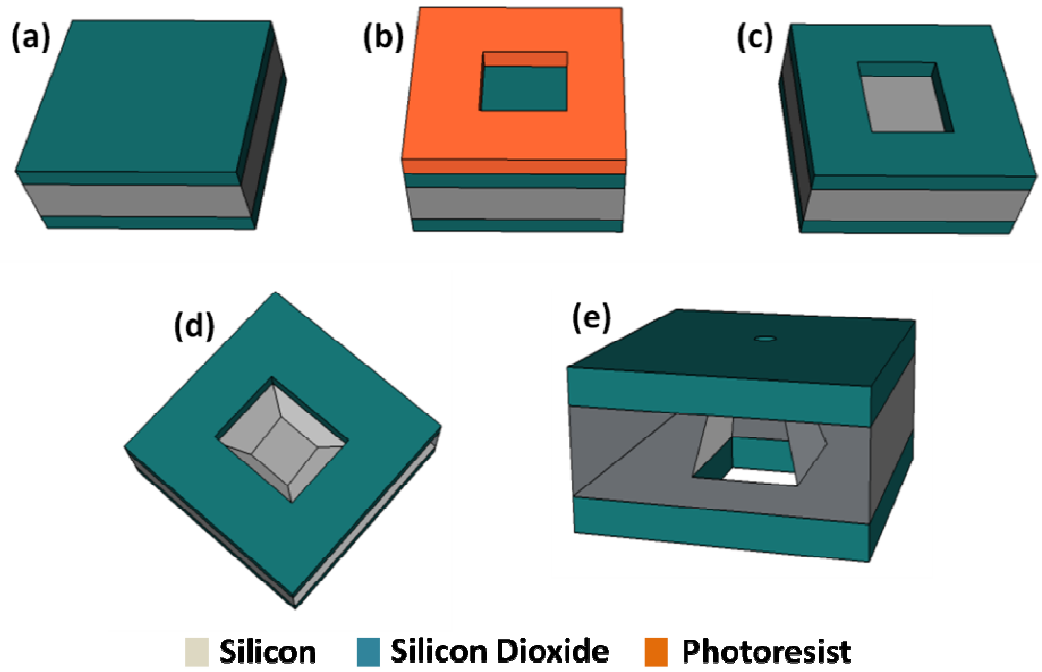

Figure 3.7 Process flow for nanopore fabrication. (a) oxidized Si chip. (b) After photolithography. (c) After BHF wet etching and acetone wash. (d) After TMAH anisotropic etching of Si. (e) Si chip after nanopore drilled with FIB. Reprinted with permission [49]

3.2.3.1 Polymer Deposition and Characterization

Pulsed plasma polymer film (PPPF) was deposited to reduce diameters of the nanopores. The PPPF deposition also provided the carboxylic acid groups on nanopore-wall surfaces. The composition of the polymer films was analyzed using FTIR as shown in Figure 3.8(a). XPS (Figure 3.8(b)) was also used to verify the polymer surface composition. FTIR transmission spectrum of the polymer film showed a very broad absorption band, extending from approximately 3500 to 2800 cm^{-1}. This absorption band can unequivocally be assigned to –COOH groups. The unusual broadness of this absorption band showed the presence of varying extents of H-bonds from the –OH groups of the -COOH functionality [156]. The other absorption bands, centered around 2900, 1700 and 900 cm^{-1}, showed the presence of C-H and C=O vibrational modes as expected for a polyMAA film. High resolution C(1s) XPS spectra of MAA films showed the controllability of the MAA film compositions as a function of the deposition conditions used. XPS analysis was done for polymer films deposited under pulsed and continuous-wave (CW) conditions. XPS spectra for films prepared under CW, as compared to pulsed conditions using 1ms on/5ms off, and 3ms on/30ms off pulse widths as shown in Figure 3.8(b). Peak centered near 289 eV is the high binding energy, which can be uniquely assigned to the carboxylic (COO) group [157]. The amount of the –COOH groups, relative to the total carbon content, increased significantly as the plasma duty cycle is decreased. This controlled variation in the –COOH surface density was quantified by integration of the deconvoluted C(1s) high resolution photoelectron spectra, as shown in Figure 3.8(b). The contribution of the –COOH groups to the total carbon 1s electrons is just 4.0% for CW plasma condition. The –COOH contribution increased to 5.2% and 8% for 1 ms on/5 ms off and 3ms on/30 ms off conditions respectively. It was concluded that higher surface density of –COOH groups is present in the film deposited under pulsed compared to CW conditions. The density of surface groups was found to be increasing as the plasma duty cycle employed is decreased.

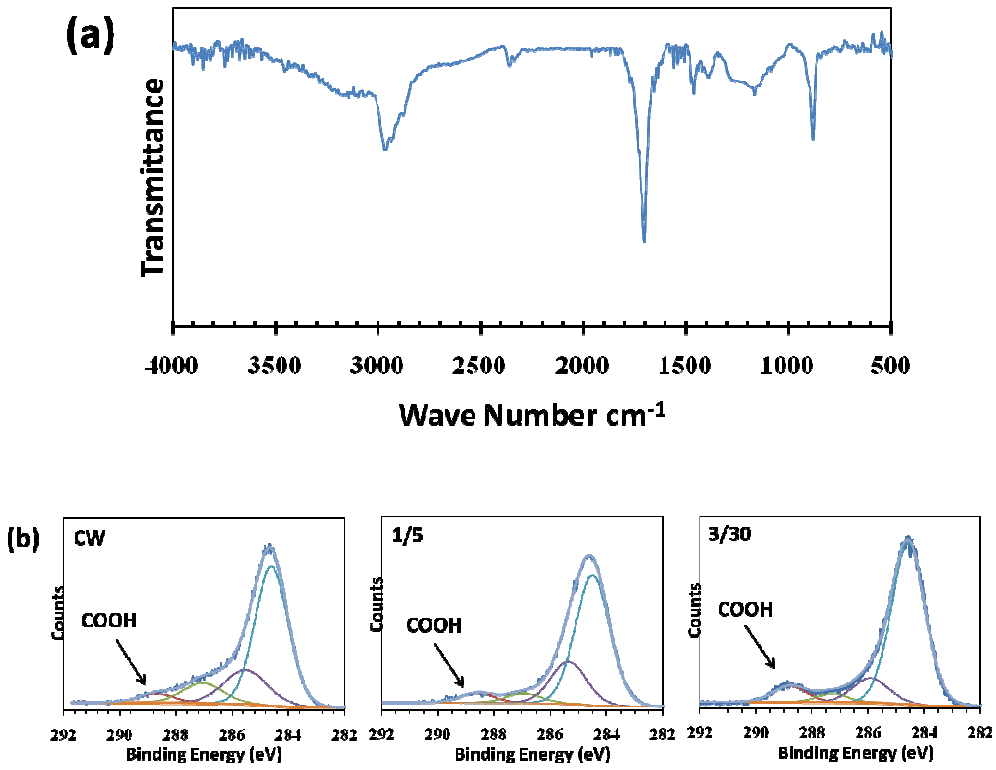

Figure 3.8 (a) FTIR spectrum of plasma polymerized MAA films. The duty cycle during this deposition was 3 ms on and 30 ms off (b) High resolution C(1s) spectra of polymer films obtained from plasma polymerization of MAA under Continuous Wave plasma (CW) and pulsed plasma conditions (on/off pulse plasma ratio of 1/5 and 3/30). Reprinted with permission [49]

3.2.3.2 Characterization of PPPF Deposition Rate

The deposition rate of PPPF was found using profilometer measurements. The process showed linear dependence on time as shown in Figure 3.9. The process showed linearity of the film deposition rate extended over the entire range of thicknesses examined (from 15 to 170 nm). The plasma operating conditions were adjusted for a deposition rate of ~ 8 nm/min. The condition employed for 8 nm/min deposition rate were: 150 W input power, 160 mTorr monomer pressure, and a pulsed plasma duty cycle of 3 ms on time and 30 ms off time. The same plasma conditions were employed during production of the films for the FTIR, XPS (Figure 3.8) and film thickness measurements (Figure 3.9).

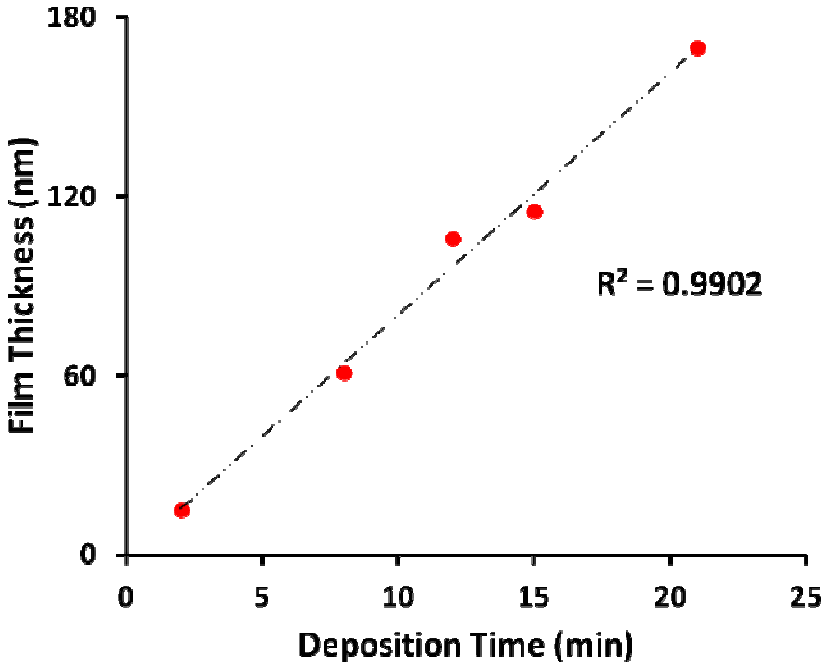

Figure 3.9 Plot shows film thickness control with pulsed plasma deposition. The deposition of the polymer was linear with respect to time. Reprinted with permission [49]

3.2.3.3 Nanopore Shrinking with PPPF Deposition

FIB was used to drill a 320 nm pore that was reduced to 80 nm diameter using PPPF deposition, as shown in Figure 3.10. The nanopore reduction could be clearly verified by the SEM imaging. The SEM images showed diffused boundary of the nanopore due to nonconductive nature of the polyMAA film. We found that the electron beam energy damaged the surface of the PPPF nanopore. The 80 nm nanopore closed during SEM imaging due to surface relaxation of the polymer layer. TEM or FESEM electron beam has been reported to relax the area around periphery of nanopore drilled in oxide membrane. The boundary material relaxation resulted in nanopore shrinking. When nanopore diameter was below 100 nm, the polymer layer closed the nanopore due to reorganization of the polymer film, promoted by the electron beam exposure.

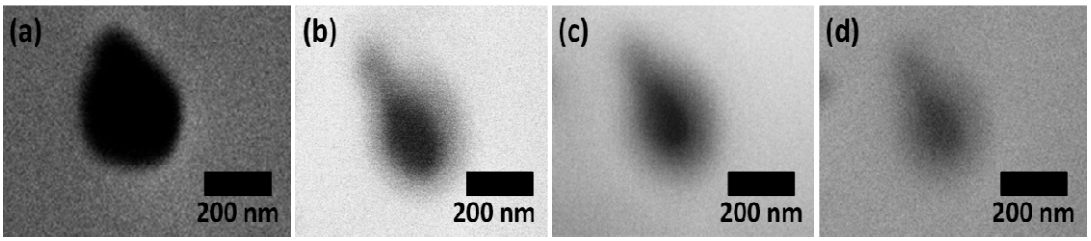

Figure 3.10 (a) The starting nanopore diameter was 320 nm as fabricated with FIB. (b) After 12 minutes PPPF deposition (~160 nm diameter). (c) After 15 minutes PPPF deposition (~120 nm diameter). (d) After 18 minutes PPPF deposition (~80 nm diameter). SEM micrographs became blurry due to nonconductive nature of polymer. Reprinted with permission [49]

To get better images of the nanopore, Atomic Force Microscope (AFM) was used to characterize and measure the plasma polymer deposition shrinkage of the nanopore, as shown in Figure 3.11. AFM micrographs revealed very uniform surface morphology of the nanopore after PPPF deposition. The micrographs in Figure 3.11 showed the excellent control on the nanopore shrinkage using PPPF deposition. A 300 nm nanopore was successfully reduced to 10 nm with PPPF deposition in a sequence of three step reductions of of 8, 13 and 21 minutes. AFM micrograph data revealed that particular plasma process produced a uniform diameter reduction rate of approximately 14 nm min^{-1}. This shrinkage rate is in good agreement with the film deposition rates as shown in Figure 3.9, in that the nanopore shrinkage rate is almost twice of the polymer deposition rate on a flat substrate.

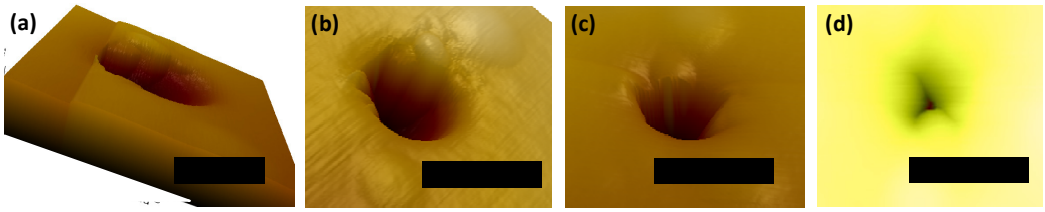

Figure 3.11 (a) AFM micrograph of the nanopore (300 nm) as fabricated with FIB. (b) After 8 minutes of PPPF deposition (~190 nm diameter). (c) After 13 minutes of PPPF deposition (~120 nm diameter). (d) After 21 minutes of PPPF deposition (~10 nm diameter). All scale bars are 200 nm. Reprinted with permission [49]

3.2.3.4 Conductivity Measurements of PPPF Nanopore

Current-voltage *(I-V)* measurements were carried out in ionic solution of 1 M potassium chloride (KCl) to electrically characterize the nanopore shrinkage. The *I-V* measurements were performed after each PPPF deposition step. The electrical data confirmed that the nanopore remained open after each plasma processing step and decrease in conductance was observed with increasing plasma deposition times. Thus these *I-V* measurements are in accord with a reduction in nanopore diameter with increasing polymer film thickness. For each of the nanopores, the current changed linearly with the applied voltage as shown in Figure 3.12.

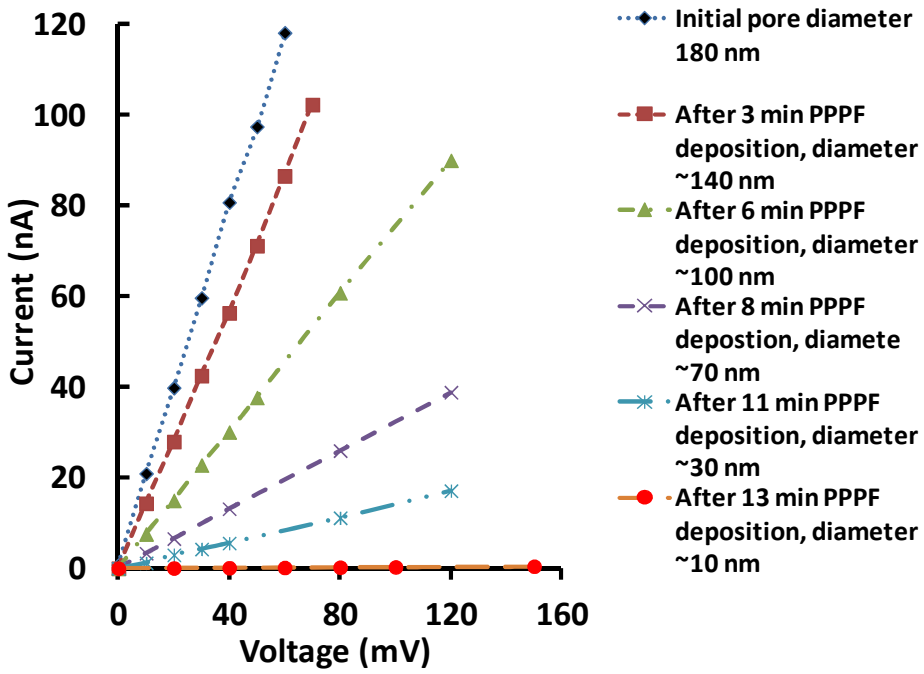

Figure 3.12 Shows the *I-V* current measurements with the PPPF deposition. The initial nanopore diameter was 180 nm. The nanopore diameter was reduced to 140, 100, 70, 30 and 10 nm after 3, 6, 8, 11 and 13 minutes of polymer deposition respectively. Reprinted with permission [49]

Conductance of the nanopore, *G*, was also measured at 1 M KCl concentration. Different models have been proposed to fit *G* of nanopores in previous reports [74, 143]. Bulk charge carriers were expected to dominate the ions flow at 1 M KCl. These models also

neglected surface charge effect at higher salt concentrations. For our conductance model, we considered purely cylindrical nanopore channel [143]. Based on the linear plasma deposition rate, a simple resistance equation, $G = \sigma\pi r^2 / L$, can be used to model the behavior of the nanopore, where σ is the conductivity of KCl solution, L is the channel length and r is the radius of the nanopore. Our data revealed two regions for conductance that can be fit to proposed model, as shown in Figure 3.13. Basically, a non-linear variation in *G* was observed with the sequential change in nanopore diameter. It can be reasonably explained in terms of a non-linear plasma polymer deposition along the nanopore channel length. As the naonpore shrank and the pore diameter to membrane thickness aspect ratio increased, we propose that more localized nanopore surface edge deposition in comparison with that on inside vertical walls may have occurred. The overall nanopore geometry would have been deviated from perfectly cylindrical geometry after few minutes of plasma polymer deposition. The PPPF deposition rate on pore-wall would also vary along the length of the nanopore channel due to reduced diffusion of polymer vapors during the deposition process. Additionally, the upstream volume transport of pre-polymer gaseous species through the nanopore causes reduced pressure. These effects can be accommodated by changing r^2 to $r \times r^*$, where r and r^* are the top and bottom radii of the nanopore respectively [74]. These observations are in accord with gas transport phenomena through porous membranes as reported earlier [158]. This pressure drop across the membrane can be described as an exponential function of time *t*, as shown by the Equation 3.1 [158]:

$$\Delta p(t) \approx p_0 e^{-\in AD_k / V_u l^2 t} \qquad (3.1)$$

Here $\Delta p(t)$ is the pressure drop across the membrane as a function of *t*, p_0 is the pressure drop at time $t = 0$, $\in$ is the porosity of the membrane, *A* is the exposed area of the membrane, D_k is Knudsen diffusivity, V_u is the volume upstream of the membrane, l is the length of the nanopore channel.

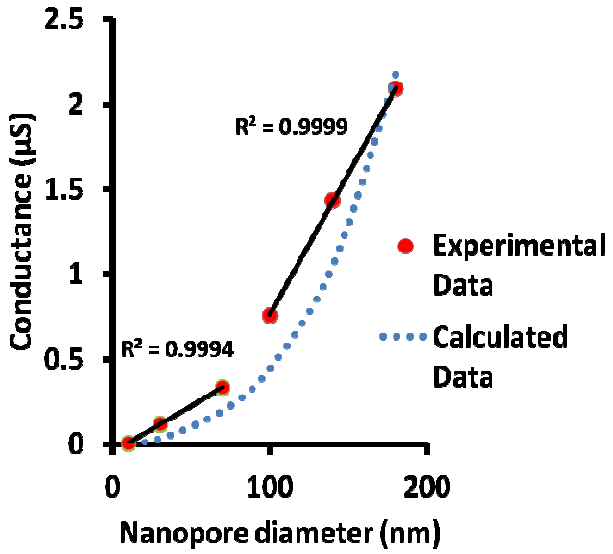

Figure 3.13 Shows the conductance plot for after successive deposition steps of PPPF deposition. The calculations are for 10 mV of applied potential and 1 M KCl concentration (blue dotted line). Measured data (red large dots) shows good fit to the model curve. The plot sows two regions of linear current behavior which was due to the conical geometry of the nanopore. Reprinted with permission [49]

3.2.3.5 Current Behavior of PPPF Nanopore at Different Salt Concentrations

We used 0.1 M and 1 M KCl for *I-V* measurements with a 10 nm PPPF nanopore to examine the current behavior of the nanopore at different salt concentrations as shown in Figure 3.14. The nanopore *I-V* measurements showed linear current behavior. At high KCl concentrations ([KCl] ≥ 100 mM), the conductivity of the nanopore showed linear dependence on KCl concentration as expected for the bulk conductivity of KCl during the voltage sweep [143]. When diameter of the nanopore is comparable to the diameter of the diffusing ionic species (K and Cl ions), the diffusion of the ions would be reduced due to hindered diffusion. This phenomena would reduce the conductivity of the nanopore as compared to bulk conductivity [20, 25]. It was also reported that lesser electrostatic interactions inside nanopores would reversely increase the nanopore conductivity when compared to bulk conductivity of the electrolyte [159]. The deposited MAA polymer film has COO- fixed charges at *pH* 7.0 which would have increased the concentration of K^+ ions inside the channel due to electrical double

layer at the walls of the nanopore [77]. The electrostatic enhancement would have been compensated by the hindered diffusion effect [20]. In PPPF nanopore, conductivities of KCl in nanopore and bulk solution can be considered approximately equal. Conical nanopores in track-etched Poly (ethylene terephthalate) (PET) membranes had been reported to rectify the ionic current due to electrical double layer [160]. PPPF nanopore is also conical but it did not show rectified current behavior. PET membranes are generally very thick (10–12 µm) as compared to our polymer nanopore with membrane thickness of ~200 nm [160]. So the nanochannels fabricated in PET membranes made perfect conical structure of channels. PET channel length is 12 µm while it has 300 nm opening at one side and 5–10 nm opening at other side of the membrane. Our polymer nanopore would not be perfectly conical due to conformal nature of the plasma polymer film and secondly the oxide membrane was very thin. We propose that PPPF nanopore would not rectify the current signal because there would not be significant asymmetry in electrostatic potential along the channel during length [160].

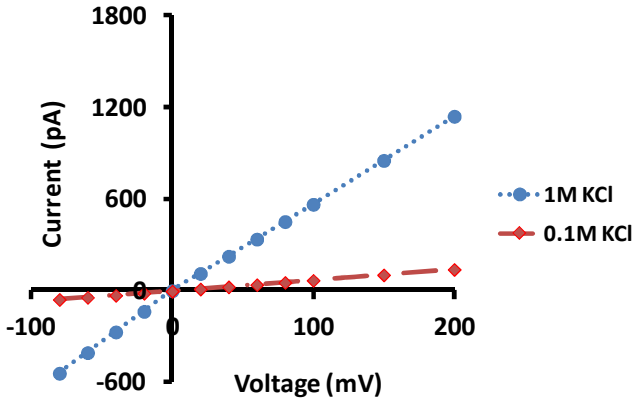

Figure 3.14 Shows *I-V* characterization of 10 nm nanopore at KCl concentrations of 0.1 M (diamonds) and 1 M (circles). The current scaled linearly with the voltage at both of the salt concentrations. Reprinted with permission [49]

PPPF nanopore shrinkage process is described by Figure 3.15. The nanopore diameter and channel length showed linear behavior against time. This plot was based on the

AFM micrographs, the profilometer and ionic measurement data and shows the overall behavior of PPPF deposition process for nanopore shrinking.

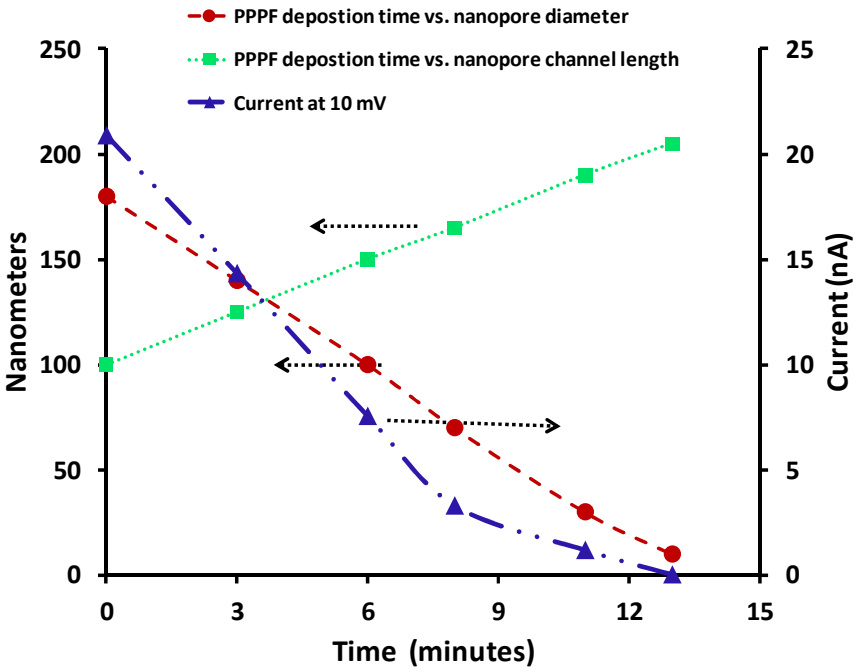

Figure 3.15 The plot shows the nanopore diameter (circles) and channel length (squares) with respect to PPPF deposition time. The starting nanopore diameter and channel length were 180 nm and 100 nm respectively. After approximately 4 minutes of deposition the channel length and diameter became equal in dimension. The measured current (triangles) also scaled almost linearly with the nanopore diameter which again showed uniform deposition rate with time. Reprinted with permission [49]

3.2.3.6 DNA Translocation Experiments

Translocation experiments using DNA were carried out to demonstrate the usage of PPPF nanopore for biosensor applications. We used unmethylated 48.5 kbp double-stranded λ-DNA in 1 M KCl buffered with 10 mM Tris-HCl and 1 mM EDTA solutions at pH 7.5. The diameter of the PPPF nanopore used for DNA translocation experiments was 10 nm. Open pore *I-V* measurements were performed before the introduction of the λ-DNA into the *cis* compartment of the chemical cell as shown by inset of Figure 3.16. The current blockades due

to DNA translocation are shown in Figure 3.16. The current signal was digitized at 200 kHz with a low pass filter cutoff frequency of 10 kHz. The average translocation time for one λ-DNA was approximately 2.2 msec which was in good agreement with earlier reports [143]. After DNA was added into to *cis* compartment of the device, many transient current blockage pulses were observed. Nanopore diameter was also calculated from the magnitude of current blockage pulses using the relation $\Delta I/I_{open} = A_{DNA}/A_{nanopore}$, where ΔI ~ 65 pA was the current blockage magnitude, I_{open} ~ 1240 pA was open nanopore current, A_{DNA} ~ 5 nm^2 is the average cross-sectional area of double strand DNA and $A_{nanopore}$ was the nanopore diameter [65]. The value of $A_{nanopore}$ was calculated to be equal to 95.38 nm^2. Assuming a circular nature of nanopore, the diameter of the nanopore was found to be equal to 11 nm which was in good agreement with nanopore diameter measured with AFM.

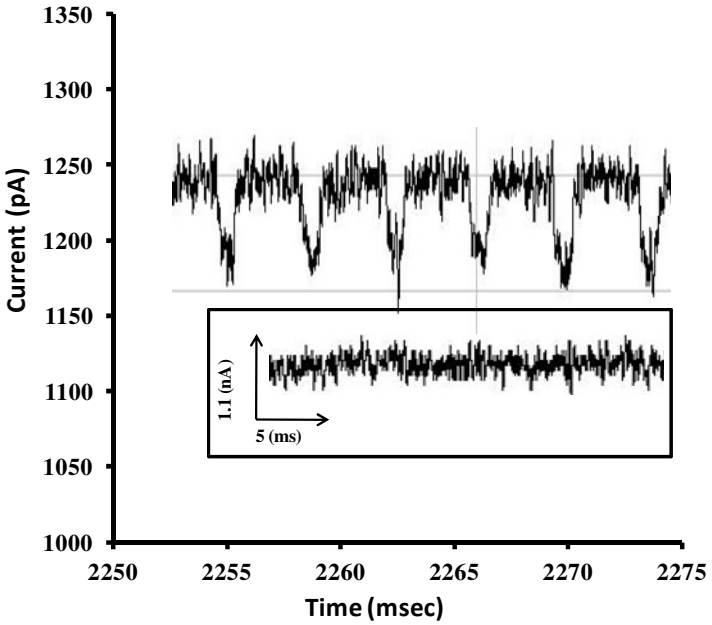

Figure 3.16 Shows DNA translocation through the PPPF nanopore. Current blockades were seen when λ-DNA at was added to the *cis* compartment and 100 mV of applied potential was applied. The inset shows the baseline current before the introduction of λ-DNA. Reprinted with permission [49]

3.2.4 Conclusions

The pulsed plasma polymerization process was employed to reduce nanopore diameters with *is situ* control on surface functional groups. The PPPF nanopore has been demonstrated for use in nanopore sensing applications for the first time. The PPPF nanopore shrinkage process involves only a single step and provides excellent control of the pore diameter. The control of pore shrinkage has been characterized extensively by a variety of conductivity measurements. The viability of this approach for single molecule sensor applications has been demonstrated using double stranded λ-DNA. The reported nanopore shrinking method offers accurate control of both pore diameter as well as molecular tailoring of the surface chemistry of the pores. The surface chemistry can be controlled simply by appropriate choice of monomer and/or by attachment of appropriate molecules to reactive functional groups retained in the nanopore walls.

3.3 Real-time Detection and Analysis of DNA Translocation using Graphical Processing Unit (GPU)

3.3.1 Introduction

Fabrication of solid-state devices at micro- and nano-scales has opened new approaches for exploring and analyzing diseases. Processes like mass spectrometry (MS), Multi-Electrode Array (MEA), and Magnetic Resonant Imaging (MRI) generates lots of data. Advances in technology increases the amount of data generated per unit time from such kind of processes, and making it harder for the analyst to inference results from it quickly, as the manual process is time consuming, tedious, and error-prone. Data generated by Nanopore when DNA is passed through it is similar kind of process generating millions of data even a single Desktop cannot handle it [55]. Moreover, the data flood collected is too noisy due to background noise (small weak peaks) and time-varying baseline (baseline artifacts). It is very common that the peaks constitute very small percentage of the acquired data. The process of finding peaks in such

huge data is done off-line manually, which is tedious, time-consuming and error-prone. To this point, the data deluge created by such measurements already precludes traditional architectures. A solution seems to combining parallelism with specialization. Multi-core architectures coupled with accelerators are becoming common to sustain high performance equivalent to a supercomputer-class node as a cheaper solution. Commodity processors provide solution for compute-intensive problems within reasonable budget. Commoditization is common place for asymmetric processors and systems like NVIDIA GPUs [161, 162]. Thus it is natural that commoditization of accelerators will enable their use in analyzing large-scale data at a fraction of a budget of comparable traditional machines. NVIDIA GPUs has been used for feature detection in large amount of proteins data [163], and fast mining of huge spike trains generated from Multi-electrode Array (MEA) [164]. Work has been done to show overall performance improvement by coupling advanced I/O techniques with accelerator based GPU processing [165, 166].

To automate the process we need to device advance I/O techniques for data acquisition and peak detection algorithms that will automatically detect the peaks in the acquired data, and will deliver it to the user in the required format (scatter plots) within seconds. During the detection process the value of threshold is of practical importance, which is used to detect the peaks (below threshold) or the noise (above threshold). Different values of threshold give different signal to noise ratios, i.e., different number of peaks with different widths in our case. Keeping threshold closer to baseline yields many peaks accompanied by weak peaks (peaks with shorter widths that are not real peaks but noise). On the other hand, keeping threshold farther below the baseline can only detect peaks with large amplitudes and ignore peaks with small amplitudes. For the time-varying baseline (baseline artifact), trying different levels of threshold even does not work and a dynamic threshold detection mechanism is required that should keep track of the time-varying baseline. For analyzing similar kind of data (e.g., neural

action potential data), there are a number of techniques developed e.g., feature analysis, cluster analysis, spike shape interpolation and filter-based approaches [167].

To tackle the problem of peak detection in the data generated by nanopore when DNA is passed through it, current implementations have many shortcomings: (i) Currently the process of peak detection is done manually which is laborious and time-consuming, (ii) Data generated is huge (millions of points) acquired in few seconds. To accomplish our first objective we need to automate the process of peak detection by devising algorithm which can extract peaks with its attributes (width, amplitude) and discarding rest of the data. The algorithms need to cleverly choose appropriate threshold for the detection of peaks. Threshold should not be too high (very close to baseline) such that it also detects weak peaks (false positives) neither it should be too low such that it ignores the real peaks (false negatives). Such threshold (static) can only help when the baseline is pretty stable and not time-varying. For time-varying baseline we need baseline tracking threshold that keeps track of the threshold during peak detection.

The automation process can be accelerated by using CUDA programmable NVIDIA GPU (highly parallel architecture) that has been extensively used recently for compute intensive workloads. Our data processing algorithm can benefit from GPU and realize our second challenge to overcome slow I/O by using optimized I/O techniques such as pre-fetching and multiple buffering to break the I/O bottleneck for massive data rates. Advanced I/O techniques coupled with accelerator based GPU processing enables us to develop a fully streamed system, which will increase the overall system performance. Such an approach seems to be the solution to our real-time peak detection framework which will result in high-speed real-time computing. Specifically, our contributions to this work are as follows:

Use of advanced I/O techniques (double buffering and asynchronous I/O) for reading raw data into the system. In our implementation, we overlap I/O with computation; this increases system performance by making the two processes (I/O and computation) to run in parallel. We implemented double buffering for raw data acquisition into the system, while enabling

asynchronous I/O communication between CPU and GPU. Our systems is fully streamed such that raw data is streamed into the system, which after pre-processing at CPU is further streamed it into the GPU, where peaks are detected and analyzed.

Designed and implemented three different peak detection algorithms using one static and two dynamic threshold techniques including baseline tracker method and moving average technique. Static threshold does not change throughout the detection process as opposed to the baseline tracker method in which threshold keeps track of the baseline. Each algorithm detects peaks in the raw input data with their start, end and global minimum (the least current value in nano-amperes in the detected peak).

Parallel implementation of our algorithms for CUDA programmable NVIDIA GPU device. After the required pre-processing of raw data; formatted data is staged into the GPU, which launches kernel (parallel algorithm) for detecting peaks in the data, and copies results back to CPU in streaming fashion. After essential post-processing of results plots are drawn for peak visualization.

Accurate understanding of current blockage pulses plays very critical rule for analysis of target biological species. Different hypothesis are made based on the pulse shape and width. Pulse width relates the molecule length while pulse shape relates its orientation and diameter [33, 61]. The electrical data is acquired by using Axon 200B amplifier connected to Digidata 1440 (Axon Instruments). PClamp 10.2 is used as software for data acquisition. Other data acquisition cards are also used for storing the electrical data from the hardware [55]. The data is stored in .abf (axon binary format) which is further analyzed using Clampfit software. The current sampling time should be in few µsecs so that the electrical measurement setup can record single translocation events. It stores ~ 200,000 – 500,000 distinct values per second. The baseline current is the steady state current when there is not translocation event occurring and is directly proportional to pore size. As we are dealing with devices at micro and nano scale, the current magnitude would also be ranging from µA to nA. At such a small scale, all the

measurement systems are prone to noise from external environment. The inbuilt noise in data can drastically affect the capabilities of device as single molecule biosensor. The noise suppresses pulses of smaller magnitude and we can lose a lot of significant information. Secondly, the manual analysis of all the data points is very time consuming process and is prone to human errors. Thirdly we can never predict the outcome before the whole process analysis is completed. Therefore there is a need for computer-based automated system which can process the data in real-time, reduce the inbuilt noise and recover all the useful information automatically. Here we report a data acquisition platform which can do all in one run. Our proposed method can recover all the useful information from the noisy data and is very time efficient as compared with manual data analysis.

3.3.2 Problem Statement

When DNA is passed through the nanopore, it gives current blockage signals. The electrical measurement setup (sensors) meant for this purpose generates millions points of data. The amount of data per second is enormous for desktop machines (even servers) to handle for real-time analysis. This huge amount of data is analyzed manually by humans for the detection of pulses. The process is tedious and error-prone.

The free versions of pClamp and Axopatch don't have all the features available. Even the full versions of the software's don't have the real-time analysis capability. Our goal is to analyze the data on fly and find pulses (real-time data acquisition for DNA translocation), by recording the blockage data (pulse-width, pulse-magnitude) only, and discarding the rest of the data (noise). We define pulse when the baseline falls below certain threshold of the baseline current, and gets back to the baseline current.

There exists very small percentage of useful information (peaks) in the measured data generated by electrical measurement setup. To address this "Needle in a Haystack problem" we want to process it in real-time. Real-time implementation will decrease the response time for the output (detected peaks) and will make the system faster.

3.3.3 GPU Architecture

GPUs are meant for computationally-intensive data-parallel applications. Its underlying architecture is highly parallel, works in a SIMD (Single Instruction Multiple Data) fashion. GPU is a many-core device in which cores are grouped together in the form of Symmetric Multiprocessor (SM). A single GPU has couple of SMs. For Instance, NVIDIA GPU 9600M GT has 4 SMs, each with 32 cores in it (total of 128 cores), all clocked at GHz. To program GPU, CUDA (Compute Unified Development Architecture) is used which is an extension to C language.

And hence CUDA makes the GPU programming easy. While making our data-parallel application to run on a GPU, we identify hot-spots (parallel portions of the program amenable to GPU architecture) in our application and schedule only those parts to execute on GPU. Such parts of the program are enclosed in function with global_primitive, called kernel. A High-level overview of a GPU application is shown in Figure 3.17.

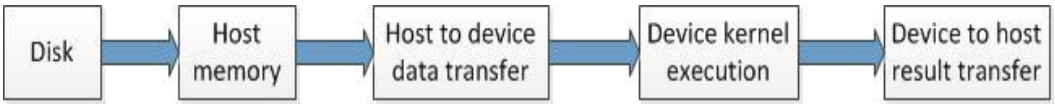

Figure 3.17 Overview of GPU application showing data copying from host to GPU memory, launching GPU kernel, and copying results back to the CPU memory. Reprinted by permission from Elsevier [168]

Main program starts execution on CPU, before launching the kernel, data is transferred to the GPU memory from CPU memory, GPU kernel is launched, and results are copied back to CPU memory. The data-transfer can be done with asynchronous I/O to overlap communication with the computation. Kernel can be launched with thousands to millions of threads using CUDA. Threads-organization follows a 2-level hierarchy; BLOCK-LEVEL and GRID-LEVEL as shown in Figure 3.18. Threads are organized into BLOCKS, which are further organized into

GRIDS. In our GPU architecture one block can support a maximum of 512 threads and a minimum of 32 threads. A grid can hold a maximum of 64K * 64K threads-blocks. While running kernel on GPU, threads are scheduled on each SM in the form of warps. Each warp consists of 32 threads.

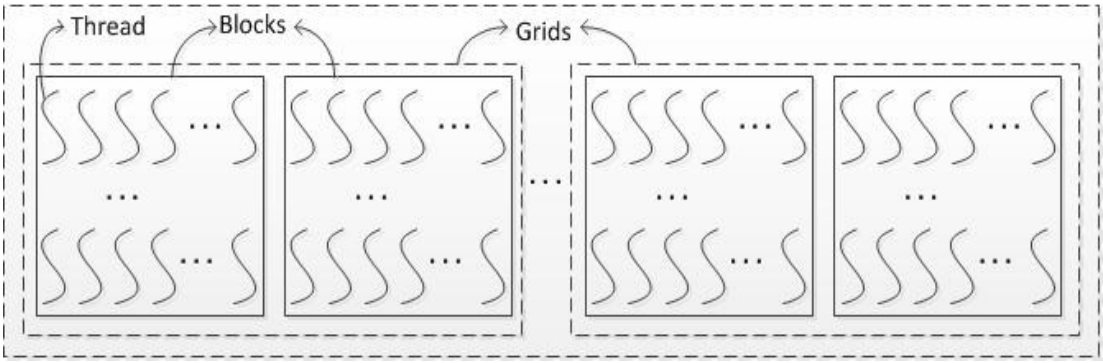

Figure 3.18 Shows the thread organization of the GPU. Threads are organized into blocks, while blocks are organized into grids. Reprinted by permission from Elsevier [168]

GPU has its own memory hierarchy, ranging from high-latency global/device memory to fastest registers available per thread-block. Texture memory, shared memory, and constant memory is part of the memory hierarchy of the GPUs as shown in Figure 3.19. Here we discuss only global memory, shared memory and registers. Global memory is the memory used to transfer data between CPU and GPU. Shared memory is shared among the threads of a block. All threads within a block are synchronized. Synchronization across different blocks is achieved using global memory and needs separate kernel launches. Each thread block has its own set of dedicated registers (16K in our case) which it can use for executing the assigned kernel efficiently. Special care should be taken when handling the branch statements in the GPU code. Branch-divergence within threads of a block causes threads to execute serially and hence hampers the performance.

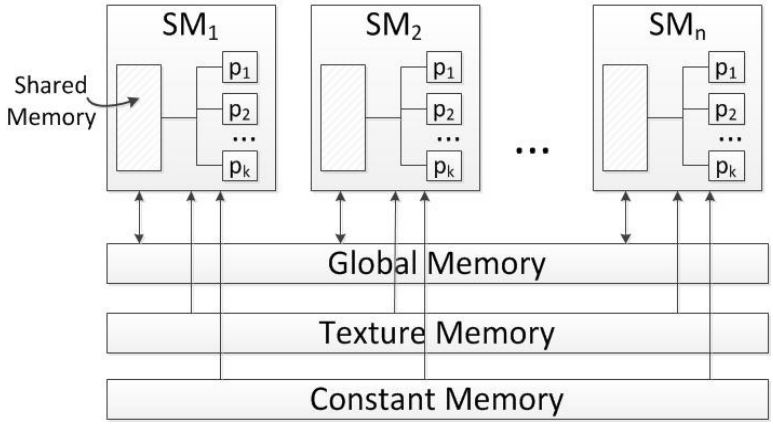

Figure 3.19 Shows the memory hierarchy of NVIDIA GPU. Reprinted by permission from Elsevier [168]

3.3.4 Why GPU for our Problem?

Our problem of finding pulses in huge data accumulated from DNA can be fit into the parallel programming model of GPU. We can better leverage our problem on GPU by breaking down our problem into chunks, and process those chunks concurrently for finding pulses. We expect huge performance benefits from GPUs for implementing such embarrassingly parallel problems. To accomplish I/O challenges which makes the data acquisition process slow, we are using advanced I/O techniques like pre-fetching and double buffering. These techniques significantly reduce the data acquisition time. For efficiently processing this data for peak detection, we implement our algorithm on massively parallel GPU architecture. As elaborated in the evaluation, this system design has huge impact on the overall system performance.

To achieve our objectives, we have designed our system that incorporates the above mentioned high performance techniques. Our proposed techniques for data analysis are fixed and dynamic threshold methods. Dynamic threshold techniques include baseline-tracker method, and moving average method.

3.3.5 Design Challenges

We present the design of our system in this section. We give a high-level overview of the system and highlight different design challenges in realizing real-time peak detection for nanoscale devices. We also present the details of implemented algorithms, and how we have used CUDA-enabled GPUs in parallelizing of these algorithms. We present details of the implemented algorithms and describe the parallelization of the developed algorithms on CUDA-enabled GPUs. Fig 3.20 shows the control flow of using a GPU device to accelerate the automated pulse detection process for nanopores.

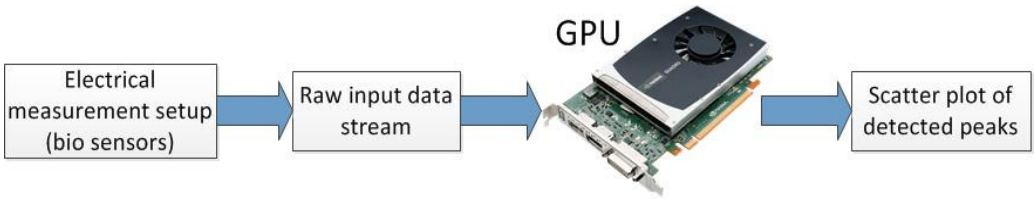

Figure 3.20 Shows flow diagram of GPU-enabled pulse detection in the data flood created by biosensors when DNA is translocated through the solid-state nanopore. The resulting scatter plot is used for decision making regarding presence of specific genes and biomarkers. Reprinted by permission from Elsevier [168]

The system design challenges are categorized into performance challenges and automation (algorithmic) challenges.

3.3.5.1 Performance Challenges

In the acquisition of huge amount of data, I/O and multi-core processing speed are the two bottlenecks in existing systems. Moreover, the I/O and processing speed themselves are sequential in nature. First I/O grabs the data, and then it is processed by the processor. I/O and computation occurs in sequence. Overlapping I/O with computation can improve the system performance. To optimize the I/O we use advanced I/O techniques like pre-fetching and double buffering which overlap I/O with the computation. This improves the system's performance.

Another optimization is to use GPU for parallel processing the tasks. This can process data at much higher speed with its highly parallel architecture. Moreover, for efficient processing

of the streaming data we convert floating point numbers to integers. Integer processing is not only memory efficient (occupies lesser memory) but also make the processing faster (addition, multiplication etc is faster) as compared to the floating point computations. With such a design we achieve a sampling rate of 2.5 million samples per second (~400 nsec per sample), as compared to the original rate of electrical measurement setup which is 454 Kilo samples per second (~2.2 µsec interval between samples). While an improvement of 7.5x observed in comparison to its naïve CPU implementation with non-optimized I/O, which is 333 Kilo samples per second (~3.0 µsec per sample).

3.3.5.2 Automation (Algorithmic) Challenges

There are challenges to run our application in parallel on GPUs. First the data itself is not parallel. Data consists of independent and dependent data points. Dependent data points are those that form peaks though in some cases noise. Independent data points are the rest of the data. There are variable size sequences of dependent data points (e.g., consecutive pulses in a peak); some of them form peaks while others larger than certain width (wide contiguous regions) in µsec (burst) does not form a peak rather noise. Similarly, peaks with too smaller length are also considered as noise. To detect only peaks we define a window which only accepts sequence of pulses that form peaks and not noise.

With GPUs we can launch thousands to billions number of threads. Due to hybrid nature of data (independent and dependent points as well) we only go up to launching thousands number of threads. Increasing beyond 16K threads, the number of peaks detected is reduced. The reason is that peaks falling at the boundary of data-chunks assigned to each thread are not tracked.

3.3.6 System Overview

System is designed into different software modules to distribute the functionality among the components. Figure 3.21 shows a high-level overview of our system. The first component

called Data Pre-fetcher streams (double buffering) raw data in to the system, the Host (CPU). Data-formatter gets data from Data Pre-fetcher and converts the streamed data to proper format to be used by computation Device (GPU), and pass it over to the GPU-Manager, where GPU-Manager off-loads the buffered data into chunks to the device memory using asynchronous I/O, launches GPU kernel for every chunk (for the detection of peaks), and finally copies the result back to the system asynchronously. The three steps copying to GPU, kernel launch, copying results back to the CPU, overlaps data transfer with computation. Results accumulated at the Host are merged together and consolidated to construct the final result. The Result-Analyzer collects data from the Device, extracts the right format (width and Amplitude of the peak), and finally delivers it to the user in form of scatter plots for further analysis.

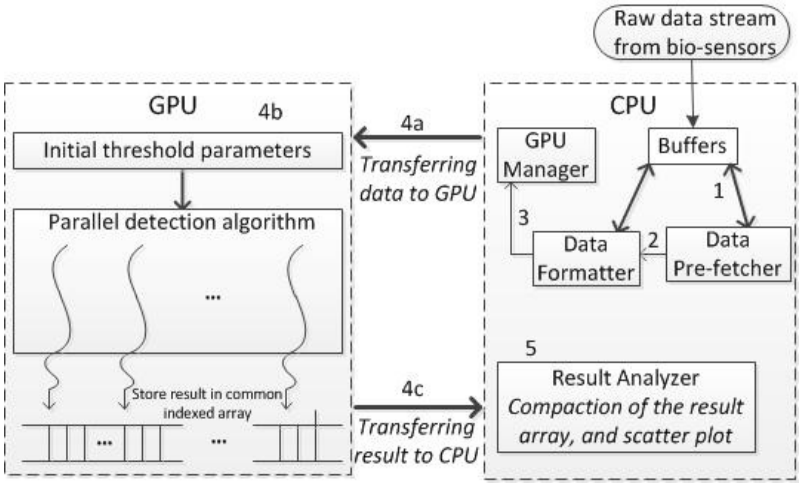

Figure 3.21 Shows high-level overview of the software components of our system. Reprinted by permission from Elsevier [168]

3.3.7 Pulse Detection Algorithms

The purpose of our system is to detect peaks in the given data source. Peaks can be one pulse, or a consecutive sequence of pulses. The application reads values from the data file, process those values, and detect them against a threshold selected according to a given criterion. Different approaches are used for the selection of threshold; fixed threshold and dynamic threshold. Dynamic threshold is further categorized with an ad-hoc technique called

baseline tracker method and other is a well-known statistical technique rolling average method. The data source contains current values in Nano-Amperes (nA) collected from the DNA translocations through nanopore. The sampling time is 2.2 microseconds. The application read the data through streams from the file where I/O is much slower as compared to the processing power. To hide the I/O latency data is pre-fetched in chunks. Using an I/O optimization technique double buffering, data is read at faster speed, and is allocated to a larger buffer, from where it is then copied to the GPU. For faster copying of the data, we used page-locked (pinned) memory. The input data is divided in equal-size chunks and assigned to the number of threads in the GPU kernel launch. Each thread runs a copy of detection algorithm. The peaks detected within the chunk are accumulated in the result memory. The output per thread is variable due to the random distribution of peaks in the data acquisition process. The result (metadata) is copied back to the host for further analysis. On CPU, compaction operation removes unnecessary zeros from the metadata leaving only (start, minimum, end) of detected peaks. From this metadata we extract the (width, minimum) of the peak. This result is displayed as scatter plot showing relationship between the width and minimum of the peaks. The data layout algorithm (Figure 3.22) is same for all three techniques, which converts floating-point data to the integers.

Input: File of raw data including time and current information

Output: File of time column (t_{value} array) and current column (I_{value} array) as integers

while not EOF **do**

Scale all t_{value} to µseconds and convert to integers

Scale all I_{value} to nanoamperes and convert to integers

Write t_{value} and I_{value} output to file

end while

Figure 3.22 Shows the date preparation algorithm. Reprinted by permission from Elsevier [168]

Figures 3.23 and 3.24 show the general flowcharts of the three detection algorithms. The algorithms differ from each other in the selection criterion of threshold whether its static or dynamic. Dynamic algorithms further differ in the adapting nature of threshold, during the process of detection. This adapting attitude of the threshold is shown with optional tag in the Figure 3.23.

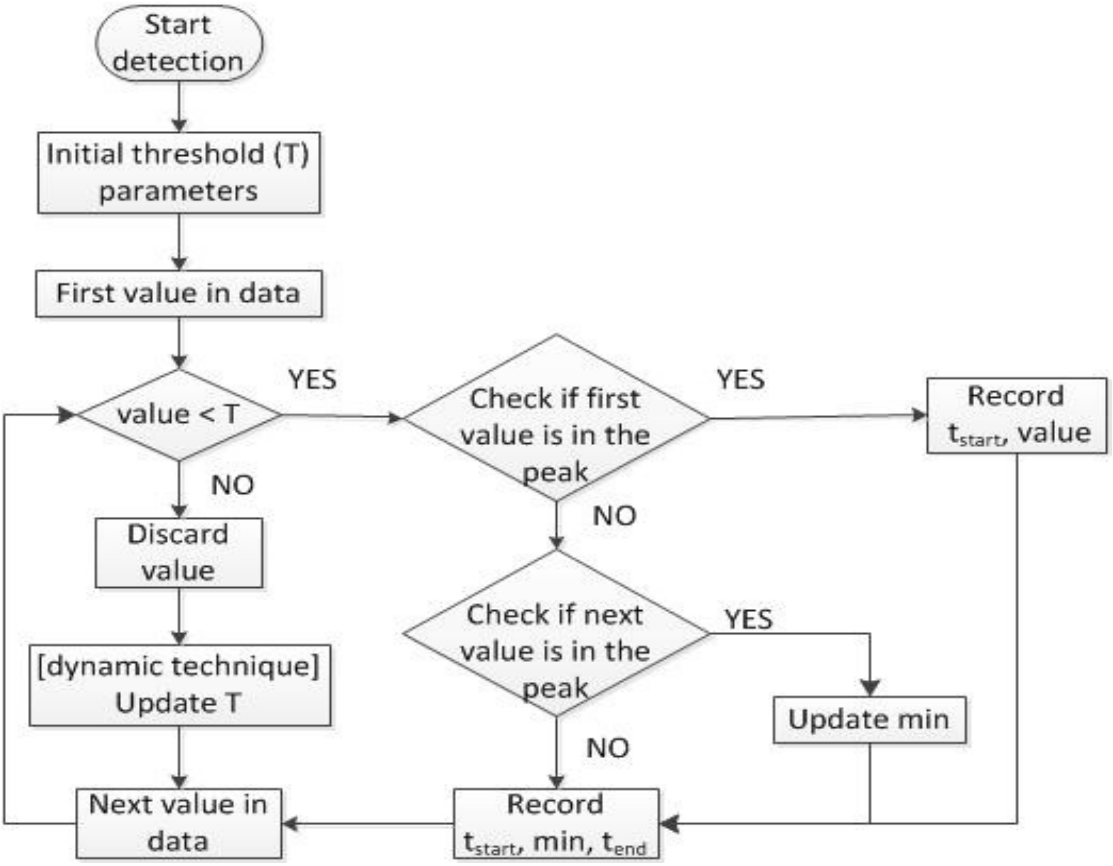

Figure 3.23 Shows the flow chart for pulse detection algorithm(s). Reprinted by permission from Elsevier [168]

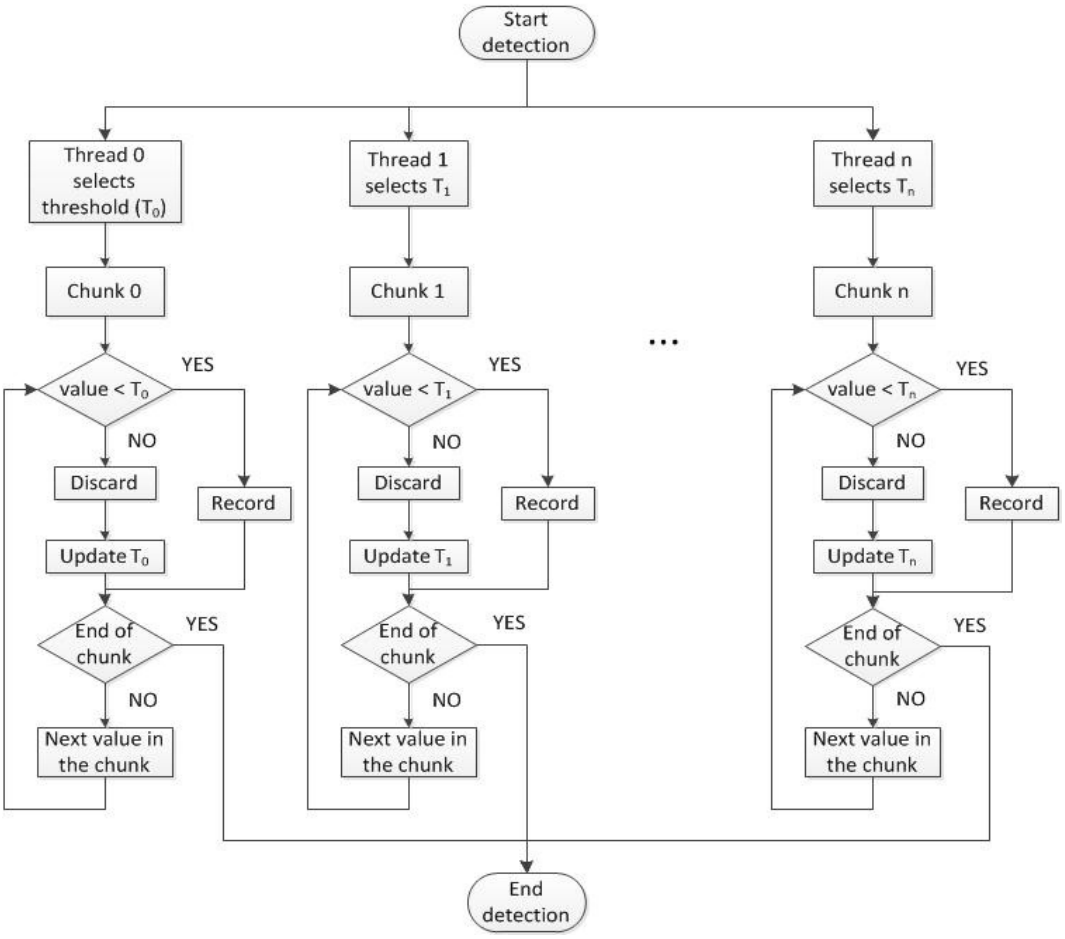

Figure 3.24 Shows parallel version of detection algorithms: Each thread calculates the initial threshold, and detects peaks in its chunk. Reprinted by permission from Elsevier [168]

3.3.7.1 Fixed Threshold Technique

We first describe the processing of peaks using fixed threshold. The Figure 3.25 shown below processes values in sequence from the DNA file and compares against a given threshold. Threshold is selected at the beginning of the detection process with some difference (nano-amperes) less than baseline. This threshold remains static throughout its detection process. All the data points which are current values are tested against this static threshold. If the current value is less than threshold, it is recorded, otherwise discarded. The peak detected can just be a single pulse, or it can be a series of pulses. In our application we are concerned about series of pulses, forming a peak. Peaks with very smaller duration (equal to one or two sampling

periods), or with very large duration (more than hundreds of sampling periods) are considered as noise. For this purpose to detect the right peaks, we define a window which defines the desired width of the peak. When a pulse is detected, its start time, and corresponding current value is recorded. The current value of the next pulse (if detected for this peak) is compared to the previous pulse, and the minimum current between them is selected. The process is repeated for the next consecutive pulses (if detected for this peak), until a value greater than threshold is encountered. At this point the end time of the peak detected is recorded. So now we have start time, end time and minimum current of the peak. We also take care of the width of the peak while detecting it. If the width of the peak exceeds certain width, it is discarded. In this way, all the values in the file are processed, the peaks with its given attributes are detected, and recorded. We can also calculate the width of the peak from the start-time, and end-time of the peak. We detect the peaks using a window with minimum width and maximum width, and its depth is the difference between the baseline and the given threshold. Peak detected within the given width and threshold (depth) of the window is accepted, while others are discarded. Peaks are detected precisely, and results from the automated approach have been verified with human-based decisions about peaks.

It is the simplest approach we designed. This approach is faster but error prone to the detection process. It may ignore the valid peaks or detected incomplete peaks with incorrect width and minimum, which results in noisy peaks. This happens in regions where baseline magnitude is fluctuating between just above and just below threshold. Adaptive (dynamic) threshold technique is one of the ways for solving this problem. Instead of choosing a single Threshold at the beginning, Threshold is updated at each signal (current) value, and when a peak detected is in progress, we lock the Threshold updating phase. Such techniques show better improvement over noise removal in peak detection process.

Input: File of time column (t_{value} array) and current column (I_{value} array) as integers
Output: Recorded pulse (P) as: $P_{[start, min, end]}$
Select threshold "T" with a desired difference "x" below the first value in baseline
for all I_{value} in I_{value} array **do**
    I_{value} <> T
    if I_{value} < T
        Record t_{value} as P_{start}
        Update P_{min}
        if $P_{[end-start]}$ > max_width
            Discard this pulse and jump to the next value
        end if
        Update P_{end}
    else
        if $P_{[end-start]}$ < min_width
            Discard this pulse and jump to the next value
        end if
        if P_{width} is within defined time-frame
            Write output $P_{[start,min,end]}$ to file
        end if
        Discard I_{value}
    end if
end for

Figure 3.25 Shows algorithm for fixed threshold technique. Reprinted by permission from Elsevier [168]

3.3.7.2 Dynamic Threshold (Baseline Tracker technique)

In this case, we have adaptive threshold, which keeps track of the baseline, with certain distance x (nano-amperes) below baseline values, and detects peaks accordingly. The algorithm for dynamic threshold is shown in Figure 3.26. We start with a seed value of threshold which is less than the first current value with *x*, we track this threshold in accordance with the baseline as we move forward. Peak is actually the part of baseline, and it starts with the data points that go down abruptly. If *x* is too high, this will detect only peaks with amplitude larger than *x*, and will discard peaks with amplitude less than *x*. Keeping *x* too small, is also not favorable; this will detect peaks with too low amplitude which we do not consider as peaks though. This *x* should be selected some reasonable value such that it detects peaks and not noise. In our experiments we tested data with varying values of *x*; 1000 nA, 1200 nA, and 1500

nA, etc. We found 1200 nA, the best out of those values. The threshold is updated at each value of the baseline except for the duration of peak detection process. It will be clearer with the following example. For instance, for a data sequence of *a, b, c, d, e, f, g,* and *T* is the threshold; let's say {*c, d, e, f*} < *T*, and {*a, b, f*}> *T*. For point *a* > *T*, *T* is maintained as, *T* = *a* – *x*; where *x* is a defined distance at which *T* is kept below baseline for each data point. We repeat the process for point *b* > *T*. As soon as *c* is encountered i.e., *c* < *T*, process of peak detection starts, and the *T* updating process is locked. *c* is recorded as t_{start}. For subsequent value *d* < *T*, minimum out of *c* and *d* is calculated, say *min1* and buffered. For next value *e* < *T*, minimum out of *min1* and *e* is computed and stored, say *min2*. Same process repeats for value *f* and the minimum is recorded. To this point we have minimum of the detected points so far, say min. For the next value *g* > *T*, we output the recorded [t_{start}, *min* and t_{end}] with the scaled minimum value (*min* = *min* – *b**(the point right before start of peak), and unlocks the updating process, which is *T* = *g* – *x* and so on. The method again starts tracking baseline by keeping the threshold at a fixed distance below baseline values. In case of dynamic threshold, the peak detection completes based upon two scenarios. Firstly, as soon as the baseline values goes up against threshold. Secondly, if the baseline becomes a peak and it stays below threshold for time greater than the defined time-frame of the window, such that the width of the peak becomes greater than the width of the window, such a peak is discarded. In this way, all the peaks that qualify the window (the width) and with values less than *T* are detected, while the rest data points which are not peaks or the peaks doesn't lie in the window are discarded.

Input: File of time column (t_{value} array) and current column (I_{value} array) as integers
Output: Recorded pulse (P) as: $P_{[start, min, end]}$
Select seed value of threshold "T" with some difference "x" below baseline
for all I_{value} in I_{value} array **do**
    I_{value} <> T
    if I_{value} < T
        Record t_{value} as P_{start}
        Update P_{min}
        if $P_{[end-start]}$ > max_width
            Discard this pulse,
            Update T (T = I_{value} – x) and jump to the next value
        end if
        Update P_{end}
    else
        if $P_{[end-start]}$ < min_width
            Discard this pulse and jump to the next value
        end if
        if P_{width} is within defined time-frame
            Write output $P_{[start,min,end]}$ to file
        end if
        Discard I_{value}
        T = I_{value} – x
    end if
end for

Figure 3.26 Shows the algorithm for baseline tracker technique. Reprinted by permission from Elsevier [168]

3.3.7.3 Dynamic Threshold (Rolling Average technique)

Rolling average or moving average technique is another kind of dynamic threshold technique that we adapted for our peak detection process. First we explain how rolling average technique works, and then we will show how we applied this to our problem.

In statistics world, it's known as moving average, rolling mean, or running average. It is a type of finite impulse response filter used to analyze a set of data points by creating a consecutive series of averages over different subsets of the overall data set. Subset size is also called window of the moving average filter. So moving average is not a single number but it is a

set of numbers, each of which is the average of the corresponding window of a larger set of data points.

To calculate the threshold (*T*) using moving average method, we calculate average of values in a window of size "*w*" as given below: *w* is the number of items in the window.

sum = 0;

tolerance = *x*%;

for all I_{value} in window-Array do

$sum = sum + I_{value}$

end for

average = *sum/w*

T = *average* – *average* * *tolerance*

Further we compute tolerance *x*% of this calculated average, which is then subtracted from the average to get the Threshold (*T*) .i.e., *T* = *average* – *average* * *tolerance*. For efficient processing, algorithm does not load window with fresh points all the time.

For the rest of the data points that do not form peaks but are rather part of baseline, we only update *T* using moving average technique. For efficient processing, we don't re-compute the sum for every new data point. We only slide the window over the next point to include it and discard the first value in the window and then compute *T* over those points. as given below:

$new\_sum = old\_sum + I_{value}[index] - I_{value}[index - w]$

average = *sum* / *w*

T = *average* – (*average* * *x*%)

Here index is for an individual iteration i.e., for each signal value, *w* is the size of window and *x*% is the tolerance. We tested our threshold with varying window size, and tolerance. Keeping *w* too small (5, 10 etc), the algorithm runs faster but the quality of peaks is degraded. Keeping *w* too large e.g., 1000 runs slower but with better quality of peaks. We trade-off between the speed and quality of peaks with window size of 200 and tolerance of 2.8%. A

tolerance of 2.8% means that for average value of 58000 nA calculated over 200 points, *T* should be 1624 nA below this value. The rest of peak detection process is same as that of Figure 3.26, i.e, updating *T* is enabled when no peaks is encountered otherwise it is disabled when peak is in the process of detection. The algo for rolling average is shown in Figure 3.27.

Input: File of time column (t_{value} array) and current column (I_{value} array) as integers
Output: Recorded pulse (P) as: $P_{[start, min, end]}$
Calculate seed threshold "T" over initial window size "w" with defined tolerance x%"
sum = 0;
tolerance = x%;
for all I_{value} in window-array do
    sum = sum + I_{value}
end for
average = sum/w
T = average – average * tolerance
for all I_{value} in I_{value} array **do**
    I_{value} <> T
    if I_{value} < T
        Record t_{value} as P_{start}
        Update P_{min}
        if $P_{[end-start]}$ > max_width
            Discard this pulse,
            Refill the window with next *w* items and compute T
            Jump to the next value
        end if
        Update P_{end}
    else
        if $P_{[end-start]}$ < min_width
            Discard this pulse and jump to the next value
        end if
        if P_{width} is within defined time-frame
            Write output $P_{[start,min,end]}$ to file
        end if
        Discard I_{value}
        Move forward the window to include next item, and discard first item in the window. Re-compute the T over the window now
    end if
end for

Figure 3.27 Shows algorithm for rolling average technique. Reprinted by permission from Elsevier [168]

3.3.8 Detailed Architecture

In the following sections, we describe the major software components of our system.

3.3.8.1 Data Pre-fetcher

To accomplish the I/O challenge in our system, which makes the data input process much slower than the data processing; this component pre-fetches the data at higher speed needed for processing. Pre-fetcher uses advanced I/O technique, double buffering to overlap I/O with computation; this will increase the overall throughput (samples per second) of the system. In double buffering technique we are using two buffers as shown in Figure 3.21, one for processing the data and other for reading the data from file. When the second buffer is processed by the processing thread (locked by processing thread), meanwhile first buffer (locked by reader thread) is read by the reader thread, (step 1). As soon as reader is done with reading data into its buffer, it swaps its buffer with the other (if available) being processed (step 2). Now processing thread is working on the first buffer, while reader thread is working on second buffer. These two thread (reader and processing) keep on swapping thread until all the data is read from the source (file). This overlap of I/O with computation makes the overall processing faster. Data itself is fetched in chunks to make the reading faster. We tested I/O speed for different chunk sizes 10K, 20K, 40K, 80K, 1M, but didn't see significant difference. We used 10K for our experiments.

3.3.8.2 Data Formatter

This component is responsible for reading pre-fetched data and converts it to proper format. The data is composed of sampled-time (μses) and corresponding current values (nano-amperes). Reading data in floating point format and then converting to integers and scaling appropriately consumes more time. So we read data in ASCII (character) format from the source, converted carefully to integers to get μsecs and nano-amperes respectively. This process makes the reading process pretty faster as compared to the former method. When

sufficient amount of data is formatted by Data Formatter, we hand-over it to the GPU Manager component, (step 3).

3.3.8.3 GPU Manager

Transferring data from CPU to GPU, launching GPU Kernel, and copying data back from CPU to GPU are the functions of GPU Manager (step 4). GPU Manager uses multiple streams to transfer data from the Host memory to the Device memory. The purpose is to overlap data transfer (I/O) with kernel launch (computation). Here processing of multiple streams are overlapped with one another, given that steps inside a given stream are synchronous. Within kernel, the input data is divided equally into chunks which are mapped to the parallel processing threads. Each thread works on its own chunk to detect the peaks in it. All threads simultaneously operate on its chunk to detect peaks in the data. This is a variable output per thread problem. Since peaks in the input data are randomly distributed, some thread would detect more peaks than others; some won't detect any peak in the assigned chunk. The attributes of peaks (width, Amplitude) detected by each thread in its chunk are accumulated in a shared result memory on the Device. This result memory is asynchronously transferred (copied back to the Host memory) as soon as the results from a given stream are accumulated at the Device. These results are merged at the Host to generate consolidated result. The Data Formatter Unit at the CPU core becomes idle due to slow I/O. Similarly GPU device becomes idle while Data formatter is formatting the fetched data. To overcome these I/O bottlenecks, we use double buffering at both levels.

3.3.8.4 Result Analyzer

This component takes care of the peak information (metadata) obtained from the Device. Initially, this is not in the exact format to be delivered to the user. The Result Formatter after post-processing (removing zeros from the result array and calculating width of the peak) form the scatter plot of the detected peaks. Since the peaks detected out of the measure data are

quite fewer in number, we intend to perform post-processing of result on the Host rather than on the Device. This peak information is further post-processed to extract the required features i.e., width and minimum of each detected peak. This information is then used to get the scatter plot of the peaks with peak-width on x-axis, and its amplitude; the minimum current value on y-axis as shown in figure 3.28.

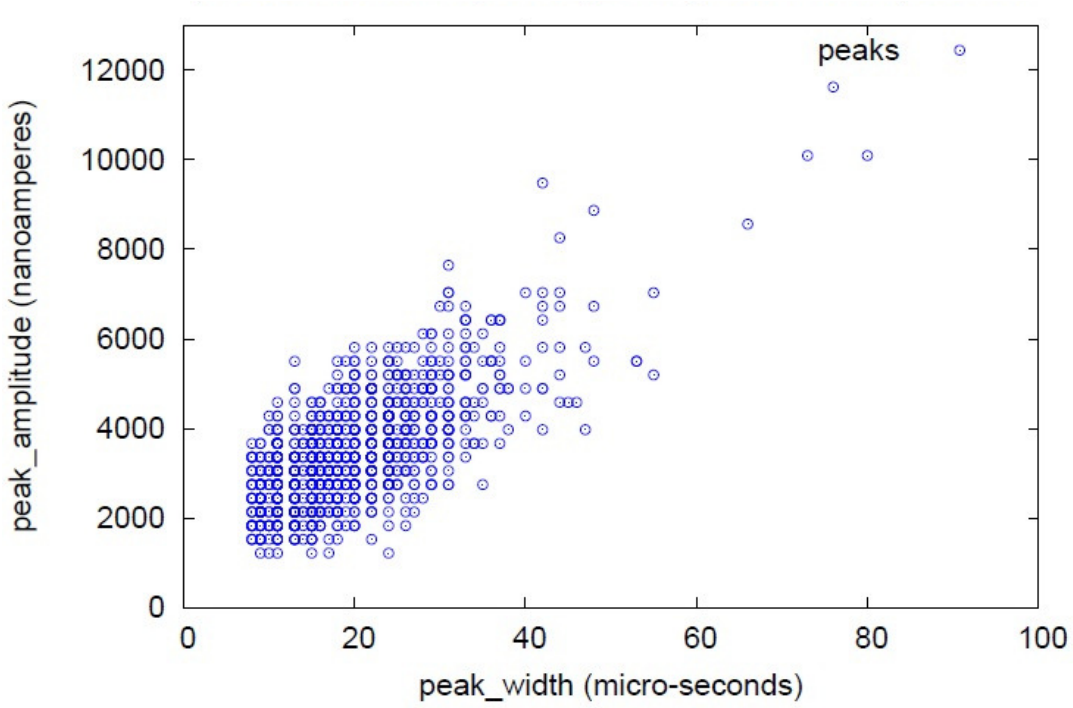

Figure 3.28 Shows the pulses detected in 120 million points of data using Moving Average technique; Threshold is kept 1596 nano-Amperes below baseline, window size kept is 500 points, minimum acceptable width is 5 micro-Amperes, and maximum acceptable width is 100 micro-Amperes. Reprinted by permission from Elsevier [168]

3.3.9 Implementation

In our design tested performance with different number of buffers; 2, 3, and 4. Littler improvement is seen with this increase in number of buffers at the cost of doubling the usage of memory. The speed is bound by float to integer conversion (using C command ASCII to float; atof() command) which is hampering the performance increase due to multiple buffers. That's

why we decided on using 2 buffers rather than more buffers to save our memory. For the buffers size used by Data Pre-fetcher to get data into system in real-time, we tested performance by varying buffer sizes from 1K to 10K, no significant performance was seen, so we decided to use 1K buffers. Buffer used by GPU-Manager to offload data to the GPU is kept at least 57MB which is equivalent to 40 million points (converted to integer format). We also tested our performance for Input size of multiples of 57MB. The performance increase is proportional to the increase in size of data. By this we observed that our system is scalable with different size of inputs at the CPU level, and at the GPU level.

3.3.10 Evaluation

In this section, we present the evaluation of our design. We first describe our evaluation methodology, followed by the experimental setup that we have used in our evaluation. We then compare the performance of our algorithm implementations with the existing state-of-the-art, and compare executing the spike detection mechanism on GPU with the corresponding execution on the CPU.

3.3.10.1 Methodologies

We evaluated our system by measuring two aspects of our system; the algorithmic performance (in terms of peak detection), and the System's performance (in terms of speed) for the data generated in real-time. For evaluating algorithms detection capability, we have shown the tracking of different threshold techniques for the given data with varying baseline. We observed that fixed threshold technique does not keep track of the data with varying baseline, while with dynamic threshold technique; threshold adapts itself to the changing baseline.

From System's performance point of view, we tested the sampling rate with different amount of data generated in real-time. With this scalability of the system was also measured. The results show that system is scalable with varying data inputs.

3.3.10.2 Experimental Setup

For our CPU implementation, we used ASUS laptop with Intel Core i3 CPU consisting of 4 cores; each operating at 1.2 GHz. This machine has 4GB of RAM with only 2.9GB available for user applications. For both sequential code, and CPU coupled with GPU, we used the above mentioned machine. For parallel implementation, we used GeForce 310M GPU with 16 cores clocked at 1.5GHz, and 1GB GPU memory. We used C for CPU, and CUDA for GPU programming.

We used two configurations for our experimental evaluation, especially for performance evaluation. Conf I is an optimized CPU implementation of detection algorithms with advanced I/O techniques. Conf II is a GPU implementation of each detection algorithm coupled with advanced I/O techniques. Conf II is about 5x faster than original electrical measurement setup which is operating at peak rate of 454 K samples per second.

3.3.10.3 Algorithms performance measurements

We show that our algorithms keep track of the time-varying baseline. Figure 3.29 shows the results being obtained using the fixed threshold technique, and the baseline-tracker technique. Figure 3.30 shows the tracking of baseline of the rolling average technique. Part (a) and (b) of Figure 3.30 shows the tracking of the rolling average technique with No Roll-back. The No Roll-back depicts the situation when once the average is calculated, e.g., on *w* number of points, those w points are discarded in the detection process and detection process starts from *w+1st* point instead. We observe best tracking with the rolling average technique out of all three algorithms.

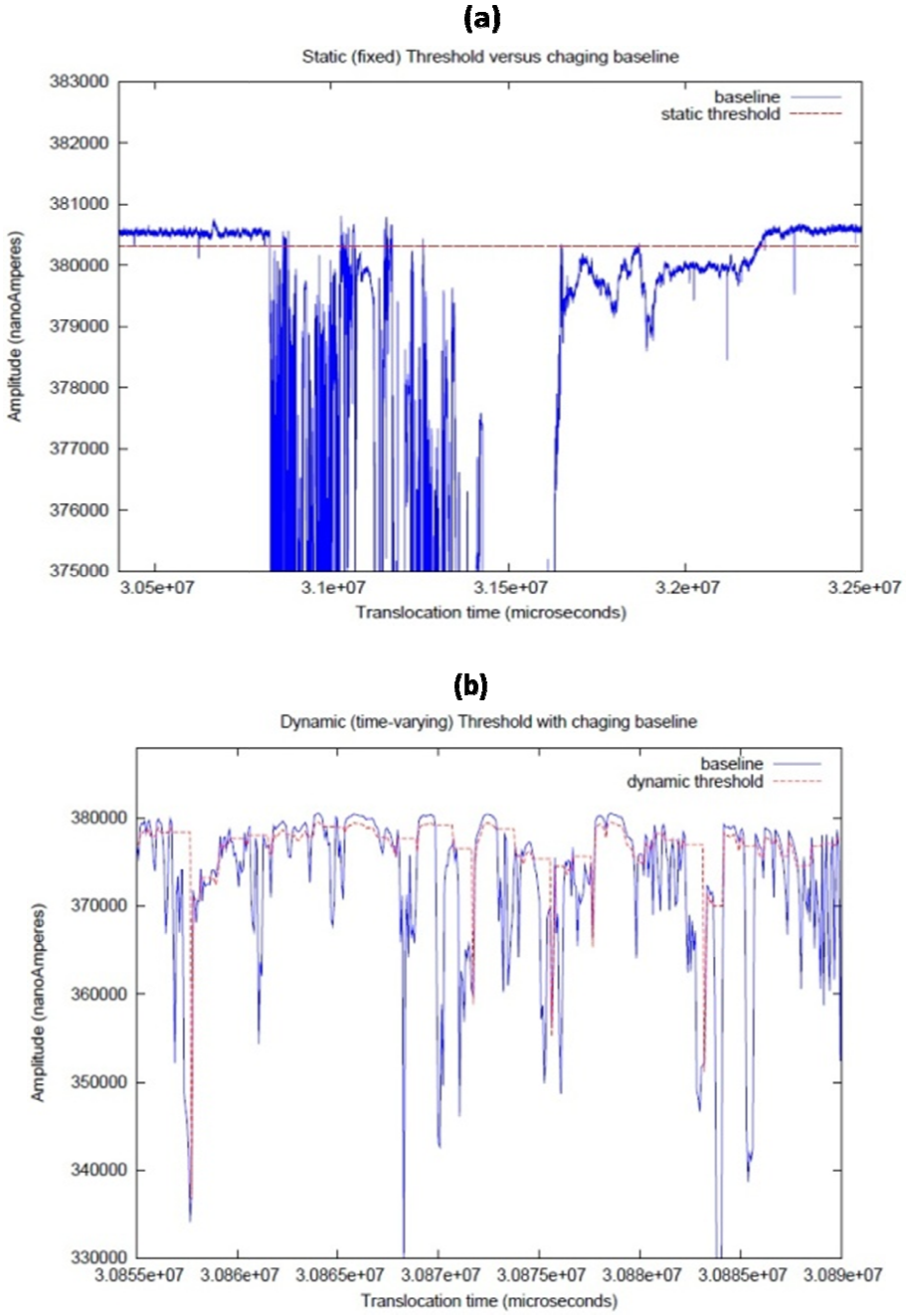

Figure 3.29 Shows the plots for static and dynamic threshold (baseline-tracker) techniques, (a) static threshold (selected 1000 nanoamperes below baseline) cannot detect pulses when the baseline is very noisy. (b) baseline-tracker technique shows how it keeps track of the baseline. Reprinted by permission from Elsevier [168]

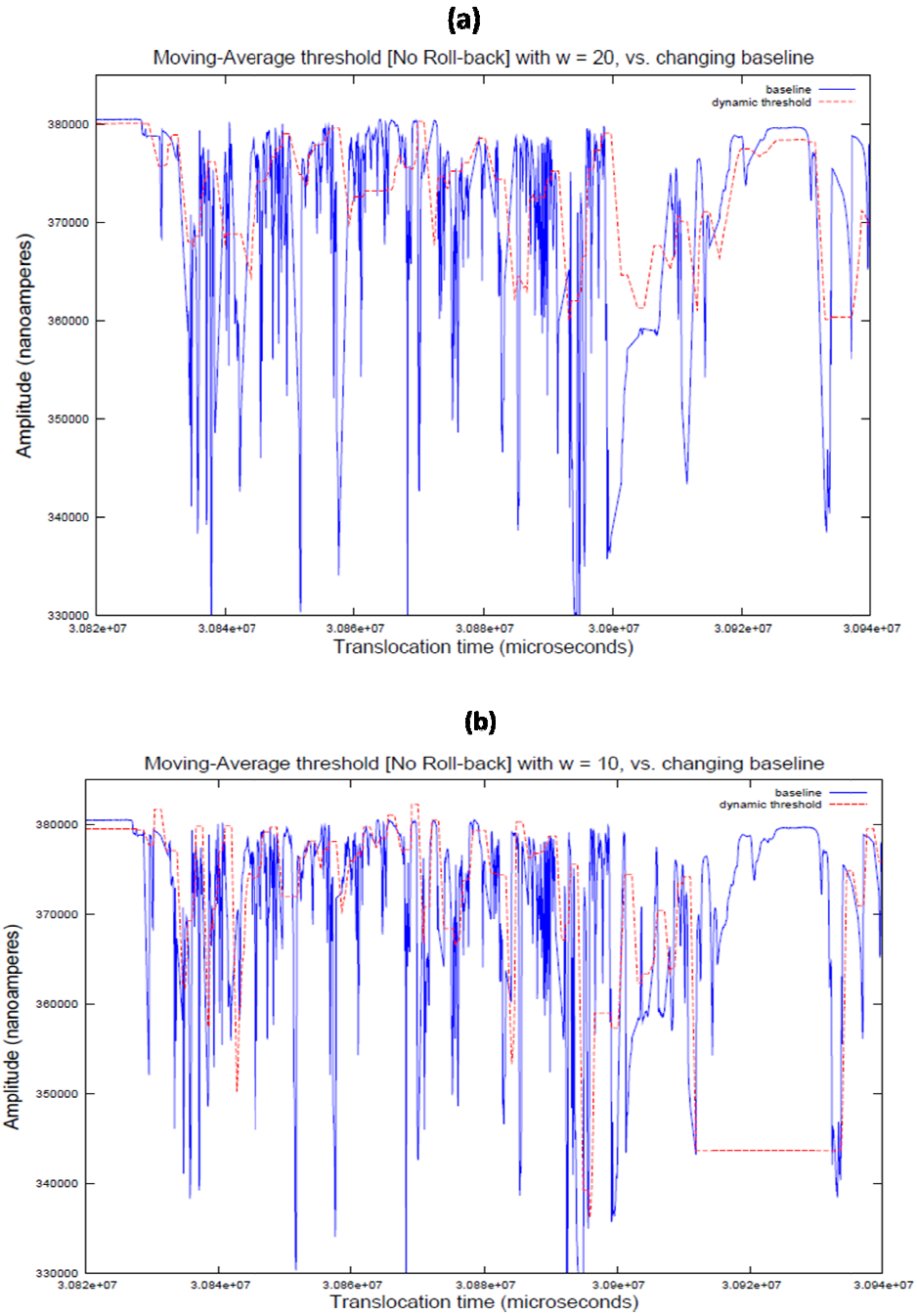

Figure 3.30 Shows the plots of moving average without Roll-back technique, tolerance: 0.3% (1143 nano-amperes below baseline), sampling rate of data: 75 µseconds, tracking for window size: (a) window-size: 750 µses, (b) window-size: 900 µses without rolling-back on data-points. Reprinted by permission from Elsevier [168]

3.3.10.4 System Output measurements

The outputs of all the three techniques are shown in the Figure 3.31. The fixed threshold technique detects the pulses and shows better overlap with the manually detected approach, but we also found much noise. Baseline-tracker method detects pulses without noise but the detected pulses are not overlapping well to the manual detection. Moving Average approach has the best overlap with the manual approach and the detection is more tolerant to noise.

For static and dynamic approaches the threshold is kept 1200 nanoamperes below the baseline, which detects the pulses more accurately as compared to other levels of threshold. Equivalent tolerance for moving average technique is 2.3%, but we have used 2.8% with which we have found better overlap with the manual detection.

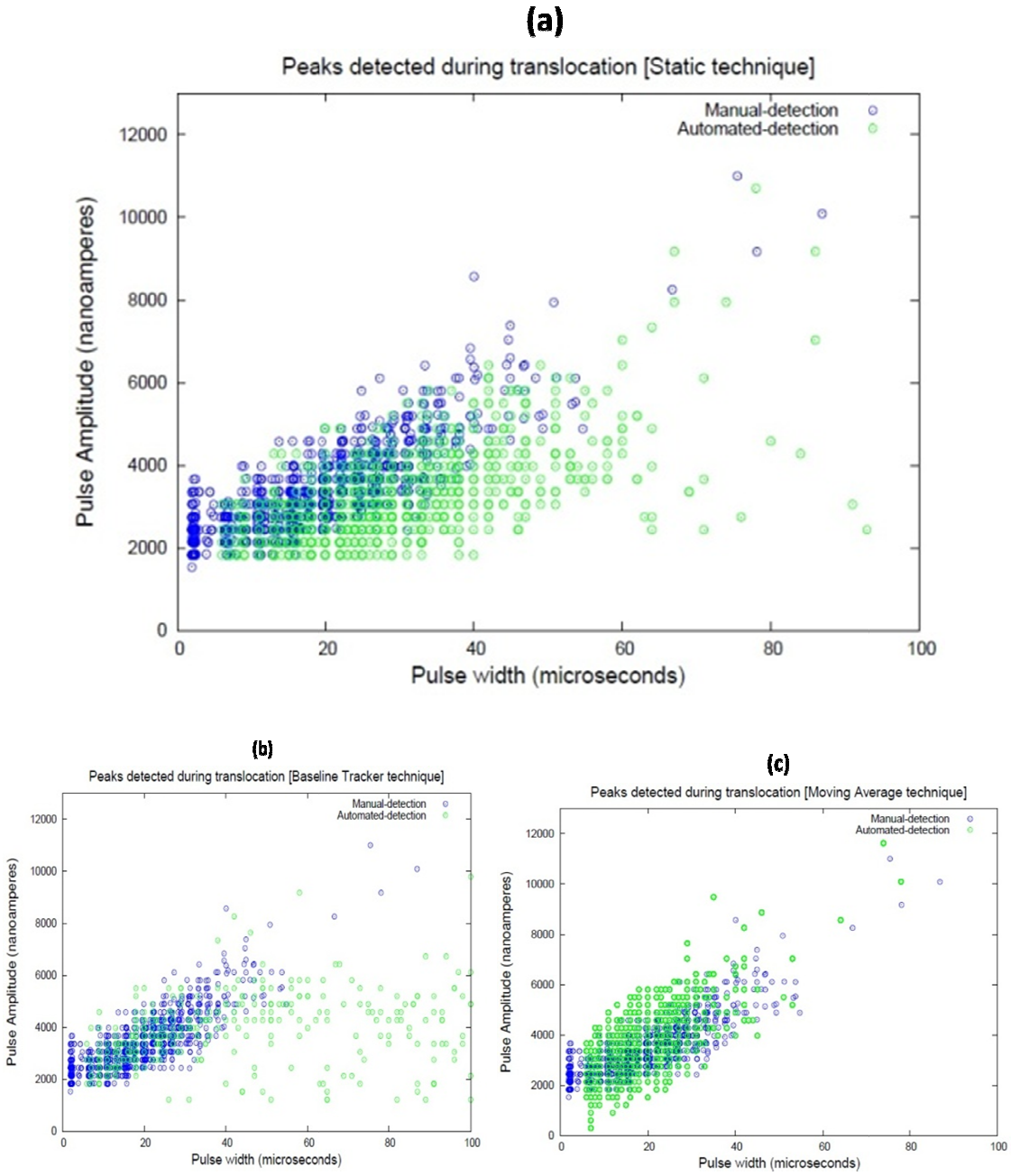

Figure 3.31 Shows the comparison of manual detection with automated approach. (a) Static technique vs. manual approach, (b) baseline-tracker technique vs. manual approach, (c) Moving Average vs. manual approach. Reprinted by permission from Elsevier [168]

3.3.10.5 System (GPU) Performance measurements

GPU processing time and overall system (end-to-end) time for different data sizes using static threshold technique, baseline-tracker technique and moving average technique are shown in Table 3.2, Table 3.3 and Table 3.4 respectively. The temporal performance is measured for data varying from 110 MB to 3.3 GB. The execution time is also found to be proportional to the size of data. The performance increase, as shown in Table 3.5, is proportional to the increase in data size. This shows that our system is scalable with different input sizes at the host and device levels.

We observe that the data transfer time in the static threshold and baseline-tracker techniques is almost equal to the computation time, while in the case of the Moving Average technique, data transfer is almost similar to other two techniques but computation part takes more time. More computation time in moving average is due to the fact that every thread calculates the seed threshold for its data chunk as compared to the single threaded program on the CPU where this step is performed only once. Each thread initially loads its window with fresh data points from the assigned chunk rather than just adding the next data point and subtracting the first data point in the window which is the case for rest of the data points in the chunk.

Table 3.2 Time taken by GPU kernel: GPU kernel with data transfers and corresponding CPU code using Static threshold Technique. Reprinted by permission from Elsevier [168]

System-Input (GB)	GPU-Input (MB)	GPU-kernel + Data-transfer time (msec)	CPU-time (msec)
0.11 (4 M points)	32	25	28.93
0.54 (20 M points)	180	125.32	145.39
1.1 (40 M points)	320	250.74	295.02
1.7 (60 M points)	480	376.16	413.78
2.2 (80 M points)	640	501.43	506.4
2.7 (100 M points)	800	626.86	669.04
3.3 (120 M points)	960	752.18	782.37

Table 3.3 Time taken by GPU kernel: GPU kernel with data transfers and corresponding CPU code using Baseline-tracker threshold technique. Reprinted by permission from Elsevier [168]

System-Input (GB)	GPU-Input (MB)	GPU-kernel+Data-transfer time (msec)	CPU-time (msec)
0.11 (4 M points)	32	24.73	25.35
0.54 (20 M points)	180	123.56	147.57
1.1 (40 M points)	320	239.67	287.02
1.7 (60 M points)	480	366.93	428.13
2.2 (80 M points)	640	492.12	522.44
2.7 (100 M points)	800	612.35	675.87
3.3 (120 M points)	960	746.6	771.96

Table 3.4 Time taken by GPU kernel: GPU kernel with data transfers and corresponding CPU code using moving average technique. Reprinted by permission from Elsevier [168]

System-Input (GB)	GPU-Input (MB)	GPU-kernel+Data-transfer time (msec)	CPU-time (msec)
0.11 (4 M points)	32	69.14	31.26
0.54 (20 M points)	180	345.68	156.29
1.1 (40 M points)	320	690.95	315.57
1.7 (60 M points)	480	1036.63	476.24
2.2 (80 M points)	640	1382.21	640.21
2.7 (100 M points)	800	1727.75	810.42
3.3 (120 M points)	960	2072.7	988.08

Table 3.5 Time taken by GPU for different input sizes using the moving average algorithm, and overall system time. Reprinted by permission from Elsevier [168]

System-Input (GB)	GPU time (msec)	System time (seconds)	
		Cold Buffer-cache Time	Hot Buffer-cache time
0.11	55.9	2.43	0.558
0.55	278	9.3	2.55
1.1	555.7	21.64	4.93
1.65	834.9	28.5	7.36
2.2	1115	42.2, 31	9.651
2.75	1394	54.5, 51.4	13.1
3.3	1718	70, 67, 49	14.6

3.3.11 Conclusion

We were able to design real-time system for detecting peaks in millions of data points generated from DNA translocation through the nanopore. Three different threshold detection techniques are employed, and its impact on the detection of peaks was analyzed in the case of

time-varying baseline and noisy data. By employing double buffering technique at two levels we achieved significant performance improvement. Using GPU for processing input data further accelerated the process of peak detection. This work can have wide implications when many bio-sensors are measuring data in parallel from the physiological platforms. We believe that this work can be extended to explore the DNA translocation pulse shapes during real-time detection.

CHAPTER 4

SOLID-STATE MICROPORES FOR DETECTION OF CANCER CELLS

4.1 Introduction

Precise quantification of Circulating Tumor Cells (CTCs) in the peripheral blood of cancer patients is believed to help against metastasis of disease. The dissemination and deposition of CTCs in different tissues through peripheral blood and evolution of secondary tumor was first proposed in late 1980s [169]. The CTCs are believed to detach from the solid tumor and spread through blood to secondary tissues [170]. Early stage detection and quantification of CTCs is a challenge as they are very low in number ranging 1 – 100 per milliliter of blood [103-105, 108]. Enumeration of CTCs in peripheral blood can be helpful in determining the effectiveness of therapeutic interventions and forecasting the disease prognosis. The CTC detection and isolation has been reported for a number of cancer types including breast, bladder and renal cancers [95, 171, 172].

Different strategies have been reported for the quantification and isolation of CTCs including polycarbonate membrane based blood filtration (size based isolation), microfluidic flow cytometry, chromatographic separation and use of immunomagnetic systems (magnetic dynabeads) [108, 119, 120, 122, 173-176]. All these approaches either give lower than desired yield or involve fluorescent tags for counting. Some of the processes are laboratory dependant and very expensive requiring equipment like optical flow cytometry. In immunomagnetic systems, the dynabeads are functionalized with anti-epithelial antibodies specific for antigen bearing target carcinomas. These typically give yield of approximately 70% [116]. The size based separation techniques give higher throughput and yield of approximately 85% but require laser scanning cytometry. In such approaches a large number of leukocytes are also retained on the membranes after filtration which complicate the cell enumeration using laser scanning

[119]. Procedures involving Reverse Transcription-PCR were reported to give higher yields but are prone to advanced laboratory equipment and challenging sample handling [177]. For label free detection of pathogens, the electrical microflow cytometers are widely used in research [178]. The major advantage of using electrical system is that fluorescent labels are not needed for cell counting. For single cell analysis, the electrical and microfluidic systems require flow of cells in single line fashion. A recent report uses three syringe pumps to maintain a single line flow of the human CD4+ T lymphocytes [178]. When cells pass through the channels, the embedded electrodes are used to measure electrical impedance of a single cell. Although elegant, but such techniques have low throughput.

There is a need of efficient, inexpensive, label free and highly sensitive approaches to detect CTCs from human blood. In this paper, a technique is described that uses single solid-state micropore for renal cancer cell detection from whole blood. It has been previously reported that cancer cell diameters are larger than red and white blood cells [120]. The solid-state nanopores have emerged as a novel device for deoxyribonucleic acid (DNA) detection, protein analysis and pathogen detection [55]. This work utilizes solid stat micropores (10 to 20 μm) instead of nanopores. The translocation mechanism here depends on the applied fluidic pressure instead of charge. Although the cells have negative potential on their membrane but we observed that they cannot be translocated through the micropore using applied electrical potential due to their larger mass compared with the DNA and proteins. When the cells suspended in electrolyte are translocated through the micropore, these give distinctive pulses by the physical blockage of current flow through the pore. Pulse magnitude corresponds to the cell size, pulse duration corresponds to the time required to pass cell through the pore and pulse shape gives the 3D profile of how cell is passing through the pore.

4.2 Materials and Methods

All the chemicals were purchased from Sigma-Aldrich (St. Louis, MO) unless noted otherwise.

4.2.1 Micropore Device Fabrication

The micropore fabrication process started with 200 nm oxidation of double side polished (100) Si wafer. G-line photolithography was employed to open a square window on one side of the Si wafer followed by SiO_2 wet etching using Buffered Hydrofluoric (BHF) acid. Tetramethylammonium hydroxide (TMAH; GFS Chemicals) wet chemical etching was used to etch through the square opening at 90 ^{o}C. This etching process was stopped when Si was etched through the whole wafer thickness and only ~200 nm of oxide membrane was left on other side of the wafer. The oxide square window size was 50 µm x 50 µm. The whole wafer was cut into 5 mm x 5 mm dyes. Focused ion beam (FIB) was used to drill micropores of different diameters in thin oxide membrane. The diameter of the micropore depends on the FIB beam current and drilling time. Higher the ion milling current and drilling time, larger would be the micropore diameter. The diameter of the micropore also depends on the thickness of the oxide membrane and material composition of the membrane. The FIB drilling process can be replaced with second photolithography process run using backside alignment and mask having circular micropore features followed by BHF etching for pore opening. The whole process flow is shown in Figure 4.1. The oxide membrane thickness was 200 nm to make sure that only single cell could pass through the 12 µm diameter micropore at a time.

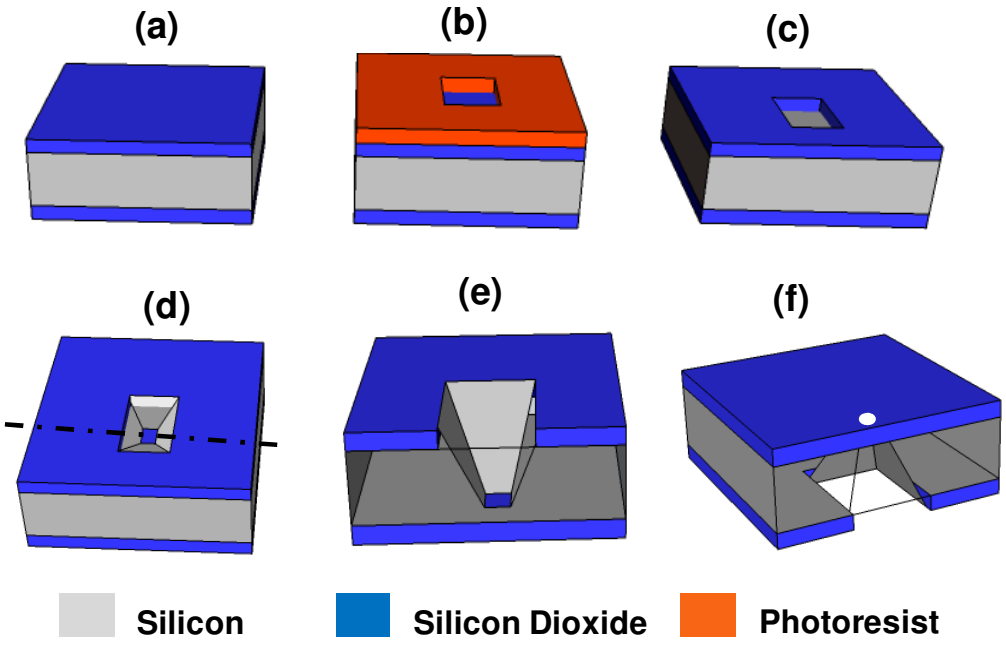

Figure 4.1 Shows the process flow of solid-state micropore fabrication. (a) After oxidation of Si wafer. (b) After photolithography, square window is opened in photoresist. (c) After BHF etching, pattern is transferred to oxide. (d) After TMAH wet etching. (e) Cross-section view of the pyramid structure holding oxide membrane. (f) After FIB drilling to make micropores in thin oxide membranes. Reprinted by permission of The Royal Society of Chemistry [179]

Once the pores were drilled, the scanning electron microscope analysis showed that the inner walls of the pores were not smooth. It was observed that rough inner wall surface of micropore was prone to pore blockage during cell translocation. And secondly it was believed that the rough oxide surface could rupture the cell membrane during translocation. In order to make the pore walls smooth, it was put inside the heating furnace at a temperature of 1050 ^{o}C for 5 minutes. The higher temperature can significantly change the pore diameter while the temperature less than 1000 ^{o}C did not give smoothing effect significantly. It has been shown in Figure 4.2.

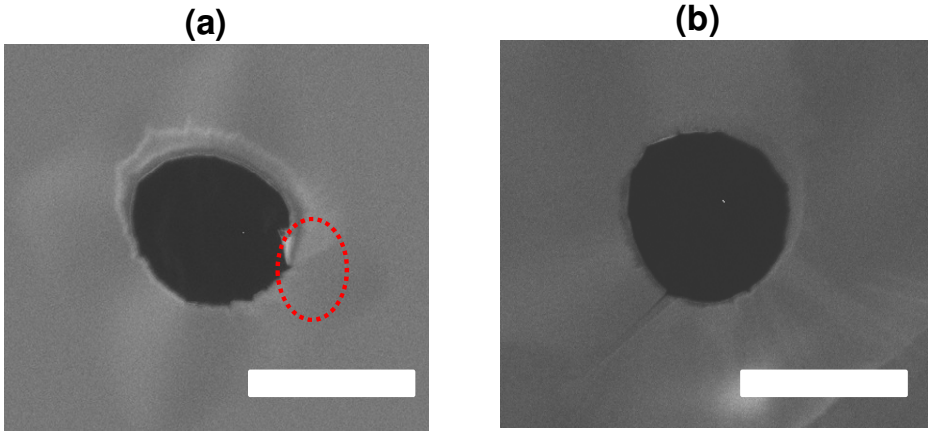

Figure 4.2 Shows the solid state micropore drilled in 200 nm thick $Si0_2$ membrane using FIB. (a) The micropore just after drilling. The red circle shows the rough structure inside and on the edges of the pore walls. (b) The sample heated at 1050 ^{o}C for 5 minutes in furnace having nitrogen flow of 10 sccm. It clearly shows that the micropore edges and inner wall surface became smooth which helped in cell translocation and reduced probability of the breaking of the cell outer membrane. The pore became more circular after heat treatment. (Scale bar = 10 µm). Reprinted by permission of The Royal Society of Chemistry [179]

4.2.2 Measurement Setup

Two compartments measuring device was made using teflon blocks. The micropore chip was sandwiched between these two teflon blocks (McMaster-Carr). Polydimethylsiloxane (PDMS; Dow Corning, Midland, MI) gaskets were used on both sides of the chip to avoid leakage of solution. Ag/AgCl electrodes were used for current measurements. The electrodes were connected to data acquisition cards (National Instruments) for voltage biasing and current measurement. One compartment of the teflon block was connected to a syringe pump (Harvard Apparatus, Holliston, MA) through a tubing adapter (McMaster-Carr). The measurement setup is shown in Figure. 4.3. Cells solution with standard phosphate buffered saline (PBS) was injected in one compartment connected to syringe pump while the other compartment was filled with PBS only. When cells were allowed to translocate through the single pore, it changed the conductivity of the pore. The change in the conductivity of the pore is due to the physical blockage of the pore with cells while translocating through it.

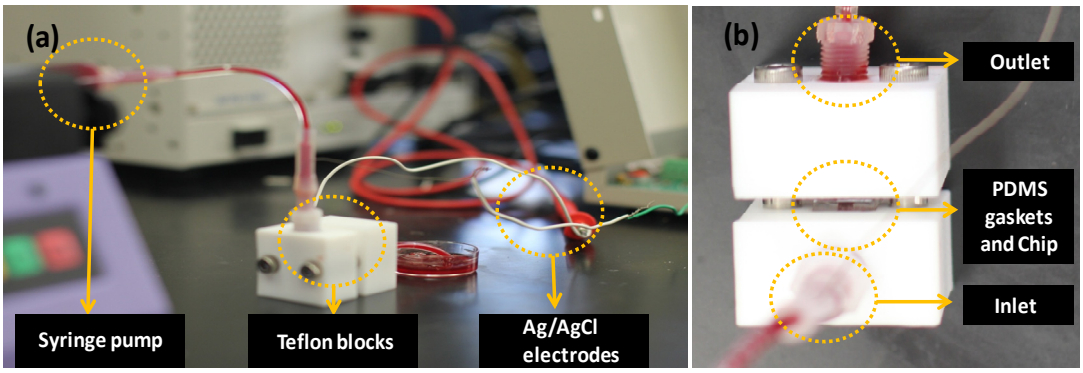

Figure 4.3 Shows the micropore device measurement setup. (a) Syringe pump connected to one of the reservoirs made with teflon blocks. The chip with single micropore is sandwiched between two teflon blocks using PDMS gaskets to avoid any leakage. One Ag/AgCl electrode is inserted in tubing at inlet and another at the outlet. The biasing and data collection is done with LabView software routines using data acquisition cards. (b) The top view of the teflon blocks, showing the PDMS gaskets used for sealing the micropore device. Reprinted by permission of The Royal Society of Chemistry [179]

4.2.3 Effects of Oxide Membrane Thickness

The micropore diameter and oxide membrane thickness plays a critical role in cell translocations. Pore diameter smaller than 8 µm did not allow the cancer cells to pass through it easily and pore was prone to blockage. And we believe that more the membrane thickness, there are more chances of pore blockage as interactions of cell walls with hydrophilic pore walls would increase. If the thickness of the membrane is doubled, the physical area of contact of cell membrane with the pore inner walls would also be approximately doubled and there would be more chances for cells to get attached on the pore walls due to hydrophilic phosphate heads of lipid bilayer. The thin membrane also made sure that only one cell can translocate through the pore at a time.

As described earlier, the diameter of the cancer cells are larger than RBCs and WBCs. The cancer cells gave distinctive signal while translocating through the micropore. When imaged under the optical microscope, most of the renal cancer cells were found having diameters more than 20 µm while RBCs and WBCs were smaller in size as shown in Figure 4.4.

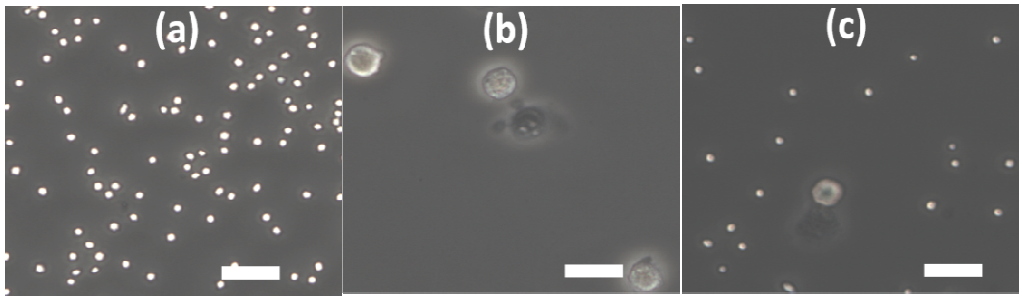

Figure 4.4 Shows the optical micrographs of the cell suspensions on glass slide. (a) Whole blood diluted with PBS. (b) Renal cancers cells suspended in PBS. (c) Renal cancer cells mixed with whole blood and suspended in PBS solution. All the images were taken with same lens and magnification. The scale bar is 50 µm. Reprinted by permission of The Royal Society of Chemistry [179]

4.2.4 Primary Renal Cancer Cell Culture (Human Derived)

Human renal derived cancer cells found in brain tissue were obtained from consenting patients at the University of Texas Southwestern Medical Center (Dallas, TX, USA) with the approval of the Institutional Review Board. The collected brain tissue containing metastasized renal derived cancer cells were chemically dissociated with papain and dispase (both 2%) and cultured in Dulbecco's modified Eagle's medium (DMEM) with 10% fetal bovine serum.

4.2.5 Isolation of Red Blood Cells (RBCs) and White Blood Cells (WBCs) from Bovine Blood

The whole bovine blood was purchased from Lampire Biological with K_2-EDTA as anticoagulant. WBCs were isolated from the whole blood using OptiPrep^{RM} density gradient medium. Whole blood was mixed with OptiPrep at a ratio of 1:8. Half ml of Tricine Buffered Saline (TBS; 0.85% NaCl, 20 mM Tricine-NaOH, pH 7.4) was layered on top of mixture carefully so that it did not mix with the blood. The whole blood solution was centrifuged at 2000 g_{av} for 15 minutes. The top transparent layer was removed carefully upto 0.5 ml below the meniscus. The collected material was washed three times with PBS for 10 minutes each. The WBCs were collected from the bottom of centrifuge tube and resuspended in PBS. For RBC isolation from whole blood, the whole blood was centrifuged at 2000 g_{av} for 15 minutes. RBCs were collected carefully from the bottom of the centrifuge tube and resuspended in PBS again.

4.3 Results and Discussions

In order to demonstrate the capability of the device as a microflow cytometer, different concentrations of renal cancer cells were mixed with PBS and run through the 12 µm pore at flow rate of 10 µL per min and current sampling time of 2.5 µsec. The same experiment was repeated for 20 µm pore at a flow rate of 10 µL per min. The two experiments showed similar results. The device showed excellent results in renal cell counting as shown in Figure 4.5. When a single cell tried to translocate through the pore, it showed distinctive current blockade signals. The two cell counting measurements, one through the micropore and other by hemocytometer, were in excellent agreement with R^2 value of 0.9999.

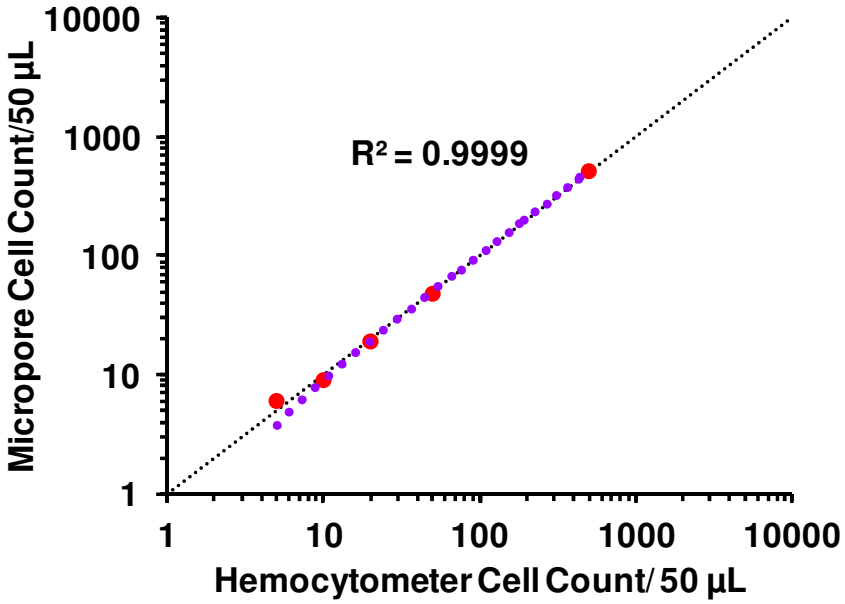

Figure 4.5 Shows concentration comparison between micropore device and hemocytometer cell counter device for 5 different concentrations of renal cancer cells (5 to 500 cells/50 µL). The plot is for 12 µm pore at flow rate of 10 µL per min. The dot line (purple) is a linear regression of 5 samples (R^2= 0.9999) and indicates good correlation between the two methods. Reprinted by permission of The Royal Society of Chemistry [179]

To check the stability of the micropore device, we analyzed the electrical profile of cells (e.g., renal cancer cells, RBC and WBC) at three different timepoints: 1, 5 and 10 minutes. The

cell profiles remained stable as shown in Figure 4.6. These results clearly demonstrated reliability and stability of the micropore for cell counting purpose.

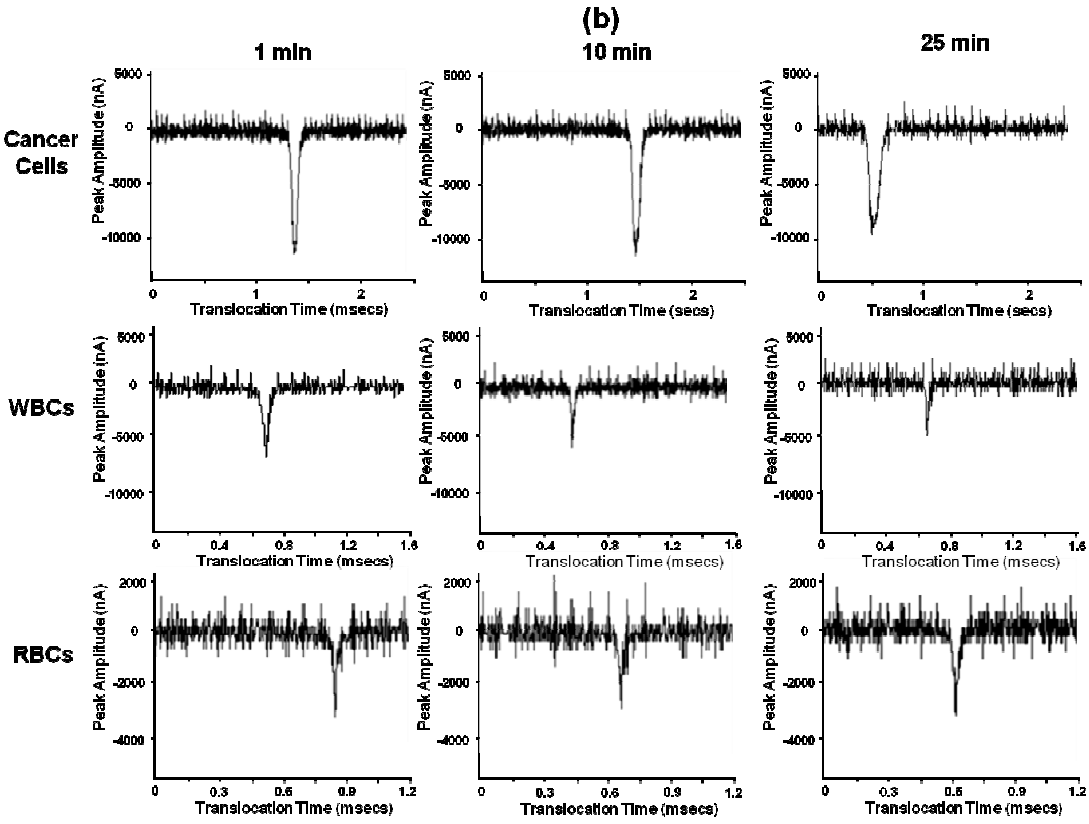

Figure 4.6 Shows the translocation pulses for all cell types (Cancer Cell, WBCs, RBCs) at different time points (1, 10 and 25 mins). The device shows the stable behavior. Reprinted by permission of The Royal Society of Chemistry [179]

We showed that the micropore device can discriminated between different cell types. The renal cancer cells were mixed with PBS at concentration of 1000 renal cells/mL of PBS solution. The flow rate was optimized for maximum throughput and we found that above 20 µL per minutes, the device started missing useful information for cancer cells during translocation. Below 10 µL per min flow rate, the throughput of our device was lower. The optimized flow rate was 10 µL per min. The optimized current sampling time was thus set at 2.5 µsec. Although at higher current sampling time, the measuring equipment gave lesser baseline noise, but some

useful information could be lost. Below 2.5 µsec sampling time, there was more noise which suppressed some current blockage signals during cell translocations. The applied bias was 5 volts. The RBCs and WBCs were separated using protocols described above. RBCs and WBCs were mixed in PBS separately at equal concentrations of 1,000 cells/mL. They were processed using the same micropore device (Flow rate = 10 µL per min, Current sampling time = 2.5 µsec, Applied voltage = 5V). For 12 µm pore, less number of RBCs and WBCs were detected than expected. The sizes of the RBCs and large number of WBCs were smaller than the pore diameter. When smaller cells passed through the 12 µm pore, they could not completely block the pore and therefore did not give significant pulse signals. The characteristic shape of the pulse blockade signals also depends on the orientation of the cells passing through it. The measurement setup can record current samples at such a high rate that it can accurately track the 3D profile of the larger cells (renal cancer cells), but in case of cells with smaller sizes, equipment with higher sampling rate would be needed. Nevertheless, the micropore chip showed significantly different current blockade pulse for all the three types of cell suspensions as shown in Figure 4.7. More than 85% of cancer cells showed different pulse widths and amplitudes. The pulse shapes are shown more closely in Figure 4.7 (b-d). When the cancer cell translocated through the 12 µm pore, it squeezed through the pore because its diameter was larger than the pore size. While squeezing, it physically blocked the pore and showed significant current dips. All of the pulses for renal cancer cells depicted very smooth bell shape which shows that only one cancer cell passed through the pore at a time. When RBCs pulses were analyzed, most of the pulses were double or triple spiked which suggested that significant signal could be measured only when clumps of two or more RBCs passed together as shown in Figure 4.7 (e-g). WBCs have a range of cell diameters (5-18 µm). When the WBCs of larger size translocated through the 12 µm pore, they gave smooth pulses.

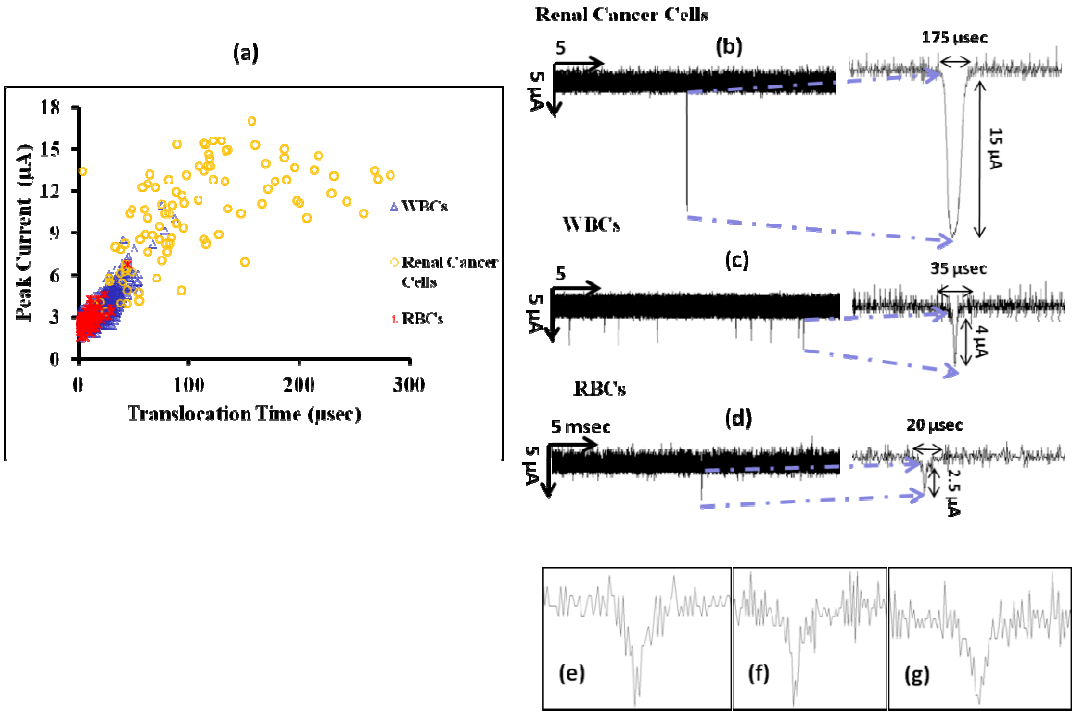

Figure 4.7 Shows the distribution of the cell data according to their size while translocating through 12 µm pore. (a) This plot points out the distribution of cancer cells from the other cell types. (b), (c) and (d) show pulses for Cancer cells, WBCs and RBCs, respectively. It depicts that the pulses for cancer cells showed more current blockage and more translocation time when compared with other cell suspensions. (e-g) Show the close-up of the RBCs pulses. Almost all of the pulses were double spiked or irregular shaped in contrast to the pulses from cancer cells which were smooth and bell shaped. It suggested that the device only showed signals for RBCs when they were clumped together. Reprinted by permission of The Royal Society of Chemistry [179]

The average translocation time and peak amplitude for three cell types is shown in Table 4.1. Statistical analysis of data (ANOVA one-way Analysis) showed that there was statistically significant difference (P-value < 0.01) between all cell types (Table 4.1). Statistical analysis was based on the translocation time and peak amplitude values.

Table 4.1 Translocation time and amplitude for different cell types for 12 µm pore. Where *P<0.01 between CTCs and others; #P<0.01 between WBCs and RBCs. Reprinted by permission of The Royal Society of Chemistry [179]

Cells Types	**Average Translocation Time**	**Average Peak Amplitude**
CTCs	138.16 ± 192.4	10.56 ± 3.51
WBCs	18.53 ± 11.24*	3.34 ± 1.05*
RBCs	6.63 ± 6.57*#	2.56 ± 0.59*#

For optimal pore diameter, the same experiment was repeated with 20 µm pore diameter. The pulse amplitude was reduced for all the cell suspensions when compared with 12 µm pore, as expected. Translocation time and pulse amplitude from all three types of cells were significantly different as shown in Figure 4.8. Very few RBC clumps were detected because of the larger pore diameter. All the applied conditions were same as for 12 µm pore. Using 20 µm, the average translocation time and peak amplitude for three cell types is shown in Table 4.2. Statistical analysis of data (ANOVA one-way Analysis) showed that there was statistically significant difference (P-value < 0.01) between all cell types (Table 4.2). Statistical analysis was based on the translocation time and peak amplitude values.

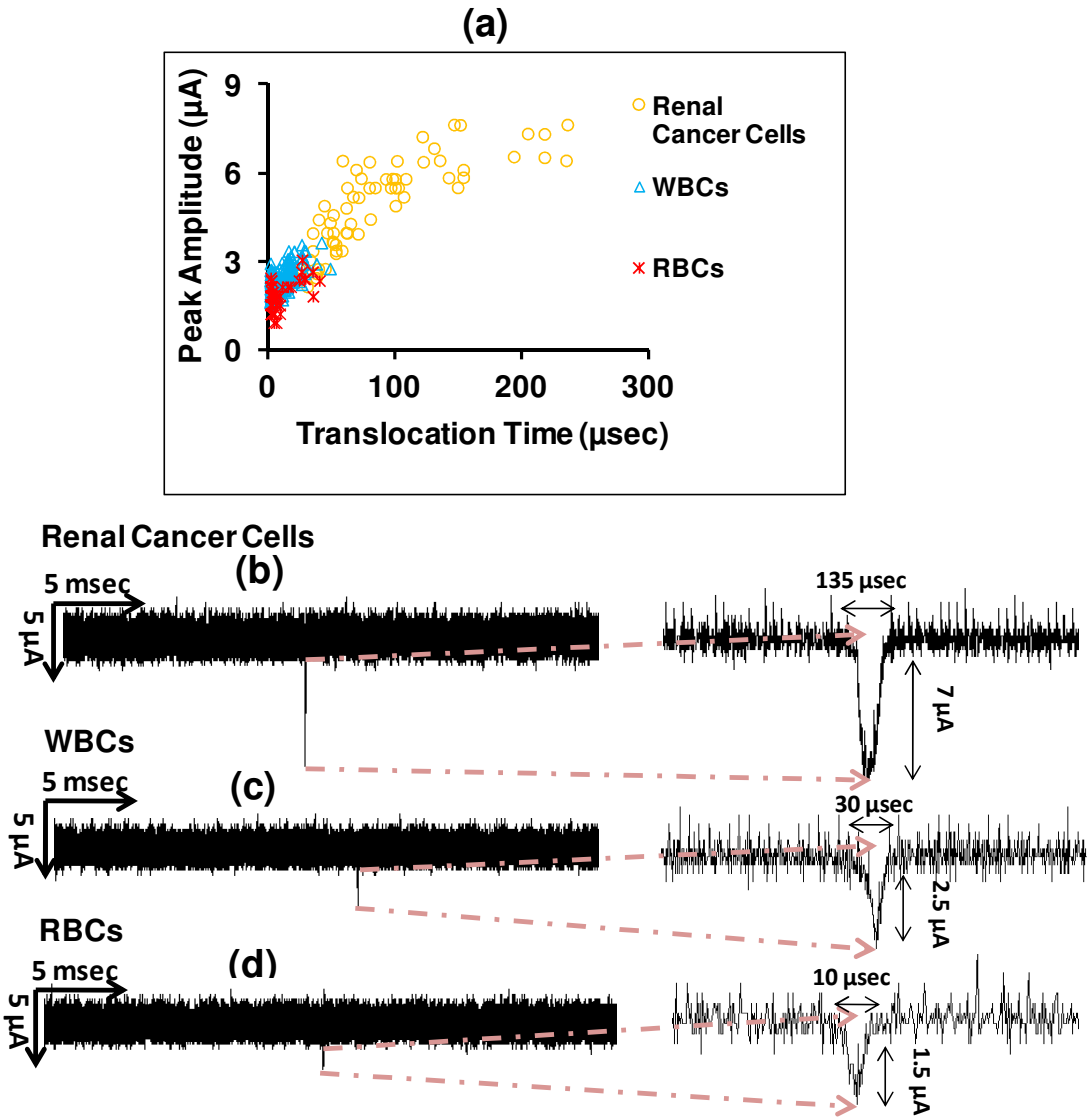

Figure 4.8 Shows the distribution of the cells according to their size while translocating through 20 µm pore. (a) Plot shows reduction in pulse magnitudes in comparison to those for the 12 µm pore. The plot shows distinct behavior for cancer cells in contrast to other cell types. (b-d) Shows the pulse data from pClamp software. (b), (c) and (d) show example pulses for cancer cells, peripheral mononuclear cells and RBCs, respectively. Reprinted by permission of The Royal Society of Chemistry [179]

Table 4.2 Translocation time and amplitude for different cell types for 2o µm pore. Where *P<0.01 between CTCs and others; #P<0.01 between WBCs and RBCs. Reprinted by permission of The Royal Society of Chemistry [179]

Cells Types	Average Translocation Time	Average Peak Amplitude
CTCs	100.15 ± 75.9	5.09 + 1.51
WBCs	9.47 ± 9.08*	2.3 ± 0.45*
RBCs	6.72 ± 9.02*	1.81 ± 0.42*#

For 20 µm pore, when the flow rate was increased from 10 µL per min to 25 µL per min, only very few RBCs and WBCs were detected due to increased translocation velocity of cells as shown in Figure 4.9. It is interesting to note that renal cancer cells still gave significant current blockage pulses at higher flow rate of 25 µL per min.

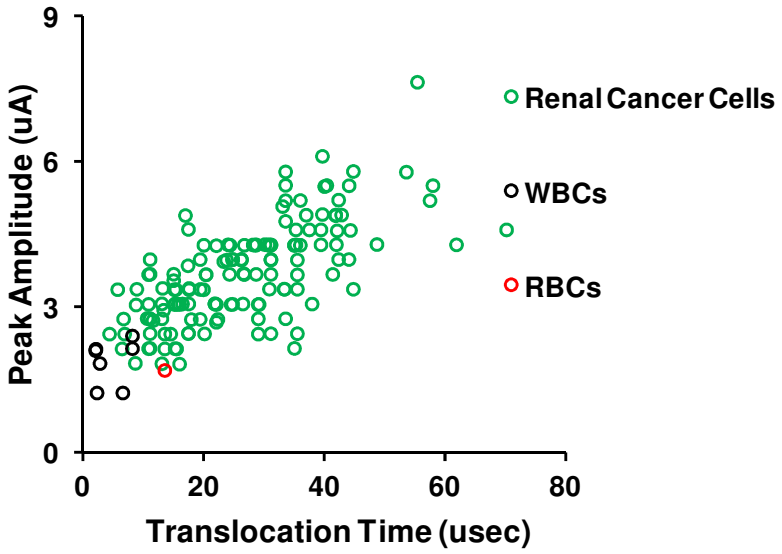

Figure 4.9 Shows the distribution of the cells data according to their size while translocating through 20 µm pore at flow rate of 25 µL per min. This data points out the distinct distribution of cancer cells from the other cell types. The average translocation times and current blockade amplitudes for renal cancer cells were significantly higher than other cells types. Only few WBCs and RBCs were detected at higher flow rate of 25 µL per min. Reprinted by permission of The Royal Society of Chemistry [179]

For further proof of the principle, we mixed the renal cancer cells with whole bovine blood. The blood was first diluted with PBS at 1:10 ratio and processed using our device. Then known concentration of cancer cells were added into the solution (100 cells/mL). The solution was mixed well before putting into the device and the measurements of cell translocation. The flow rate was maintained at 10 µL per min for both of the micropores (12 µm and 20 µm). The data was recorded using LabView software at current sampling time of 2.5 µsec and distribution density plots were made to analyze the data. Most of the cells (RBCs and WBCs) showed familiar peaks as shown in Figure 4.10. Some of the blood cells showed high current blockade signal because of clumping at higher concentration. But they can be easily separated from the renal cancer cells based on their pulse shape, width and translocation time. Cancer cells still showed smooth and deep current pulses when compared to other cell types. For 12 µm pore, about 70% of the cancer cells were detected while detection percentage was about 50% using 20 µm pore.

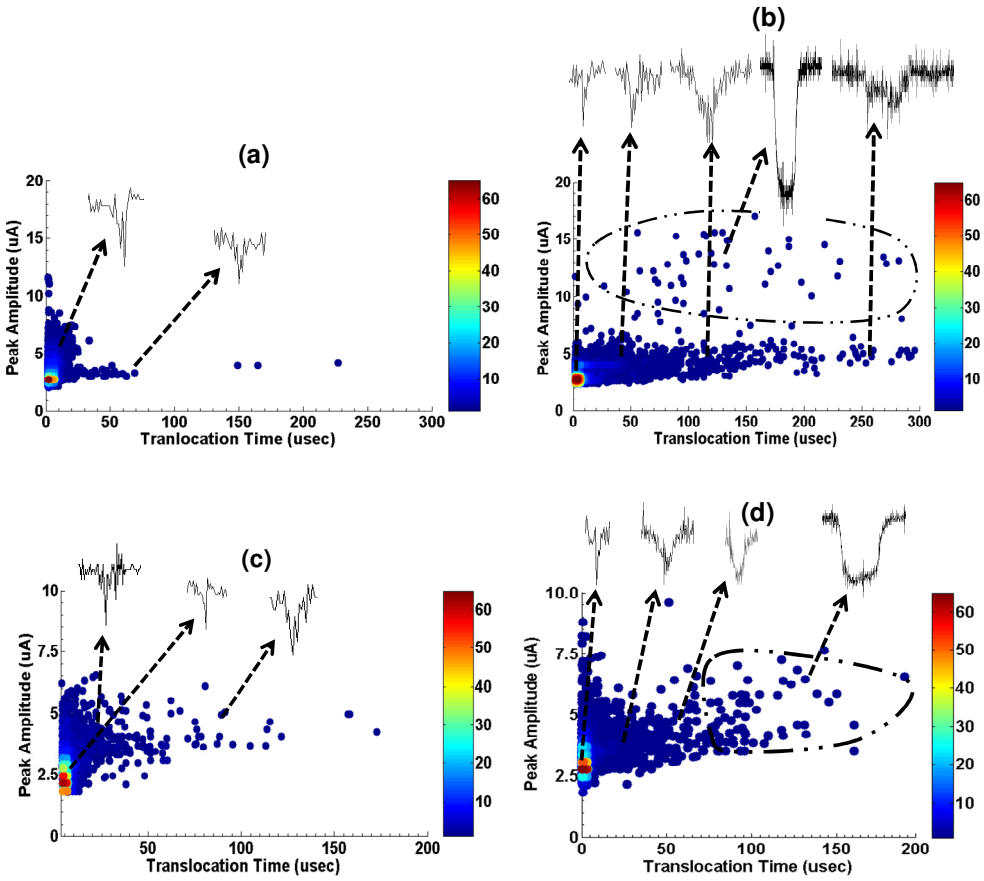

Figure 4.10 Shows the density plots for mixed cell suspensions. (a) Shows the density plot of the whole blood diluted with PBS at a ratio of 1:10 for 12 µm pore. The colormap at right of each plot shows the density distribution of cells according to their translocation time and pulse amplitude. (b) Shows the density plot when mixture of whole blood with renal cancer cells was processed using the pore chip. Because of size difference the cancer cells showed distinctive current pulses as highlighted by dashed oval. Analysis of the pulse shapes further reduced the background noise. The cancer cells gave smooth bell shaped pulses, while the other cells and clumps gave spiked pulses because of their irregular orientation. (c) Shows the density plot of diluted whole blood with PBS buffer for 20 µm pore. All the other parameters were same as for 12 µm pore. (d) Shows the density plot, when renal cancer cells were mixed with the solution of whole blood with PBS and whole mixture was process with 20 µm pore. The cancer cells can be differentiated easily form other cells based on their current pulse characteristics. Characteristic pulses were detected form the data and are shown for different data distributions. Reprinted by permission of The Royal Society of Chemistry [179]

For 20 µm pore diameter and at higher flow rate of 25 µL per min, the detection efficiency was reduced to approximately 40% as shown in Figure 4.11. At higher cell denisty, more than one cell approach the pore entrance but the pore works on first come first serve basis. When cells were translocated separately at low concentrations, they gave less translocation time when compared to mixed translocation at higher concentration. At higher flow rates of 25 µL per min, the 20 µm pore lost its detection efficiency because more than one cell would try to enter the pore at any time instance and affect the pulse characteristics. Secondly, the translocation time was reduced at flow rate of 25 µL per min which would require lesser sampling time for pulse shape discrimination.

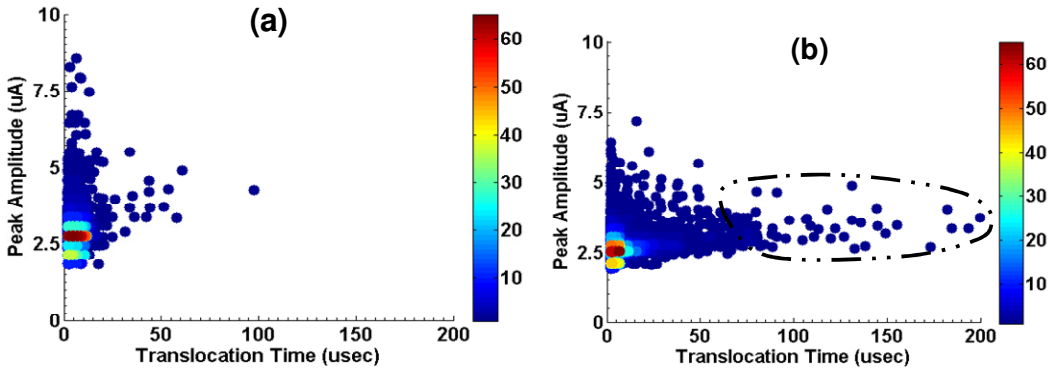

Figure 4.11 Shows the density plots for mixed cell suspension. (a) Shows the density plot of the whole blood diluted with PBS at a ratio of 1:10 for 20 µm pore. The flow rate was 25 µL per min. (b) Shows the density plot when mixture of whole blood with renal cancer cells was processed using the micropore chip of 20 µm diameter. Because of size difference the cancer cells showed distinctive current pulses as highlighted by dashed oval. At flow rate of 25 µL per min, detection efficiency was reduced to 40%, and pulse characterizing based on pulse shape became more challenging. Reprinted by permission of The Royal Society of Chemistry [179]

4.4 Conclusions

A novel solid-state micropore based cancer cell detection device was fabricated. Cancer cells can be detected directly from the whole blood using micropore device. 12 µm pore gave better cancer cell discrimination. The discrimination could be increased by diluting the blood further with PBS buffer, but more dilution would reduce the overall throughput. The cell detection approach based on size is broadly applicable and could be used for complete

phenotypic characterization of specific cells. Live and dead cells could also be differentiated by our proposed method. We successfully showed that solid-state micropore can be used for label free and efficient CTC detection from blood based on their size. Micropore device gave 85% cancer detection efficiency. Our proposed method opened a new research direction for CTC detection and characterization.

CHAPTER 5

NANOTEXTURED SCAFFOLD FROM CHICKEN EGGSHELLS

5.1 Introduction

Cell growth, adhesion, migration and orientation are influenced by surface topographical features of substrates like pores, fibers and ridges at nanometer dimensions [180, 181]. The cells shows more attachment and proliferation on textured surfaces as compared with flat ones [182, 183]. Basement membranes serve as an underlying layer for cellular structures throughout the human body. The basement membrane is composed of extracellular matrix (ECM) which has nanoporous structure with collagen fibrous network. ECM consists of fibrous collagen, proteoglycans, fibronectin, hyaluronic acid and laminin. The substrates having nano-structures, dense nanopores and high surface area have topographical resemblance with ECM and considered ideal in many tissue engineering and cell growth applications [184-186]. Therefore methods and processes to make surfaces with nano-texturing are highly desirable. The textured surfaces have also found a lot of application in biosensors, pathogen detection proteomics and light emitting diodes [22, 126, 187, 188]. Nano-textured surfaces offers increased surface area which allows more protein or nucleic acid binding to capture specific biological targets [189]. Nano-textured surfaces are prepared using photolithography, plasma etching, micro contact printing, stencil assisted patterning and long polymer chemical etching processes. These fabrication processes have limited utility because they are cost prohibitive or require special equipment [190]. Therefore a simple and cost effective fabrication process is required to make nano and micro-textured surfaces.

We report a simple and inexpensive method to make 3D nano and micro-structures using wet chemical etching of chicken eggshell. The chicken eggshell is totally resorbable and biocompatible with good osteoconductivity [191-193]. Calcium carbonate has emerged as a

novel bone substitute in its natural or derived form for bone healing applications in dentistry and orthopedics [194, 195]. Coralline eggshells have been previously reported to synthesize nanoparticles and nano-powder which can be further sintered to make porous scaffolds. However, we report that eggshells can provide novel substrate features that can be tailored for many more applications. For the first time, we report synthesis of nano-textured scaffolds by wet chemical etching of chicken eggshells. Briefly, chicken eggshells are treated with diluted hydrochloric acid (HCl) and sulphuric acid (H2SO4). The chemical treatment etches the eggshell surface into nanoporous and eggshell-grass scaffolds. The patterns are also transferred to polydimethylsilaxane (PDMS) with precision. The PDMS scaffolds are then utilized to study the effects of nano-texturing on the growth of human fibroblast cells.

5.2 Materials and Methods

All chemicals were obtained from Sigma-Aldrich (St. Louis, MO) unless otherwise noted.

5.2.1 Synthesis of Chicken Eggshell Scaffold

The chicken eggshells were first cleaned from inside by leaving them for 30 minutes in hot water followed by washing with de-ionized (DI) water. The eggshell was dried with nitrogen blow after boiling. The eggshells were processed in hot furnace at 200 ^{o}C for 2 hours to burn away any impurities. The eggshells were dipped in 15% HCl for 5 minutes for fabrication of nano-textured surfaces. The HCl-treated eggshells were washed with large amount of DI water and dried with nitrogen. In order to make micro-needle scaffolds, the eggshells were left in 25% H_2SO_4 for half an hour. The H_2SO_4-treated eggshells were also washed with a conspicuous amount of DI water and dried with nitrogen blow. After drying, scaffolds were stored in Petri dishes for later use.

5.2.2 Gold Sputtering for SEM Imaging

As scanning electron microspore (SEM) imaging requires conductive samples, we sputtered 10 nm thin film of gold on eggshell samples to make these conductive for imaging. The SEM (ZEISS Supra 55) was used in Variable Pressure mode. Secondary electron (SE) detector at high vacuum was used during SEM imaging.

5.2.3 Energy-Dispersive X-ray Spectroscopy (EDS) and Composition Mapping

Energy-Dispersive X-ray Spectroscopy (EDS) was used for elemental analysis of synthesized eggshell scaffolds. EDS and mapping was done before gold coating. EDS detector (EDAX, Genesis) was attached to SEM. After loading the sample, SEM was focused at 15 mm working distance with 15 KV applied voltage. First EDS data was captured and then mapping analysis was done using inbuilt mapping software.

5.2.4 X-ray Diffraction Analysis for Chicken Eggshell Samples

First eggshell samples were loaded into sample holders using molding clay. The X-ray system (KristalloFlex-810, Siemens D-500) was turned on and allowed to warm up for 10 minutes. The sample was loaded and X-ray beam was turned on. X-ray diffraction data was captured at the following conditions: $2\theta\_start = 8^{o}$, $2\theta\_end = 120^{o}$, step size = 0.05 and dwell time = 3 secs.

5.2.5 Polydimethysiloxane Casting

The eggshell samples were treated with 1H,1H,2H,2H-Perfluorooctyl-trichlorosilane (PFTS). Deposition of thin film of PFTS helped in peeling off of polydimethysiloxane (PDMS: Sylgard 184, Dow Corning) from eggshell samples [196]. For PFTS deposition, the eggshell samples were put on the hot plate next to a glass slide that carried few drops of PFTS. These were covered with glass Petri dish with small hole in it. The temperature of the hot plate was maintained at 250 ^{o}C. The PFTS evaporated at high temperature and get deposited on the eggshells scaffolds making few nm polymer layer [197]. The eggshells scaffolds were removed

from the hot plate after 20 minutes and allowed to cool down. PDMS was prepared by mixing base curing agent at the ratio of 1:10 (w/w). PDMS mixture was placed in vacuum chamber to remove air bubbles. PDMS mixture was then poured on the eggshell scaffolds and allowed to polymerize for 10 minutes at 150 ^{o}C. The samples were cooled down and PDMS was peeled off the eggshell scaffolds.

5.2.6 Atomic Force Microscope (AFM) Surface Analysis

AFM was used for surface analysis of PDMS scaffolds casted from textured eggshell surfaces. Non-contact AFM tips (NCLR f^{o}: 190 kHz, C: 48 N/m, NanoWorld AG) were used to analyze the PDMS surface. No coating was applied on samples prepared for AFM analysis.

5.2.7 Human-derived Primary Immortalized Fibroblast Cell Culture

Human fibroblast cells were obtained from consenting patients at the University of Texas Southwestern Medical Center (Dallas, TX, USA) with the approval of the Institutional Review Board. The collected human fibroblast cells were cultured in Dulbecco's modified Eagle's medium (DMEM/F-12, Cellgro, Mediatech Inc.) with 10% fetal bovine serum. Gentamycin and L-Glutamine (Invitrogen) were also added in cell culture medium. Cells were incubated under standard cell culture conditions i.e. a sterile, humidified, 95% air, 5% CO2 and 37 ^{o}C.

5.2.8 In vitro Fibroblast Cell Culture Studies and Laminin Coating on PDMS Scaffolds

Texture and plain PDMS scaffolds were cut into 6 mm diameter circular disks. All the PDMS samples were glued into 24 well plate using UV glue (Dymax Corporation). The well plate was left under UV lamp for 20-30 mins to cure the UV glue. All the PDMS scaffolds were washed three times with DI water and dried with nitrogen blow. The PDMS samples were treated with O_2 plasma for 30 minutes to sterilize the scaffolds. Secondly, the plasma treatment made the surface of PDMS hydrophilic. All of the scaffolds were washed again with DI water 3 times. The samples were then coated with Poly-D-Lysine (PDL) by immersing the scaffolds in PDL solution for 24 hours. PDL solution was made in DI water. The PDL solution was drained

out after 24 hours and the wells were filled with DI water. The wells were washed again thoroughly with sterilized DI water for 3 times. PDMS samples were then coated with laminin by immersing the samples in solution with 10 µg/ml laminin in 1X PBS solution. Well plate was left at 37 ^{o}C in incubator for 3-4 hours to coat laminin on PDMS surfaces [198]. The laminin solution was then removed and samples were washed with sterilized 1X PBS thrice. Freshly harvested human fibroblasts cells were seeded onto the PDMS samples; 5000 cells/cm^2 for low density and 100,000 cells/cm^2 for high density cell culture studies. Four samples were prepared for each condition (n=4). Statistical Analysis was performed using one-way ANOVA analysis for three independent samples.

5.2.9 Immunostaining of Human Fibroblast Cells

After cell culture for 3 days, the cell culture medium was removed from the wells. The cells were fixed by immersing all the samples into 4% paraformaldehyde for 3 hours. Blocking solution was prepared by mixing goat serum with washing solution (0.5 % Triton X-100 in 1X PBS solution) to make 4% goat serum. 4% paraformaldehyde was removed after 3 hours followed by washing three times with 1X PBS. Blocking solution was added on samples for 1 hour at room temperature. Blocking solution was replaced with primary antibody solution (Vimentin, mIgG1, 1:500) and well plate was left overnight at 4 ^{o}C. After specific time period, primary antibody solution was removed and all the PDMS samples were washed 3 times with washing solution. Secondary antibody solution was prepared by mixing goat anti-mouse IgG1 Dylight 488 (1:400, Jackson ImmunoResearch Laboratories Inc., USA) with washing solution. Secondary antibody solution was added to all wells and samples were left for 1 hour at room temperature. Samples were washed again three times with washing solution. Samples were left with 1X PBS. All the samples were imaged with the same fluorescent microscope.

5.2.10 Laminin Staining

The method to stain for laminin was similar to immunostaining process used for fibroblast except different primary and secondary antibodies were used. Laminin was fixed by immersing samples in 4% paraformaldehyde. Primary laminin antibody (rabbit IgG, 1:200) solution was added to all of the wells and kept at 4 ^{o}C overnight. After desired time, primary was removed and secondary antibody solution, goat anti-rabbit IgG Dylight 488 (1:400, Jackson ImmunoResearch Laboratories Inc.), was added and well plate was kept at room temperature for 1 hour. Samples were washed with washing buffer three times followed by immersion in 1X PBS solution. Four images were taken for each sample from random parts using fluorescent microscope. The intensity data was measured and quantified with *ImageJ* software. The intensities were calculated by selecting random areas of the images. Bright spots were avoided during intensity quantification. Statistical Analysis was performed using one-way ANOVA analysis for three independent samples.

5.2.11 Cell Sample Preparation for SEM Imaging

In order to prepare the cell samples for SEM imaging, different ethanol gradient solutions (v/v) were prepared by mixing with DI water at concentrations of 20%, 30%, 50%, 70%, 85%, 95% and 100% [189]. The gradient solutions were used to remove water content from the cells. The ethanol gradient solutions helped cells to be fixed without rupturing the cell walls. All the samples were put in each ethanol gradient solution for 15 minutes in increasing concentration order (starting with 20%). Samples were stored at -20 ^{o}C for overnight. Fixed cell samples were prepared for SEM imaging by sputtering few nm of gold onto all samples.

5.3 Results and Discussions

5.3.1 Wet Etching of Chicken Eggshells

The eggshell samples were cleaned as explained in materials and method section. When the samples were treated with diluted HCl and H_2SO_4, different nano-textures were produced on

the eggshell surface. Chemically treated eggshell samples had nano-features and micro-needles as shown by SEM micrographs in Figure 5.1. SEM micrographs showed that original eggshell does not have any of the features like micro-features or nanoporous texture.

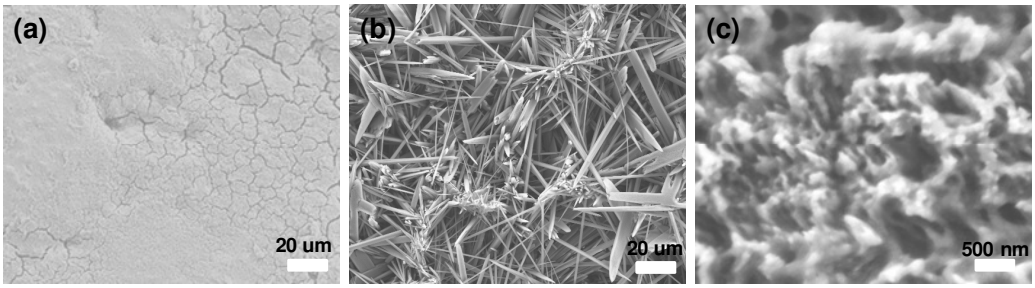

Figure 5.1 Shows the SEM micrographs for original and chemically treated eggshell surfaces. (a) Original eggshell surface. (b) Eggshell treated with 25% H_2SO_4 solution for 30 minutes. (c) Eggshell treated with 15% HCl solution for 5 minutes

H_2SO_4-treated eggshell scaffolds showed needles with widths ranging between 500 nm – 3 µm and the lengths of most of the needles are 50 µm as shown in Figure 5.2. Eggshell micro-needles are similar to silicon grass in shape [25, 26]. The concentration of sulfuric acid did not have any effect on the size, shape, orientation, thickness or length of the micro-needles. We found that higher the concentration of sulfuric, higher would be the rate of chemical reaction but it did not have any effect on synthesized micro-needles.

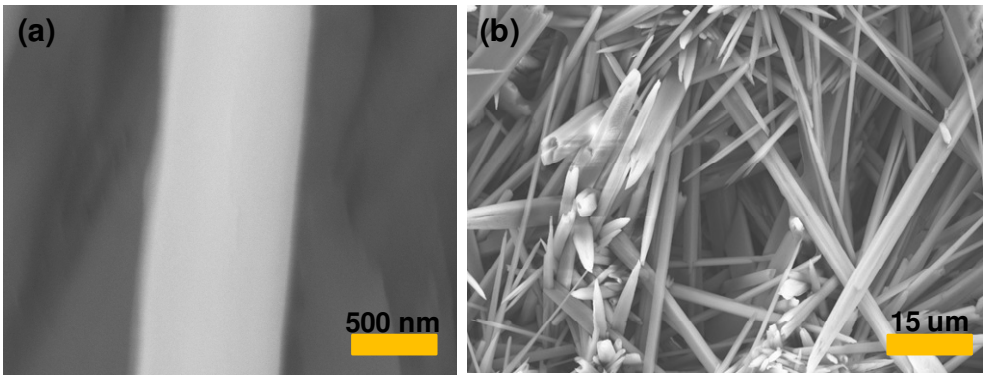

Figure 5.2 Shows the SEM micrographs of micro-needles synthesized by the chemical reaction of eggshell with sulfuric acid. (a) Shows single micro-needle with width of ~800 nm. (b) The lengths of micro-needles ranged between 25–60 µm

Nanoporous texture was formed on the surface of eggshell treated with diluted HCl. The average diameter of nanopore was less than 100 nm as shown in Figure 5.3. The nanoporous pattern was very uniform over the whole eggshell surface. We used higher concentrations of HCl (25 %, 50%) but, again, it showed only increase in the chemical reaction with no differences in the final nano-texture. At higher concentrations of HCl, it was difficult to control the chemical reaction. The HCl reacted vigorously with chicken eggshell at higher concentrations.

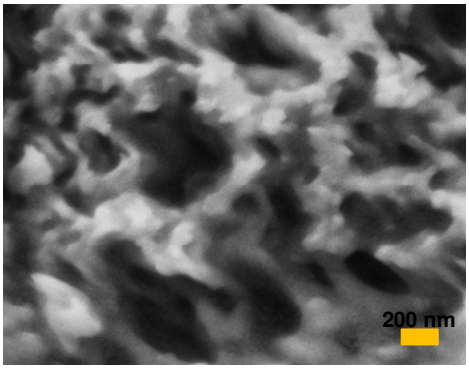

Figure 5.3 Shows SEM micrograph of the eggshell treated with HCl. The diameter of most of the nanopores is less than ~100 nm

5.3.2 EDS Elemental Analysis and Mapping of Eggshell

Energy-dispersive x-ray spectroscopy (EDS) was performed to analyze the material composition as described in Materials and Method section. The original chicken eggshell mainly consisted of Ca, C, O, P and Mg as shown in Figure 5.4(a). EDS spectrum analysis showed that carbon content decreased significantly in H_2SO_4 treated sample as carbon would form CO_2 during chemical reaction Figure 5.4(b). Chemical reaction might also have dissolved some organic impurities. The sulfuric acid treatment decreased the carbon content and sulfur content was appeared as shown by Equation 5.1.

$$CaCO_3 + H_2SO_4 \rightarrow CaSO_4 + H_2O + CO_2 \qquad (5.1)$$

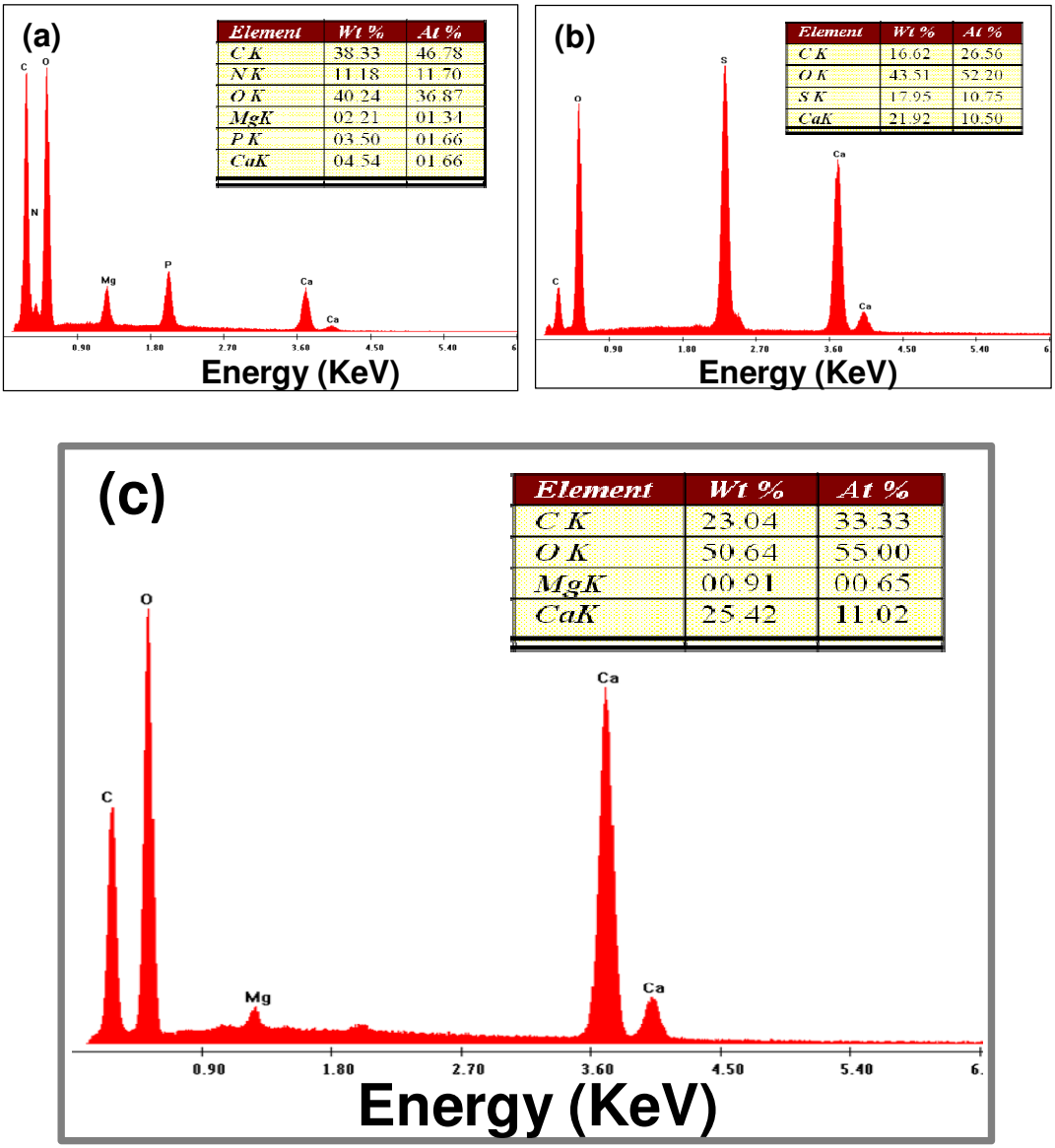

Figure 5.4 EDS elemental analysis of original and chemically treated eggshell samples. (a) EDS spectrum of original eggshell. (b) EDS spectrum of eggshell sample treated with diluted H_2SO_4. (c) EDS spectrum of eggshell sample treated with diluted HCl

Chicken eggshell mainly consists of 94% calcium carbonate, 1% calcium phosphate, 4% organic matter and 1% magnesium carbonate [199]. When calcium carbonate reacted with sulphuric acid, grass like features were produced which were supposed to be made up of calcium sulphate. The composition mapping was performed on the H_2SO_4 treated sample as

explained in materials and methods section and also shown in Figure 5.5. Mapping of eggshell samples treated with sulfuric acid proved that calcium was abundantly present all over the sample but oxygen and sulfur were mainly present on the surface of micro-needles. It was due to the fact that the original eggshell is composed of calcium carbonate which has calcium everywhere. As sulfur was only present over the needle surface, that confirmed the formation of calcium sulphate crystals. The presence of carbon in few areas might be due to underlying calcium carbonate which was still in its original form.

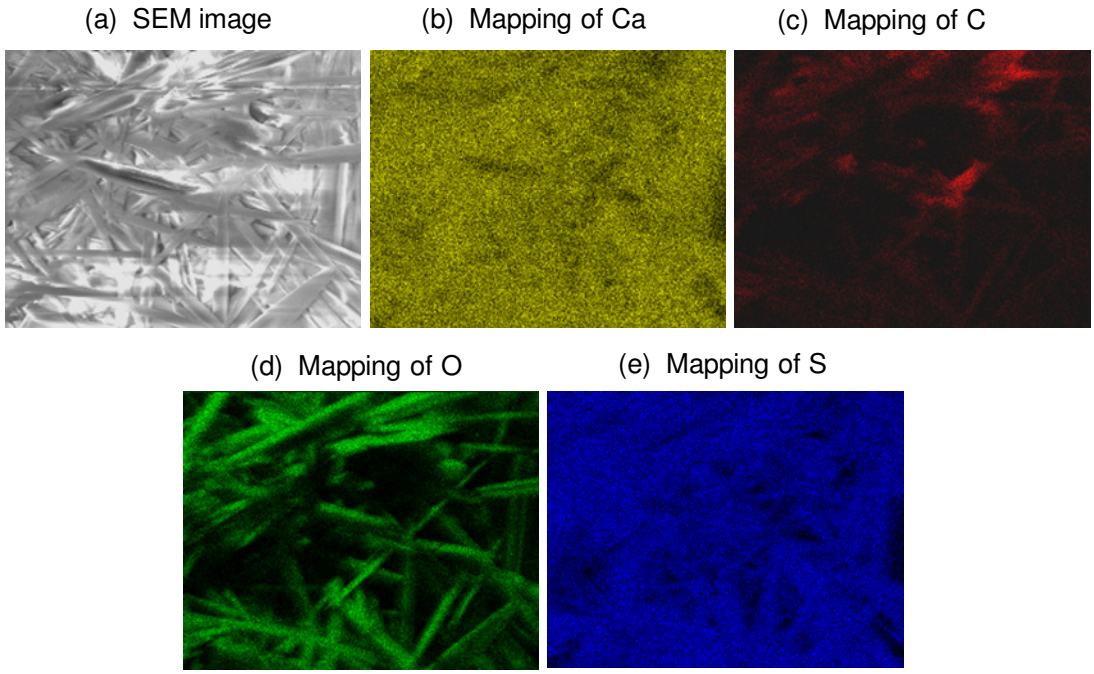

Figure 5.5 Elemental mapping of sulfuric acid treated eggshell samples. (a) SEM micrographs of the sample area used for mapping. Mapping micrographs show: (b) Mapping of calcium; (c) Mapping of carbon; (d) Mapping of oxygen; (e) Mapping of sulfur

Carbon content was reduced when eggshell reacted with diluted HCl solution as shown in Figure 5.4(b). Lesser carbon content was due to the release of CO_2 and dissolution of organic components during chemical reaction. Chlorine was not found in the EDS spectrum, because $CaCl_2$ precipitated out in the solution. The reaction equation of eggshell with HCl is given by Equation 5.2.

$$CaCO_3 + 2HCl \rightarrow CaCl_2 + H_2O + CO_2 \quad (5.2)$$

The formation of the nano-features on the eggshell surface was due to random etching of the eggshell surface. When eggshell was reacted with HCL, CO_2 was being released resulting bubble formation. The bubbles prevented the physical contact of certain areas of the eggshell surface with HCl for short duration of time. This bubble formation process resulted into an uneven chemical etching of the eggshell surface which led the appearance of nano-features on eggshell surface.

5.3.3 XRD Crystal Analysis of Eggshell

The eggshell samples were also characterized with XRD as shown in Figure 5.6. After recording the XRD data, *Jade5* software was used to analyze the results. It was found that original eggshells showed a significant peak around $2\theta \sim 30^o$ which was characteristic of crystalline calcite having *hkl* (104) [200]. These results were similar to previous reports [201]. The XRD spectrum of H_2SO_4 treated eggshell showed that there were few peaks which were not associated with calcite as denoted by stars in Figure 5.6(a). These peaks were associated with calcium sulphate dihydrate (CSD) crystals [202]. The three peaks ($2\theta \sim 12^o$, 20^o and 24^o) are similar as reported earlier reports [202]. The overlapping of two XRD spectra in certain regions might be due to the fact that calcite phase was still present in underlying layers of eggshell. The sample treated with HCl showed XRD spectrum very similar to original eggshell as shown in Figure 5.6(b). The XRD spectra of both of the samples perfectly overlapped with significant peak around $2\theta \sim 30^o$ (calcite crystalline phase). The HCl has just etched the eggshell surface but did not change the surface composition. It can also be confirmed by EDS analysis.

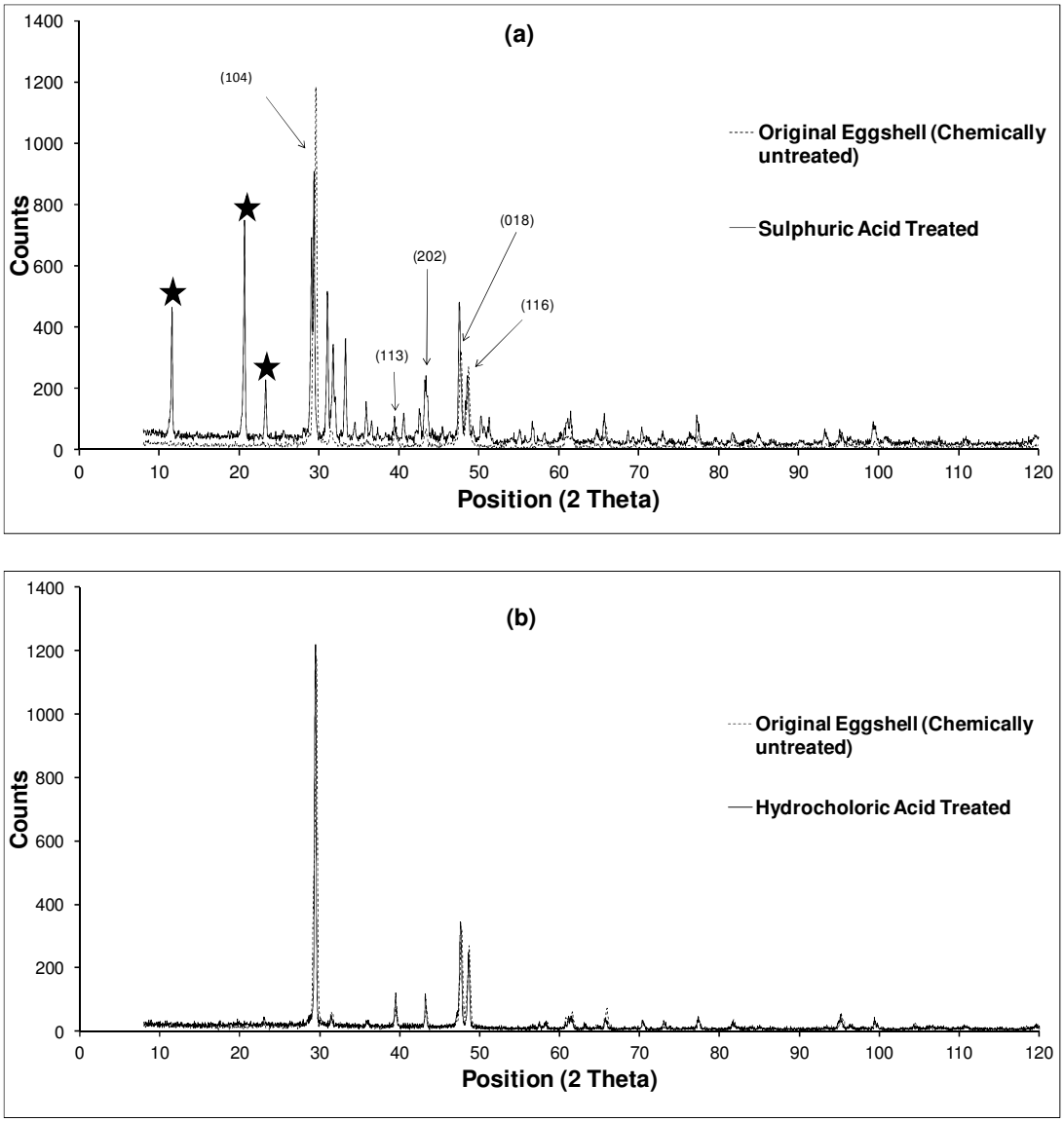

Figure 5.6 X-ray diffraction spectra for original and chemically treated eggshell samples. (a) Comparison between XRD spectra of original eggshell and H_2SO_4 treated eggshell. The peaks represented by arrows show the characteristics of crystalline calcite phase having *hkl* (104), (113), (202), (018) and (116). Stars represent the peaks not associated with calcites. (b) Comparison between XRD spectra of original eggshell and HCl treated eggshell

5.3.4 Polymer Casting and AFM Analysis

PDMS was casted onto the chemically treated eggshells as explained in the materials and methods section. A nanolayer of 1H,1H,2H,2H-Perfluorooctyl-trichlorosilane (PFTS)

polymer was deposited before casting PDMS, as PFTS helped in peeling PDMS off of the eggshell surface. Three different samples were synthesized i.e. PDMS casted from plain surface (Sample-1), PDMS casted from eggshell with micro-needles (Sample-2) and PDMS casted from eggshells with nano-texture (Sample-3). For convenience we will use Sample-1 (plain control), Sample-2 (casted from H_2SO_4 treated eggshell) and Sample-3 (casted from HCl treated eggshell) in the remaining text. After casting, PDMS samples were analyzed using atomic force microscope (AFM). The AFM micrographs showed that Sample-2 showed both micro and nano-features while Sample-3 had only nano-texture as shown in Figure 5.7. For Sample-2, the micro-features were transferred from the micro-needles. As micro-needles were very dense, there were nano-gaps present between the micro-needles which resulted in the formations of nano-features on the PDMS Sample-2.

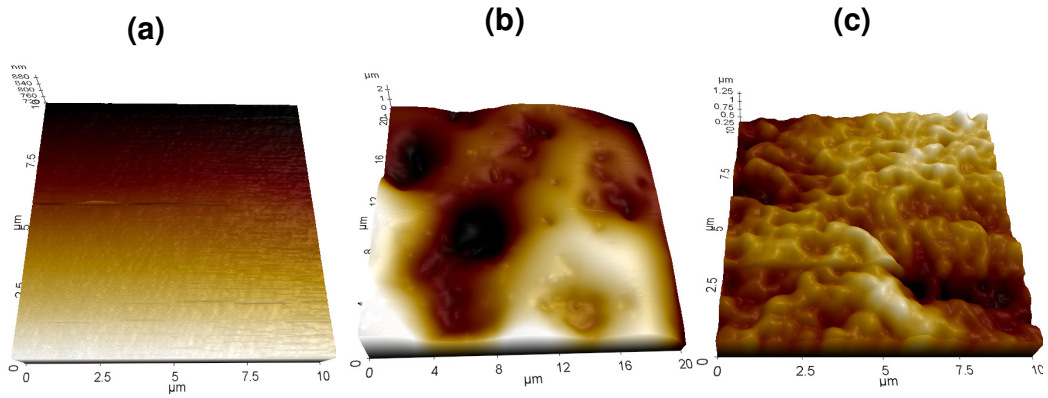

Figure 5.7 Shows AFM micrographs of PDMS samples casted form native and processed eggshells. (a) Sample-1, PDMS casted on plain glass surface. (b) Sample-2, PDMS casted on eggshell with micro-needles. (c) Sample-3, PDMS casted from eggshell with nano-texture

The samples were also analyzed by SEM as shown in Figure 5.8. SEM micrographs clearly revealed that PDMS Sample-2 had both of the micro and nano-features. Very uniform nano-texture was found on the surface of PDMS Sample-3 which casted from eggshell treated with HCL.

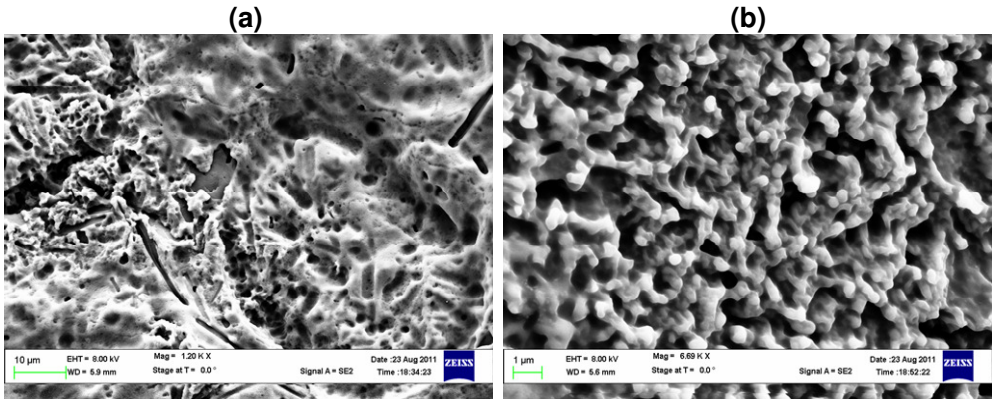

Figure 5.8 Shows SEM micrographs of PDMS samples. (a) Sample-2 with nano to micron range features. (b) Sample-3 with nano-texture

5.3.5 Laminin Coating on PDMS Samples

To study the *in vitro* fibroblast cell growth on different surfaces, first human fibroblast cells were seeded onto the PDMS samples without laminin coating. The cells were allowed to grow on PDMS surfaces for 3 days. It was observed that cells were not growing well on the PDMS surfaces without laminin coating. The intrinsic hydrophobicity of PDMS did not allow cells to attach and grow well. Cells like moderately hydrophilic surfaces. Cell membrane proteins are highly absorbable on moderate hydrophilic surface which facilitates cell adhesion. It is also interesting to point out that highly hydrophilic surfaces also prevent protein adsorption. The flat PDMS surface is very hydrophobic because methyl group is present on both sides of backbone chain with average contact angle of ~115±2^{o}. It is interesting to note that hydrophobic surfaces become more hydrophobic with nano-texturing, while hydrophilic surfaces become more hydrophilic with nano-texturing [189]. In this regards, nano-texturing would not help in reducing the contact angle of hydrophobic PDMS surface. The PDMS samples were made hydrophilic by laminin coating as described in material and methods section [198]. Fluorescent imaging was used to verify the laminin attachment. Fluorescent intensity was quantified on all of the laminin coated PDMS samples as shown in Figure 5.9.

Fluorescent intensity quantification showed that the laminin attachment on Sample-3 was 2 times more than Sample-1 because it had more surface area available for attachment. There was also ~50% more protein attachment on the nano-textured PDMS surface (Sample-3) as compared to mciro-textured PDMS (Sample-2). Statistical analysis showed that there were significant statistical differences between Sample-1, Sample-2 and Sample-3 (*P*-value < 0.0001, n=4).

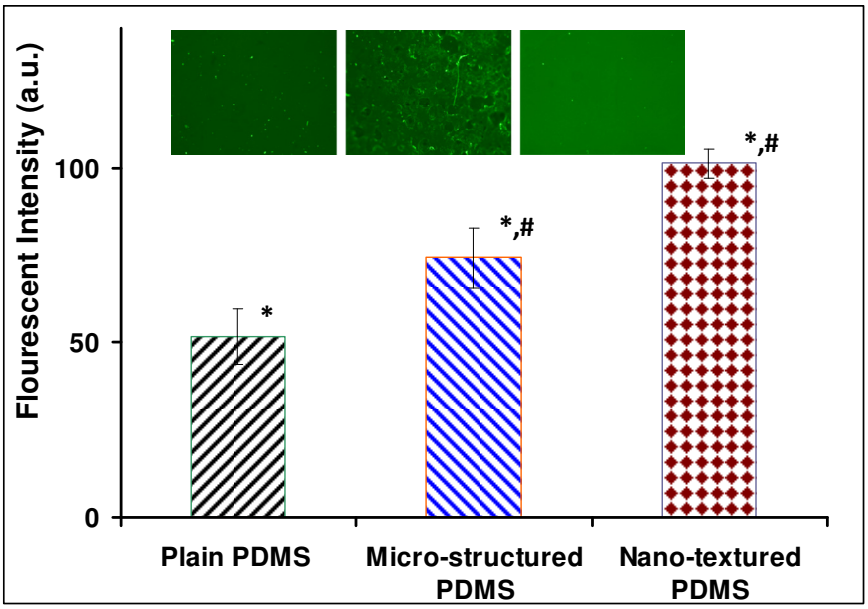

Figure 5.9 Shows fluorescent intensity (a.u.) after laminin coating of PDMS samples. There were significant statistical differences between flat and textured PDMS samples (*p <0.0001, n=4). Nano-textured PDMS samples were also statistically different from micro-structured PDMS samples (#p <0.0001, n=4)

5.3.6 In vitro Fibroblast Cell Growth

Human fibroblast cells were seeded on the all three types of laminin coated PDMS samples. The cell growth was found to be significantly more on laminin coated textured Sample-2 and Sample-3 as compared to laminin coated plain Sample-1 as shown in Figure 5.10. The cell density increased from 63±14 cells/mm^2 (Sample-1) to 810±207 cells/mm^2 (Sample-2) and

1035±130 cells/mm^2 (Sample-3) as shown in Figure 5.11. The PDMS samples casted from HCl treated eggshell showed denser and more uniform fibroblast growth compared to other PDMS samples. Statistical analysis showed that there were statistically significant differences (*P*-value < 0.01) between Sample-1, Sample-2 and Sample-3. Though Sample-3 had more cell density than Sample-2 but they were not significantly statistically different (*P*-value = 0.1236). It was also observed that if the initial cell seeding density was increased from 4000 cells/cm^2 to 100,000 cells/cm^2, there were very little affects of nano-texturing on cell growth. The cells aslo proliferated well on Sample-1 but there were lesser in number. Similar initial cell seeding number affect on MDCK epithelial cell growth has been reported earlier [203]. For dense cell culture studies, cell-cell contact might have resulted in increased mechanical forces between cells [198]. The decrease in topographical effects on the cell growth might have resulted from these mechanical forces.

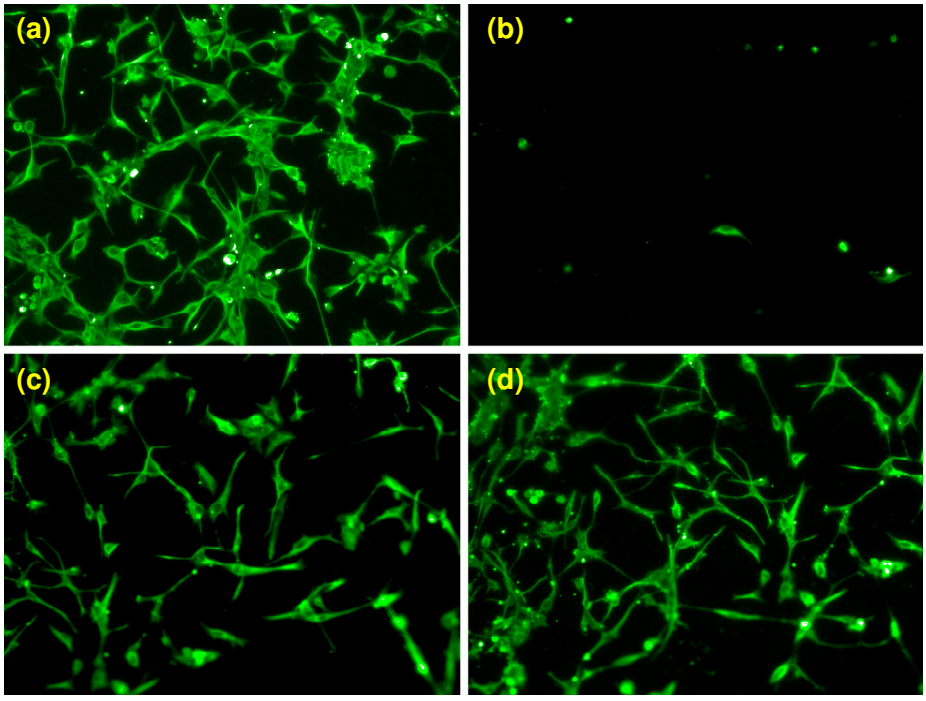

Figure 5.10 hows fluorescently labeled human fibroblasts on different PDMS surface types. (a) Fibroblast growth on cell culture. (b) Fibroblast growth on flat PDMS, Sample-1. (c) Fibroblast growth on Sample-2. (d) Fibroblast growth on Sample-3. Human fibroblast cells were cultured for 3 days before fluorescent imaging

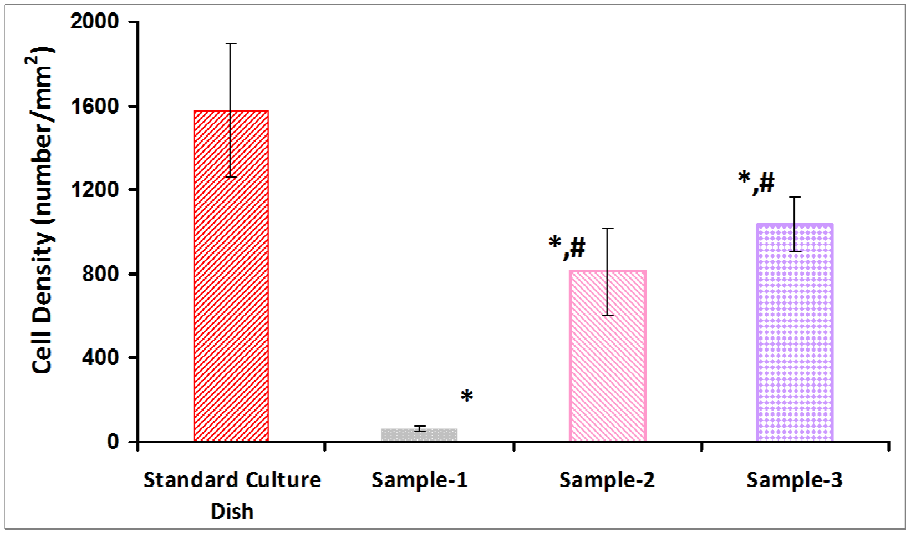

Figure 5.11 Shows human fibroblast growth density on all three types of PDMS samples. The cells were imaged and counted after 3 days of cell growth. There was significant statistical differences between Sample-1 and other samples (*p <0.01, n=4), while Sample-2 and Sample-3 were not statistically significant different (#p = 0.12, n=4)

5.3.7 Cell Morphology on Flat and Nano-textured PDMS

SEM imaging was used to characterize the cell morphology on PDMS surfaces. Visual differences in cell morphology were seen on flat and nano-textured PDMS surfaces. The cell shape on flat PDMS surface was spherical as shown in Figure 5.12, while cells on the nano-textured surfaces were elongated and well-spread. We believe that nano-texturing helps cells to better attach on the surface which resulted in more cell growth. SEM micrographs showed that fibroblast cells were ~100 µm elongated on nano-textured PDMS surface while cells on plain PDMS were just 30 µm in size. We show that nano-texturing plays a very important role in protein adsorption, cell adhesion, growth and proliferation. The nano-textured surfaces have increased surface area which allowed more of the protein attachment and hence helped cell adhesion and growth.

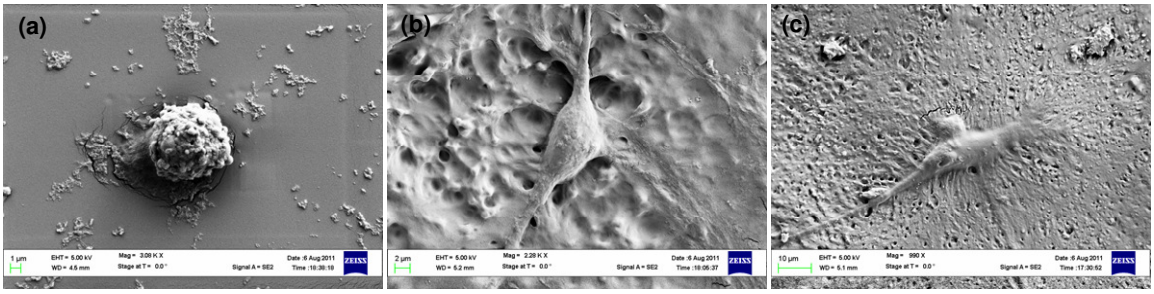

Figure 5.12 Shows SEM micrographs showing human fibroblast morphology on all types of PDMS surfaces. (a) Fibroblast morphology on flat PDMS sample (spherical). (b) Fibroblast morphology on PDMS Sample-2 (elongated). (c) Fibroblast morphology on PDMS Sample-3 (elongated and spread out)

5.4 Conclusions

The reported nano-texture synthesis method is simple, rapid and cost-effective. As these micro and nano-scale structures are synthesized from chicken eggshells, it opens a new way to create nano-textured surfaces while recycling common waste. The unique micro-needle pattern resembles silicon grass which has been used for different applications including cell culture studies. The patterns can be successfully transferred to many polymers as demonstrated in case of PDMS. The casted nano-textured PDMS shows more protein attachment due to increased surface area. The cells growth rate is also increased on these surfaces as compared to flat ones that show the power of these novel substrates that can significantly enhance cell culture studies.

CHAPTER 6

RAPID NANO-MANUFACTURING OF BREAK-JUNCTIONS USING FOCUSED ION BEAM (FIB) AND ELECTROMIGRATION

6.1 Introduction

Break-junctions are one of the simplest ways to study the current flow in molecules [204]. It consists of a thin metal strip in which a gap is formed by one of the many possible ways. The gap that is formed is usually in the nano or sub-nanometer range. The break in the metal strip can be caused by a variety of methods including e-beam lithography, electromigration, with mechanical control, electrochemical deposition [135], etc. The majority of the approaches uses either serial e-beam writing of metal electrodes or suffers from low-yield. Break-junctions have also been synthesized using scanning tunneling microscope tips, where molecules bridge the tip and substrate surface [205]. The tunneling microscope process is also not scalable because each individual molecule has to get attached between the tip and substrate.

Herein, we present a novel approach of using focused ion beam (FIB) scratch followed by conventional electromigration to create break-junctions at precise locations. Electromigration is a break-down phenomenon where application of voltage and current that flows results into a “break” in the metal line. The reported process gave higher yield. We believe that a break-junction with larger distance (~200 nm) having very small conductance between electrodes is more favorable for applications in molecular sensing. The lower conductance of break-junction can show more pronounced change when an analyte binds to surface-attached probes in-between the electrodes.

6.2 Materials and Methods

The fabrication of metallic break-junctions started with the oxidation of silicon wafer followed by two-step photolithography process. In the first step of photolithography, a 3 μm wide line pattern was defined followed by e-beam evaporation of 50 Å of titanium. The titanium coating was used as an adhesion layer. The process continued with the evaporation of 150 Å of gold. Lift-off was performed to have metal lines on the wafer. In the second step of photolithography, probing pads were patterned that were aligned to the metal lines. The probing pads were made of 100 Å titanium and 500 Å gold.

The FIB has been used in many applications in nano and micro-scale fabrication. FIB has also been used extensively in MEMS for micromachining and ion milling [206, 207]. In this report we used a manual FIB milling process on gold lines to make a scratch on the surface. A 30 kV acceleration voltage was used for the FIB scratching using Gallium ions. Different milling currents (100 pA, 20 pA and 1 pA) and FIB scratching times (120 sec and 60 sec) were used to achieve optimum conditions. A number of characterization runs were carried out to ensure that FIB does not remove all of the metal line during scratching. This characterization was very critical because if FIB scratching would remove all of the metal, it might also affect the underlying oxide. The underlying oxide would be further used for surface functionalization.

FIB drilling has been used previously to create surface defects in a pattern for selective and controlled electrochemical deposition of metals [208]. We believe that this presented work is the first report of using FIB based partial scratching of the metal lines to create controlled nano-gaps for break-junction fabrication. The innovation and opportunity lies in using the conventional photolithography to define pattern and then using FIB process to make scratches rather than patterning the whole line using e-beam writing. The reported process also did not require e-beam alignment marks during fabrication process.

The Agilent *I-V* probe station was used to measure current-voltage (*I-V*) characteristics across the metal lines. Sweeping voltage was applied and current flow was measured. The *I-V*

measurements were done before and after the FIB scratch, and again before and after the creation of break-junction with electromigration.

6.3 Results and Discussions

First the line was patterned using optical photolithography on the chip surface as shown in Figure 6.1. The whole process is explained in the materials and methods section.

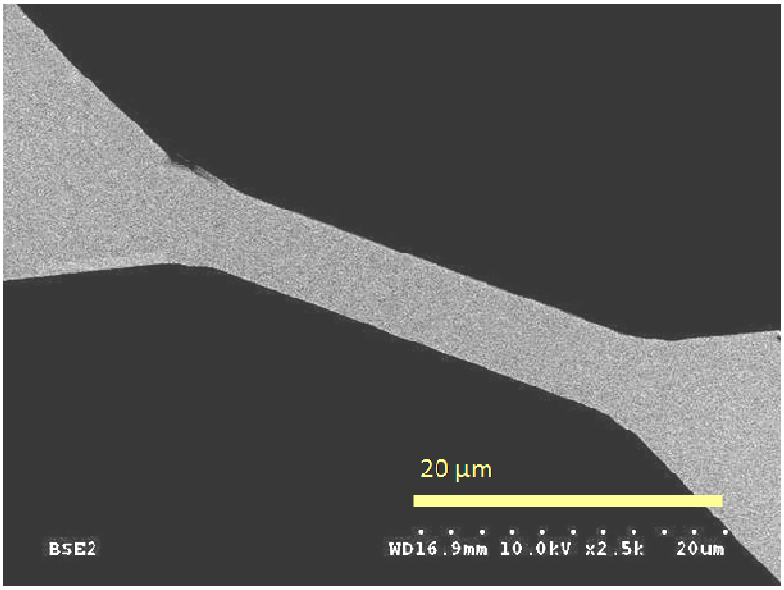

Figure 6.1 Shows the SEM micrograph of the gold lines as patterned with optical photolithography. Reprinted with permission [209]

FIB scratching was performed on the chip after metallic lines are patterned. Figure 6.2 showed different FIB conditions that resulted in scratching of the gold lines. The amount of material removed from the metal lines was directly proportional to the milling current and time of the FIB scratching process. A longer FIB exposure with higher milling current resulted in complete removal of the metal as shown in Figure 6.2(a). Lesser milling current resulted in removal of relatively less metal but long exposure time (120 sec) still resulted in a wide trench as shown by Figure 6.2(b). Decreasing the exposure time to 60 sec and milling current to 1 pA

provided the optimum removal of material as shown by Figure 6.2(c). All of the devices were processed at these conditions.

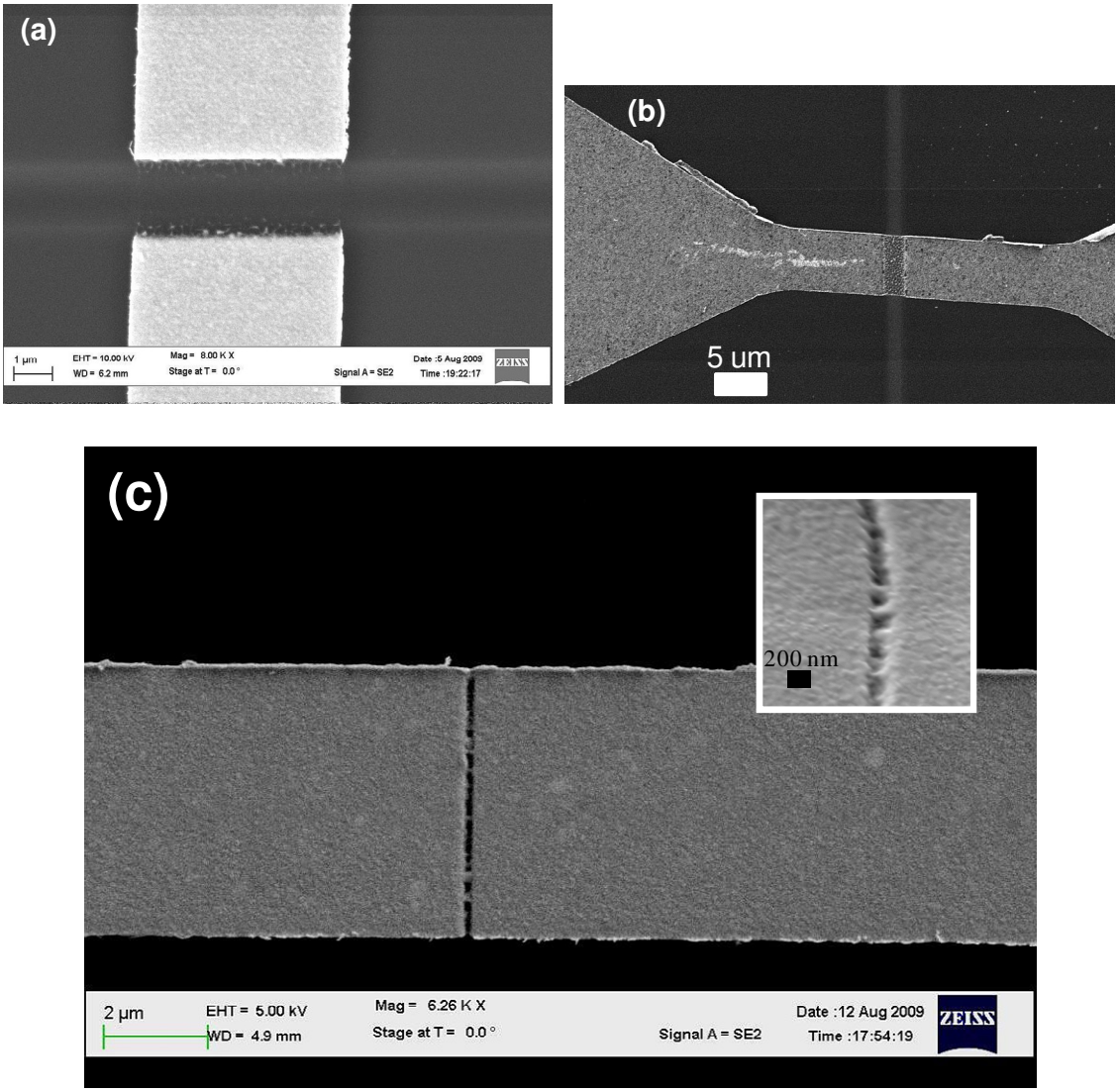

Figure 6.2 Shows the SEM micrographs for FIB scratches at different accelerating voltages, milling currents and time of scracthing exposure; (a) 30 kV, 100 pA, 120 sec (b) 30 kV, 20 pA, 120 sec, and (c) 30 kV, 1 pA, 60 sec. Magnified view of scratch is shown in inset of (c). Reprinted with permission [209]

The *I-V* data was recorded using probe station after FIB scratch of metal lines. All devices showed a linear *I-V* trend proving the electrical and physical continuity of the metal lines

as shown by Figure 6.3. To break the metal lines at specific location, electromigration voltage sweep (0 to ~5 V) was applied. The drop in recorded current showed the complete break in the metal line (Inset to Figure 6.3). The complete breaking of metal lines is shown by Figure 6.4. The *I-V* data was compared before and after the application of the electromigration as shown in Figure 6.5. Once the junctions are completely broken, the current flow became negligible.

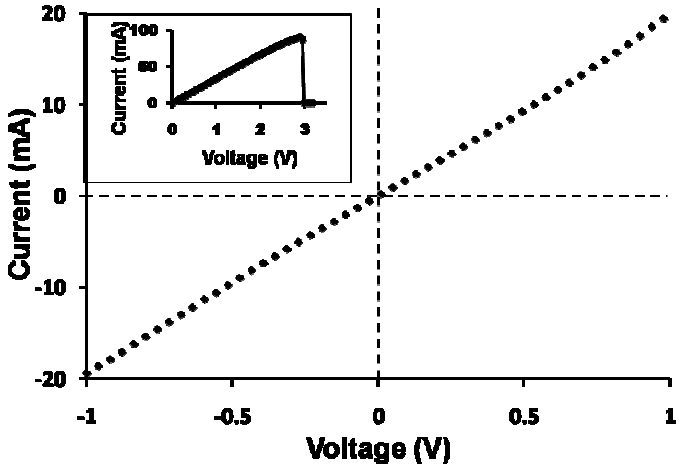

Figure 6.3 Shows the *I-V* data of metal lines after the FIB scratch. Inset shows the sudden drop in current through metal line describing the complete break of the metal. Reprinted with permission [209]

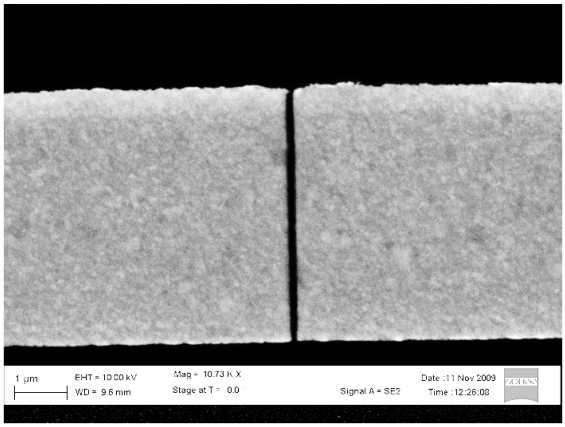

Figure 6.4 Shows the SEM micrograph with the nano-gap between metallic line. Reprinted with permission [209]

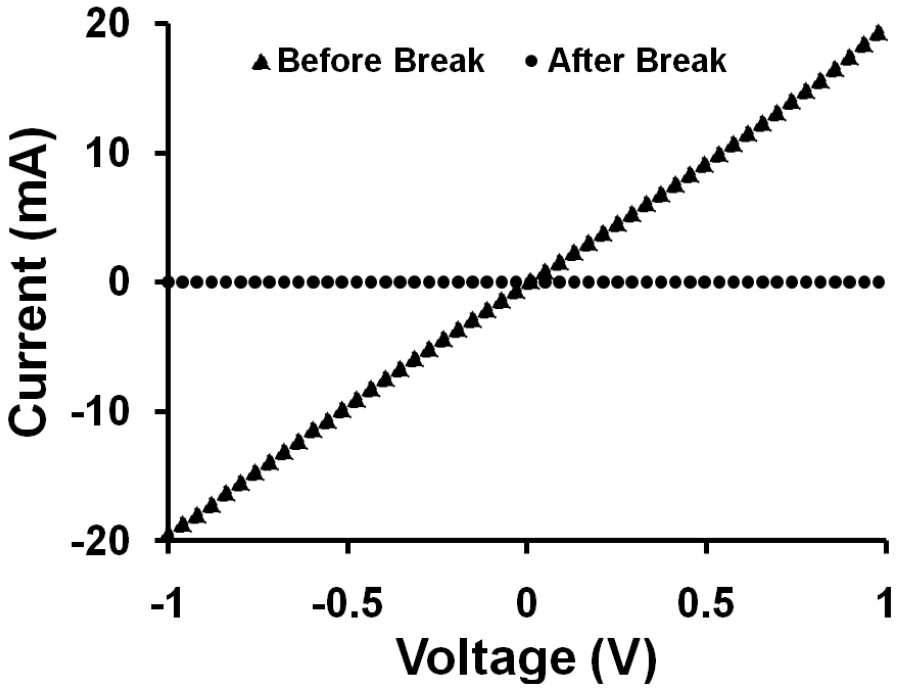

Figure 6.5 Shows the *I-V* plot before and after break in metallic lines due to electromigration. Reprinted with permission [209]

Conductance of the break-junctions is plotted in Figure 6.6. The graph shows that most of the electrodes with nano-gap in the range of 150 – 500 nm had a conductance only in the range of a few nS. This would be important parameter as conductance change can be more pronounced. The distribution of the nano-gaps that the most of the gaps were in the range of 100 – ~300 nm.

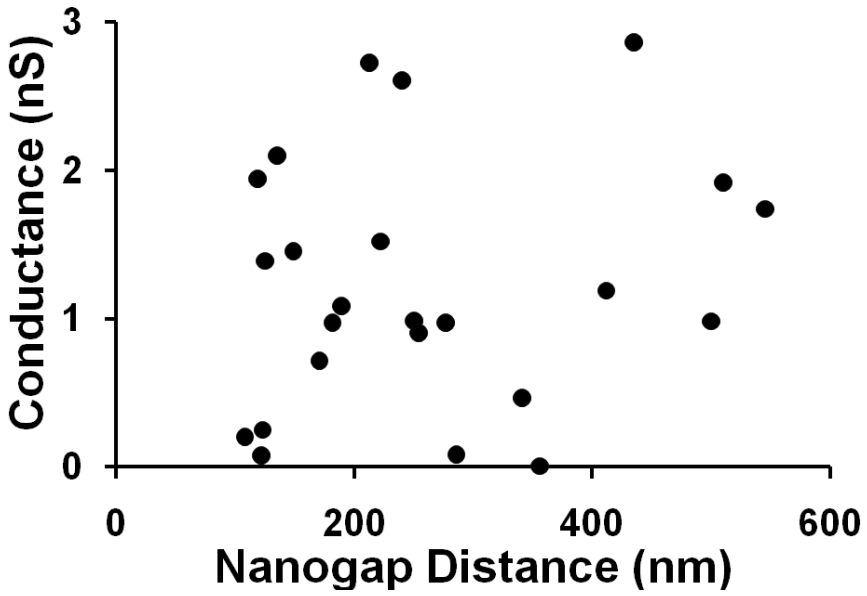

Figure 6.6 Shows the distribution of the devices according to conductance and nano-gap distance. The most of the gaps were in the range of 100 to ~300 nm. Reprinted with permission [209]

The results showed that the break-junctions were synthesized and characterized at each processing step. The FIB scratching process provided a rapid method to create nano-scratch in the metal lines. The FIB scratch provides very high electrical bottleneck to the flow of charge carriers. The high resistance and defects of the scratched part offered localized break in metal lines upon the applied voltage. During the FIB scratching process, the incident ions stroke the surface of the metal and transferred their energy to the electrons and atoms resulting in ejection of the atoms from the metal surface. The ions may also be penetrating the metal film and can also displace the atoms from their positions. Acceleration voltage applied during FIB scratching process plays a key role in these two competing processes.

The penetration of the ions into surface layer also depends on the penetration depth or range of the ions R_p. At depth D inside the material, if Gaussian curve is fitted to the distribution of the ions, it has the form of Equation (6.1).

$$\frac{Exp\left[-\left(D-R_p\right)^2 * \left(\Delta R_p\right)^2\right]}{2} \qquad (6.1)$$

Where ΔR_p is the Range Straggle. The number of atoms ejected from the surface depend on the energy of the striking ions. The FIB processes give typical yield of 1-10 atoms/ion. The yield also depends on the incident angle between ion beam and normal to the surface. Yield increases with $1/\cos\theta$, where θ is the incident angle [209]. The FIB milling process depends on milling current and time interval of the FIB process. As we only want to scratch the surface of the metal line, we first optimized our FIB process to desired feature. The complete removal of metal layer was not desired as it could cause defects in underlying SiO_2 layer which needs to be maintained plain and viable for possible immobilization of probe molecules. In one of our previous report, we defined the break-junctions with e-beam and these were used for electrical detection of selective target proteins using double-stranded DNA probe immobilized on the plain SiO_2 between the electrodes [210]. The reported method for the fabrication of break-junction can be used for a variety of similar applications, especially for genes or biomarker detection at very small concentrations [211].

The electromigration is the phenomenon in which external electric field is applied that caused a large current density in the metal lines. The electrons move under the influence of applied potential. If there is a defect in the metal, the momentum of the electrons is transferred to the defect. After certain time period, the momentum exchange becomes larger. The resulting build-up of a force causes the atoms to move away from the defect causing the breakdown of the metal line. In our process, FIB scratching not only provides a high resistance scratch on the metal line but it also introduces defects that directly help in breaking the metal line using electromigration. Although electromigration has been used by many research groups for synthesis of break-junctions [212, 213], the described method of producing nanogaps on FIB-scratched metal lines gave higher throughput and yield. We have successfully achieved

>60% yield of nanoscale devices as compared to previously reported yield of 10-20% [214, 215]. FIB to scratch the metal surface proves faster and less expensive way to fabricate break-junctions as compared with e-beam defined nanogaps.

6.4 Conclusions

We reported a rapid approach to create break-junctions. The FIB is used to only scratch the metal line followed by electromigration. The reported fabrication method has many advantage as compared with traditions methods like cost, time-to-manufacture, yield and spatial control of junctions' locations. Break-junctions fabricated with FIB can be used for biosensors and biomarker detection.

CHAPTER 7

FUTURE RESEARCH DIRECTIONS

7.1 Introduction

In this chapter, we are discussing future research directions and potential use of developed biosensing platforms. It includes the scope of more work that would supplement/complement the current research work.

7.2 Selective Detection of Epidermal Growth Factor Receptor (EGFR) using PPPF Nanopores

As thermal shrinking and PPPF deposition processes give rapid fabrication of solid-state nanopore, we plan to use nanopores for selective sensing of EGFR protein. We described earlier that EGFR protein is termed as “Cancer Protein” as it is over expressed in many tumor cells including breast cancer, lung cancer and prostate cancer. The expression levels of EGFR in cancer cells can be over 100 times higher than those in normal cells. The anti-EGFR aptamer has been used to selectively capture EGFR protien and tumor cells [216]. The nanopores with controlled surface composition can be synthesized using PPPF deposition process. The methacrylic acid monomer will be used during polymer deposition to have COO^- group on the nanopore walls [49]. Anti-EGFR aptamer will be tethered to COO^- surface groups using N-ethyl-N’-(3-dimethylaminopropyl) carbodiimide (EDC) and N-hydroxysuccinimide (NHS) chemistry [217]. Amine-Reactive O-acylysourea intermediate was formed by EDC but the intermediate is unstable due to susceptibility to hydrolysis in aqueous solution. The intermediate can be stabilized by using EDC/NHS mixture. Nanopore walls can be functionalized with amine-modified single strand DNA (ss-DNA) by incubated at 37 ^oC overnight. After DNA attachment the nanopore walls can be further functionalized with RNA aptamer which specifically binds to EGFR [218]. The final nanopore structure should looks like as shown in Figure 7.1.

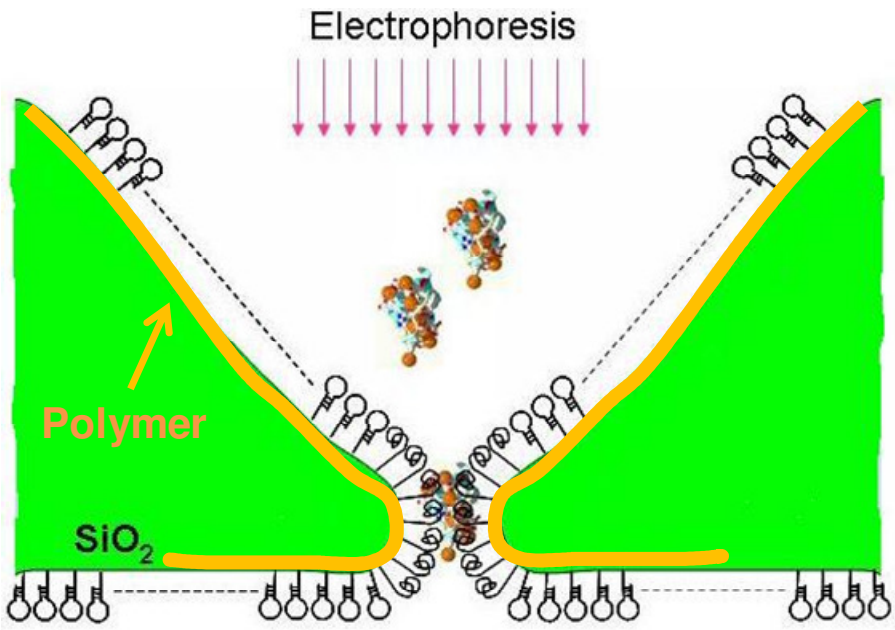

Figure 7.1 Shows the nanopore structure after PPPF deposition and anti-EGFR functionalization

We plan to use Bovine Serum Albumin (BSA) protein as a control. We believe as two proteins will try to translocate through the functionalized nanopore, different type of current blockage pulses are expected. The signals from translocations of EGFR protein will be differentiated from the BSA translocations because of specific binding of EGFR with RNA aptamers as shown in Figure 7.2. The GPU based real-time detection algorithms will be designed to automate the pulse detection process. The developed nanopore platform can perform selective detection of EGFR cancer protein at very low concentrations. The automatic detection algorithms such as moving average and adaptive threshold will increase the detection efficiency of target proteins.

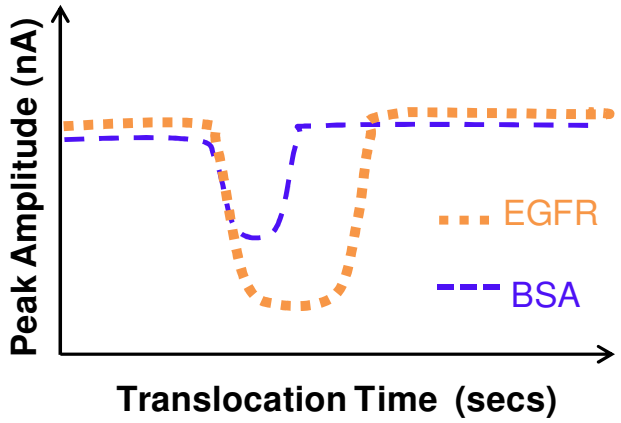

Figure 7.2 Shows the expected current translocations pulses from EGFR and BSA proteins through aptamer functionalized solid-state nanopore

7.3 Selective Enumeration of CD4+ T Lymphocytes

HIV/AIDS affects more than 30 million people all over the world. More that 67% of the affected people live in resource poor region of sub-Saharan Africa [219]. Anti-retrovial Therapy (ART) increases the quality of life of patients and global efforts increased the accessibility of such therapies to a large extent. Unfortunately, the lack of feasible diagnostic test to determine when to start ART hinders the effective use of treatment [219]. An important diagnostic procedure is to count the CD4+ T lymphocytes from the blood. Flow cytometers using laser induced fluorescence principles and laser light scattering are gold standards to count CD4+ cells [220, 221]. However the cost and technical requirements made these equipment inaccessible to resource poor regions. These optical equipment include lenses, filters, light sources, light detectors and CCDs which make them very expensive, bulky and fragile. These equipment also need regular maintenance. To deal with the problems, a cheap point of care (POC) microchip is needed for counting CD4+ cells.

Solid-state device having only one micropore would be used for selective counting of the CD4+ T lymphocytes. As the average diameter of the leukocytes is 13 um, the micropore have diameter comparable to 13 um will be used [178]. If the diameter of the micropore is larger

than 13, there are chances that more than two cells will try to pass through the pore at one time, which would produce error in final results. CD4+ cells will be mixed with PBS at different concentrations and run through the device. The schematic of the device is shown in Figure 7.3. The results will be compared with the standard flow cytometer. CD4+ cells over-express CD4 proteins on cell surface. Micropore chip is then functionalized with CD4+ antibody, and CD4+ cells are processed again. When the cells try to pass through the functionalized micropore, the antibody would attract the translocating cells. And the cell would give different translocation time and pulse amplitude. The pore diameter, flow rate and sampling time would be optimized.

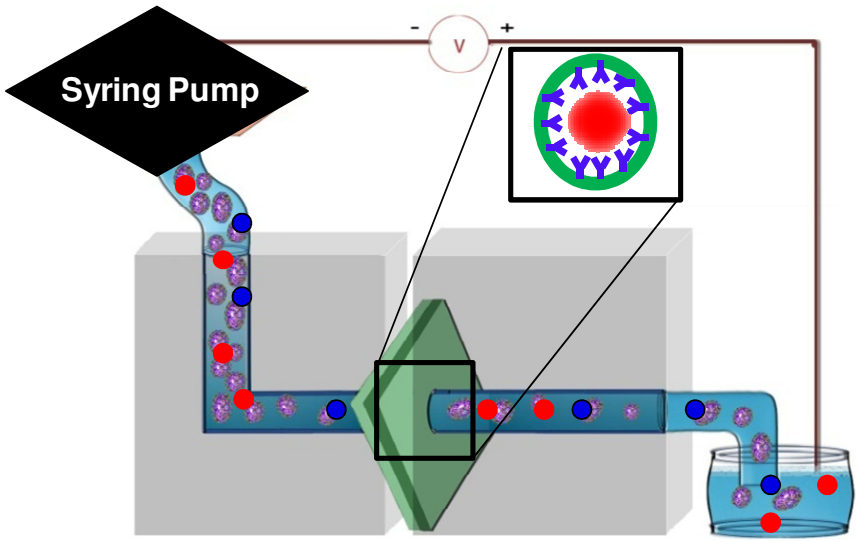

Figure 7.3 Shows the schematic for experimental setup that can be used for selective enumeration of CD4+ lymphocytes. The inset shows the translocation of a cell (red) through the micropore functionalized with CD4+ antibody

Once the device is characterized, the leukocytes would be separated from the human whole blood. The cells would be processed with functionalized and non-functionalized micropore chips to count the CD4+ cells. It is proposed that the CD4+ cells would give distinctive signals due to the antigen-antibody interactions. Upon accomplishment, the proposed device can be used for CD4+ T lymphocytes from the blood. The device would be very cheap and efficient. It would release burden from the health centers of resource poor regions.

7.4 Nano-Textured Surfaces for Efficient Cancer Detection and Cytology

We synthesized novel eggshell scaffolds having nanoporous and micro grass forest patterns as explained in Chapter 5. These surfaces gave 2 time increased laminin protein adsorption and 16 times more cell. The unique patterns have more available surface area due to texturing. We can use these eggshell scaffolds for efficient capture of primary human glioblastom (hGBM) cells. The EGFR protein is over expressed on many cancer cell types including hGBM [216]. Textured substrates can be functionalized with anti-EGFR RNA aptamers which bind very specifically with EGFR. As the chicken eggshell substrates give more protein adsorption, it is hypothesized that more of the anti-EGFR aptamers would bind with the textured substrates. For that PDMS channel will be made having nano-textured bottom surface as shown in Figure 7.4. The sample containing hGBM and healthy cells will be tested. I believe that novel substrates functionalized with anti-EGFR would give significantly more hGBM cells capture. These novel substrates will give efficient cancer cytology platform.

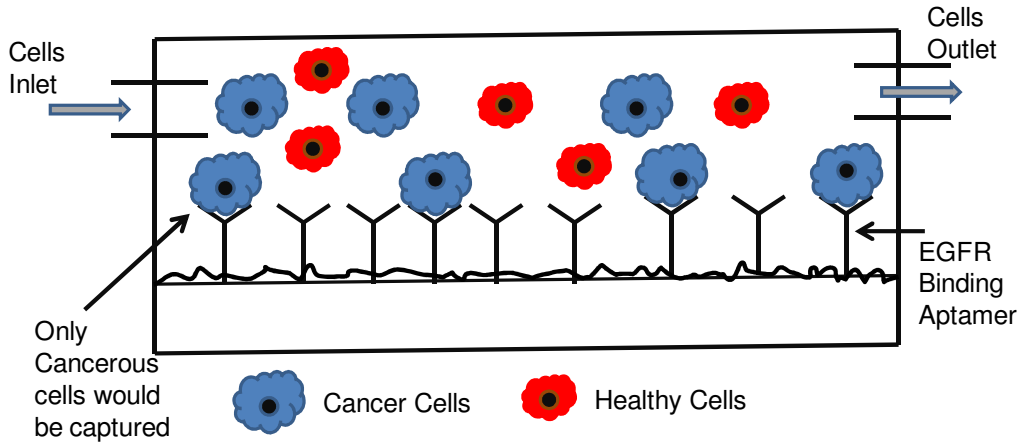

Figure 7.4 Shows the schematic for PDMS device having nano-textured bottom. The hGBM cells can be captured efficiently with aptamer functionalized, nano-textured surfaces

REFERENCES

1. Zimmer, C. and U. Wahnert, *Nonintercalating DNA-binding ligands: specificity of the interaction and their use as tools in biophysical, biochemical and biological investigations of the genetic material.* Progress in biophysics and molecular biology, 1986. **47**(1): p. 31.
2. Lacks, S. and R.D. Hotchkiss, *A study of the genetic material determining an enzyme activity in pneumococcus.* Biochimica et biophysica acta, 1960. **39**(3): p. 508-518.
3. Kabanov, A.V. and V.A. Kabanov, *DNA complexes with polycations for the delivery of genetic material into cells.* Bioconjugate chemistry, 1995. **6**(1): p. 7-20.
4. Zambryski, P., et al., *Ti plasmid vector for the introduction of DNA into plant cells without alteration of their normal regeneration capacity.* The EMBO journal, 1983. **2**(12): p. 2143.
5. Bekker-Jensen, S. and N. Mailand, *Assembly and function of DNA double-strand break repair foci in mammalian cells.* DNA repair. **9**(12): p. 1219-1228.
6. Watson, J.D. and F.H.C. Crick, *Molecular structure of nucleic acids.* Nature, 1953. **171**(4356): p. 737-738.
7. McGhee, J.D. and P.H. Von Hippel, *Formaldehyde as a probe of DNA structure. I. Reaction with exocyclic amino groups of DNA bases.* Biochemistry, 1975. **14**(6): p. 1281-1296.
8. Majewski, J., et al., *What can exome sequencing do for you?* Journal of Medical Genetics. **48**(9): p. 580-589.
9. Sanger, F., et al., *The nucleotide sequence of bacteriophage [phi] X174.* Journal of molecular biology, 1978. **125**(2): p. 225-246.
10. Shendure, J., et al., *Advanced sequencing technologies: methods and goals.* Nature Reviews Genetics, 2004. **5**(5): p. 335-344.
11. Swerdlow, H., et al., *Capillary gel electrophoresis for DNA sequencing:: Laser-induced fluorescence detection with the sheath flow cuvette.* Journal of Chromatography A, 1990. **516**(1): p. 61-67.
12. Shendure, J. and H. Ji, *Next-generation DNA sequencing.* Nature biotechnology, 2008. **26**(10): p. 1135-1145.
13. Bockelmann, U. and V. Viasnoff, *Theoretical study of sequence-dependent nanopore unzipping of DNA.* Biophysical journal, 2008. **94**(7): p. 2716-2724.
14. Cai, Q., et al., *Nanopore sculpting with noble gas ions.* Journal of Applied Physics, 2006. **100**: p. 024914.
15. Carbonaro, A. and L.L. Sohn, *A resistive-pulse sensor chip for multianalyte immunoassays.* Lab on a Chip, 2005. **5**(10): p. 1155-1160.
16. Chad Harrell, C., et al., *Resistive-pulse DNA detection with a conical nanopore sensor.* Langmuir, 2006. **22**(25): p. 10837-10843.
17. Chang, H., et al., *DNA-mediated fluctuations in ionic current through silicon oxide nanopore channels.* Nano Letters, 2004. **4**(8): p. 1551-1556.
18. Gierak, J., et al., *Sub-5nm FIB direct patterning of nanodevices.* Microelectronic Engineering, 2007. **84**(5-8): p. 779-783.
19. Gyurcsanyi, R.E., T. Vigassy, and E. Pretsch, *Biorecognition-modulated ion fluxes through functionalized gold nanotubules as a novel label-free biosensing approach.* Chemical Communications, 2003. **2003**(20): p. 2560-2561.
20. Harrell, C.C., et al., *DNA-nanotube artificial ion channels.* Journal of the American Chemical Society, 2004. **126**(48): p. 15646.
21. Chen, P., et al., *Probing single DNA molecule transport using fabricated nanopores.* Nano Letters, 2004. **4**(11): p. 2293-2298.

22. Cheng, M.M.C., et al., *Nanotechnologies for biomolecular detection and medical diagnostics.* Current Opinion in Chemical Biology, 2006. **10**(1): p. 11-19.
23. Cross, J.D., E.A. Strychalski, and H.G. Craighead, *Size-dependent DNA mobility in nanochannels.* Journal of Applied Physics, 2007. **102**: p. 024701.
24. Danelon, C., et al., *Fabrication and functionalization of nanochannels by electron-beam-induced silicon oxide deposition.* Nano Lett, 2005. **5**: p. 403-407.
25. Deen, W.M., *Hindered transport of large molecules in liquid filled pores.* AIChE Journal, 1987. **33**(9): p. 1409-1425.
26. DeGuzman, V.S., et al., *Sequence-dependent gating of an ion channel by DNA hairpin molecules.* Nucleic Acids Research, 2006. **34**(22): p. 6425-6437.
27. Firnkes, M., et al., *Electrically Facilitated Translocations of Proteins through Silicon Nitride Nanopores: Conjoint and Competitive Action of Diffusion, Electrophoresis, and Electroosmosis.* Nano Letters, 2010. **10**(6): p. 2162-2167.
28. Fologea, D., et al., *Detecting single stranded DNA with a solid state nanopore.* Nano Lett, 2005. **5**(10): p. 1905-1909.
29. Fologea, D., et al., *Slowing DNA translocation in a solid-state nanopore.* Nano Letters, 2005. **5**(9): p. 1734-1737.
30. Gadgil, V.J., et al., *Fabrication of nano structures in thin membranes with focused ion beam technology.* Surface & Coatings Technology, 2009. **203**(17-18): p. 2436-2441.
31. Gadzekpo, V.P.Y., et al., *Development of an ion-channel sensor for heparin detection.* Analytica Chimica Acta, 2000. **411**(1-2): p. 163-173.
32. Heng, J.B., et al., *Stretching DNA using the electric field in a synthetic nanopore.* Nano Letters, 2005. **5**(10): p. 1883.
33. Heng, J.B., et al., *Sizing DNA using a nanometer-diameter pore.* Biophysical journal, 2004. **87**(4): p. 2905-2911.
34. Howorka, S., S. Cheley, and H. Bayley, *Sequence-specific detection of individual DNA strands using engineered nanopores.* Nature biotechnology, 2001. **19**(7): p. 636-639.
35. Kircher, M. and J. Kelso, *High-throughput DNA sequencing-concepts and limitations.* Bioessays, 2010. **32**(6): p. 524-536.
36. Stoddart, D., et al., *Single-nucleotide discrimination in immobilized DNA oligonucleotides with a biological nanopore.* Proceedings of the National Academy of Sciences, 2009. **106**(19): p. 7702.
37. Wiggin, M., et al., *Nonexponential Kinetics of DNA Escape from [alpha]-Hemolysin Nanopores.* Biophysical journal, 2008. **95**(11): p. 5317-5323.
38. Pastoriza-Gallego, M., et al., *Urea denaturation of [alpha]-hemolysin pore inserted in planar lipid bilayer detected by single nanopore recording: Loss of structural asymmetry.* FEBS letters, 2007. **581**(18): p. 3371-3376.
39. Clarke, J., et al., *Continuous base identification for single-molecule nanopore DNA sequencing.* Nature nanotechnology, 2009. **4**(4): p. 265-270.
40. Flusberg, B.A., et al., *Direct detection of DNA methylation during single-molecule, real-time sequencing.* Nature methods, 2010. **7**(6): p. 461-465.
41. Schadt, E.E., S. Turner, and A. Kasarskis, *A window into third-generation sequencing.* Human molecular genetics, 2010. **19**(R2): p. R227.
42. Tsutsui, M., et al., *Identifying single nucleotides by tunnelling current.* Nature nanotechnology, 2010. **5**(4): p. 286-290.
43. Kasianowicz, J.J., et al., *Characterization of individual polynucleotide molecules using a membrane channel.* Proceedings of the National Academy of Sciences, 1996. **93**(24): p. 13770.
44. Branton, D., et al., *The potential and challenges of nanopore sequencing.* Nature biotechnology, 2008. **26**(10): p. 1146-1153.
45. Meller, A., et al., *Rapid nanopore discrimination between single polynucleotide molecules.* Proceedings of the National Academy of Sciences, 2000. **97**(3): p. 1079.

46. Zhao, Q., et al., *Stochastic sensing of biomolecules in a nanopore sensor array.* nanotechnology, 2008. **19**: p. 505504.
47. De Zoysa, R.S.S., et al., *Slowing DNA translocation through nanopores using a solution containing organic salts.* The Journal of Physical Chemistry B, 2009. **113**(40): p. 13332-13336.
48. Asghar, W., et al., *Shrinking of Solid-state Nanopores by Direct Thermal Heating.* Nanoscale Research Letters, 2011. **6**(1): p. 372.
49. Asghar, W., et al., *Pulsed plasma polymerization for controlling shrinkage and surface composition of nanopores.* Nanotechnology, 2011. **22**(28): p. 285304.
50. Biance, A.L., et al., *Focused ion beam sculpted membranes for nanoscience tooling.* Microelectronic Engineering, 2006. **83**(4-9): p. 1474-1477.
51. Billo, J.A., W. Asghar, and S.M. Iqbal. *An implementation for the detection and analysis of negative peaks in an applied current signal across a silicon nanopore*. 2011: SPIE.
52. Chang, H., et al., *Fabrication and characterization of solid-state nanopores using a field emission scanning electron microscope.* Applied Physics Letters, 2006. **88**: p. 103109.
53. Chang, H., et al., *DNA counterion current and saturation examined by a MEMS-based solid state nanopore sensor*. Vol. 8. 2006. 263-9.
54. Chen, P., et al., *Atomic layer deposition to fine-tune the surface properties and diameters of fabricated nanopores.* Nano Letters, 2004. **4**(7): p. 1333-1337.
55. Iqbal, S.M., D. Akin, and R. Bashir, *Solid-state nanopore channels with DNA selectivity.* nature nanotechnology, 2007. **2**(4): p. 243-248.
56. Iqbal, S.M. and R. Bashir, *Nanoelectronic-Based Detection for Biology and Medicine*. In Handbook of Automation, ed. S.Y. Nof. 2008: Springer Publishers.
57. Liu, Y. and S.M. Iqbal, *A mesoscale model of DNA interaction with functionalized nanopore.* Applied Physics Letters, 2009. **95**: p. 223701.
58. Ramachandran, A., et al., *Characterization of DNA-Nanopore Interactions by Molecular Dynamics.* American Journal of Biomedical Sciences, 2009. **1**(4): p. 344-351.
59. Venkatesan, B.M., et al., *Highly sensitive, mechanically stable nanopore sensors for DNA analysis.* Advanced Materials, 2009. **21**(27): p. 2771-2776.
60. Venkatesan, B.M., et al., *DNA Sensing Using Nanocrystalline Surface-Enhanced Al2O3 Nanopore Sensors.* Advanced Functional Materials, 2010. **20**(8): p. 1266-1275.
61. Li, J., et al., *DNA molecules and configurations in a solid-state nanopore microscope.* Nature materials, 2003. **2**(9): p. 611-615.
62. Li, J., et al., *Ion-beam sculpting at nanometre length scales.* Nature, 2001. **412**(6843): p. 166-169.
63. Park, S.R., H. Peng, and X.S. Ling, *Fabrication of nanopores in silicon chips using feedback chemical etching.* Small, 2007. **3**(1): p. 116.
64. Storm, A.J., et al., *Fabrication of solid-state nanopores with single-nanometre precision.* Nature materials, 2003. **2**(8): p. 537-540.
65. Wu, S., S.R. Park, and X.S. Ling, *Lithography-free formation of nanopores in plastic membranes using laser heating.* Nano Lett, 2006. **6**(11): p. 2571-2576.
66. Asghar, W., J.A. Billo, and S.M. Iqbal, *Solid State Nanopores for Selective Sensing of DNA*, in *Nanopores: Sensing and Fundamental Biological Interactions*, S.M. Iqbal and R. Bashir, Editors. 2011, Springer. p. 109-110.
67. Chen, P.H., et al., *The characteristic behavior of TMAH water solution for anisotropic etching on both silicon substrate and SiO2 layer.* Sensors and Actuators A: Physical, 2001. **93**(2): p. 132-137.
68. Sundaram, K.B., A. Vijayakumar, and G. Subramanian, *Smooth etching of silicon using TMAH and isopropyl alcohol for MEMS applications.* Microelectronic engineering, 2005. **77**(3): p. 230-241.
69. Zubel, I. and M. Kramkowska, *The effect of isopropyl alcohol on etching rate and roughness of (1 0 0) Si surface etched in KOH and TMAH solutions.* Sensors and Actuators A: Physical, 2001. **93**(2): p. 138-147.

70. Thong, J.T.L., W.K. Choi, and C.W. Chong, *TMAH etching of silicon and the interaction of etching parameters.* Sensors and Actuators A: Physical, 1997. **63**(3): p. 243-249.
71. Sundaram, K.B., A. Vijayakumar, and G. Subramanian, *Smooth etching of silicon using TMAH and isopropyl alcohol for MEMS applications.* Microelectronic Engineering, 2005. **77**(3-4): p. 230-241.
72. Choi, W.K., et al., *Characterisation of pyramid formation arising from the TMAH etching of silicon.* Sensors and Actuators A: Physical, 1998. **71**(3): p. 238-243.
73. Wu, M.Y., et al., *Formation of nanopores in a SiN/SiO membrane with an electron beam.* Applied Physics Letters, 2005. **87**: p. 113106.
74. Nilsson, J., et al., *Localized functionalization of single nanopores.* Advanced Materials, 2006. **18**(4): p. 427-431.
75. Siwy, Z., et al., *Protein biosensors based on biofunctionalized conical gold nanotubes.* Journal of the American Chemical Society, 2005. **127**(14): p. 5000-5001.
76. Siwy, Z., et al., *Conical-nanotube ion-current rectifiers: the role of surface charge.* J. Am. Chem. Soc, 2004. **126**(35): p. 10850-10851.
77. Siwy, Z., et al., *Asymmetric diffusion through synthetic nanopores.* Physical review letters, 2005. **94**(4): p. 48102.
78. Nilsson, J., et al., *Localized functionalization of single nanopores.* Advanced Materials, 2006. **18**(4): p. 427-431.
79. Meller, A., L. Nivon, and D. Branton, *Voltage-driven DNA translocations through a nanopore.* Physical review letters, 2001. **86**(15): p. 3435-3438.
80. Kim, Y.R., et al., *Nanopore sensor for fast label-free detection of short double-stranded DNAs.* Biosensors and Bioelectronics, 2007. **22**(12): p. 2926-2931.
81. Kim, M.J., et al., *Rapid fabrication of uniformly sized nanopores and nanopore arrays for parallel DNA analysis.* Advanced Materials, 2006. **18**(23): p. 3149-3153.
82. Umehara, S., et al., *Current rectification with poly-L-lysine-coated quartz nanopipettes.* Nano Lett, 2006. **6**(11): p. 2486-2492.
83. Wang, G., et al., *Electrostatic-gated transport in chemically modified glass nanopore electrodes.* J. Am. Chem. Soc, 2006. **128**(23): p. 7679-7686.
84. Wanunu, M. and A. Meller, *Chemically modified solid-state nanopores.* Nano Letters, 2007. **7**(6): p. 1580-1585.
85. Lopez-Lazaro, M., *A new view of carcinogenesis and an alternative approach to cancer therapy.* Molecular Medicine, 2010. **16**(3-4): p. 144.
86. Schwartz, G.K. and M.A. Shah, *Targeting the cell cycle: a new approach to cancer therapy.* Journal of clinical oncology, 2005. **23**(36): p. 9408.
87. Johnstone, R.W., A.A. Ruefli, and S.W. Lowe, *Apoptosis: A Link between Cancer Genetics and Chemotherapy.* Cell, 2002. **108**(2): p. 153-164.
88. Ghossein, R.A., S. Bhattacharya, and J. Rosai, *Molecular detection of micrometastases and circulating tumor cells in solid tumors.* Clinical cancer research, 1999. **5**(8): p. 1950-1960.
89. Paterlini-Brechot, P. and N.L. Benali, *Circulating tumor cells (CTC) detection: clinical impact and future directions.* Cancer letters, 2007. **253**(2): p. 180-204.
90. Futreal, P.A., et al., *A census of human cancer genes.* Nature Reviews Cancer, 2004. **4**(3): p. 177-183.
91. Klein, C.A., et al., *Genetic heterogeneity of single disseminated tumour cells in minimal residual cancer.* The Lancet, 2002. **360**(9334): p. 683-689.
92. Bernstein, L.R. and L.A. Liotta, *Molecular mediators of interactions with extracellular matrix components in metastasis and angiogenesis.* Current opinion in oncology, 1994. **6**(1): p. 106.
93. Liotta, L.A., *Cancer cell invasion and metastasis.* Scientific American, 1992. **266**(2): p. 54.

94. Cristofanilli, M., et al., *Circulating tumor cells: a novel prognostic factor for newly diagnosed metastatic breast cancer.* Journal of Clinical Oncology, 2005. **23**(7): p. 1420-1430.
95. Cristofanilli, M., et al., *Circulating tumor cells, disease progression, and survival in metastatic breast cancer.* New England Journal of Medicine, 2004. **351**(8): p. 781-791.
96. Budd, G.T., et al., *Circulating tumor cells versus imaging-predicting overall survival in metastatic breast cancer.* Clinical cancer research, 2006. **12**(21): p. 6403-6409.
97. Riethdorf, S., et al., *Detection of circulating tumor cells in peripheral blood of patients with metastatic breast cancer: a validation study of the CellSearch system.* Clinical cancer research, 2007. **13**(3): p. 920-928.
98. Hayes, D.F., et al., *Circulating tumor cells at each follow-up time point during therapy of metastatic breast cancer patients predict progression-free and overall survival.* Clinical Cancer Research, 2006. **12**(14): p. 4218-4224.
99. De Bono, J.S., et al., *Circulating tumor cells predict survival benefit from treatment in metastatic castration-resistant prostate cancer.* Clinical Cancer Research, 2008. **14**(19): p. 6302-6309.
100. Olmos, D., et al., *Circulating tumour cell (CTC) counts as intermediate end points in castration-resistant prostate cancer (CRPC): a single-centre experience.* Annals of oncology, 2009. **20**(1): p. 27.
101. Cohen, S.J., et al., *Relationship of circulating tumor cells to tumor response, progression-free survival, and overall survival in patients with metastatic colorectal cancer.* Journal of clinical oncology, 2008. **26**(19): p. 3213-3221.
102. Tol, J., et al., *Circulating tumour cells early predict progression-free and overall survival in advanced colorectal cancer patients treated with chemotherapy and targeted agents.* Annals of Oncology, 2010. **21**(5): p. 1006.
103. Kahn, H.J., et al., *Enumeration of circulating tumor cells in the blood of breast cancer patients after filtration enrichment: correlation with disease stage.* Breast cancer research and treatment, 2004. **86**(3): p. 237-247.
104. Pelkey, T.J., H.F. Frierson Jr, and D.E. Bruns, *Molecular and immunological detection of circulating tumor cells and micrometastases from solid tumors.* Clinical chemistry, 1996. **42**(9): p. 1369.
105. Rolle, A., et al., *Increase in number of circulating disseminated epithelial cells after surgery for non-small cell lung cancer monitored by MAINTRAC® is a predictor for relapse: a preliminary report.* World Journal of Surgical Oncology, 2005. **3**(1): p. 18.
106. Zieglschmid, V., C. Hollmann, and O. Böcher, *Detection of disseminated tumor cells in peripheral blood.* Critical Reviews in Clinical Laboratory Sciences, 2005. **42**(2): p. 155-196.
107. Krivacic, R.T., et al., *A rare-cell detector for cancer.* Proceedings of the National Academy of Sciences of the United States of America, 2004. **101**(29): p. 10501.
108. Racila, E., et al., *Detection and characterization of carcinoma cells in the blood.* Proceedings of the National Academy of Sciences, 1998. **95**(8): p. 4589.
109. Alix-Panabieres, C., S. Riethdorf, and K. Pantel, *Circulating tumor cells and bone marrow micrometastasis.* Clinical cancer research, 2008. **14**(16): p. 5013-5021.
110. Watkins, N., et al., *On a chip.* IEEE Pulse, 2011. **2**(6): p. 21-22.
111. Yu, M., et al., *Circulating tumor cells: approaches to isolation and characterization.* The Journal of Cell Biology, 2011. **192**(3): p. 373.
112. Hardingham, J.E., et al., *Immunobead-PCR: a technique for the detection of circulating tumor cells using immunomagnetic beads and the polymerase chain reaction.* Cancer research, 1993. **53**(15): p. 3455.
113. Witzig, T.E., et al., *Detection of circulating cytokeratin-positive cells in the blood of breast cancer patients using immunomagnetic enrichment and digital microscopy.* Clinical cancer research, 2002. **8**(5): p. 1085-1091.

114. Gauthier, L.R., et al., *Detection of circulating carcinoma cells by telomerase activity.* British journal of cancer, 2001. **84**(5): p. 631.
115. Allard, W.J., et al., *Tumor cells circulate in the peripheral blood of all major carcinomas but not in healthy subjects or patients with nonmalignant diseases.* Clinical Cancer Research, 2004. **10**(20): p. 6897-6904.
116. Balic, M., et al., *Comparison of two methods for enumerating circulating tumor cells in carcinoma patients.* Cytometry Part B: Clinical Cytometry, 2005. **68**(1): p. 25-30.
117. Zieglschmid, V., C. Hollmann, and O. BÃ¶cher, *Detection of disseminated tumor cells in peripheral blood.* Critical reviews in clinical laboratory sciences, 2005. **42**(2): p. 155-196.
118. Schuler, F. and G. Dolken, *Detection and monitoring of minimal residual disease by quantitative real-time PCR.* Clinica chimica acta, 2006. **363**(1-2): p. 147-156.
119. Zabaglo, L., et al., *Cell filtration-laser scanning cytometry for the characterisation of circulating breast cancer cells.* Cytometry Part A, 2003. **55**(2): p. 102-108.
120. Vona, G., et al., *Isolation by Size of Epithelial Tumor Cells: A New Method for the Immunomorphological and MolecularCharacterization of Circulating Tumor Cells.* American Journal of Pathology, 2000. **156**(1): p. 57.
121. Meng, S., et al., *Circulating tumor cells in patients with breast cancer dormancy.* Clinical cancer research, 2004. **10**(24): p. 8152-8162.
122. Nagrath, S., et al., *Isolation of rare circulating tumour cells in cancer patients by microchip technology.* Nature, 2007. **450**(7173): p. 1235-1239.
123. Biela, S.A., et al., *Different sensitivity of human endothelial cells, smooth muscle cells and fibroblasts to topography in the nanoâ€“micro range.* Acta biomaterialia, 2009. **5**(7): p. 2460-2466.
124. Biggs, M.J.P., R.G. Richards, and M.J. Dalby, *Nanotopographical modification: a regulator of cellular function through focal adhesions.* Nanomedicine: Nanotechnology, Biology and Medicine, 2010. **6**(5): p. 619-633.
125. Schmidt, R.C. and K.E. Healy, *Controlling biological interfaces on the nanometer length scale.* Journal of Biomedical Materials Research Part A, 2009. **90**(4): p. 1252-1261.
126. Devabhaktuni, S. and S. Prasad, *Nanotextured Organic Light Emitting Diode Based Chemical Sensor.* Journal of Nanoscience and Nanotechnology, 2009. **9**(11): p. 6299-6306.
127. Brunette, D.M., G.S. Kenner, and T.R.L. Gould, *Grooved titanium surfaces orient growth and migration of cells from human gingival explants.* Journal of dental research, 1983. **62**(10): p. 1045-1048.
128. Ricci, J.L., J.C. Grew, and H. Alexander, *Connectiveâ€ tissue responses to defined biomaterial surfaces. I. Growth of rat fibroblast and bone marrow cell colonies on microgrooved substrates.* Journal of Biomedical Materials Research Part A, 2008. **85**(2): p. 313-325.
129. Hamilton, D.W. and D.M. Brunette, *The effect of substratum topography on osteoblast adhesion mediated signal transduction and phosphorylation.* Biomaterials, 2007. **28**(10): p. 1806-1819.
130. Wang, P.Y., H.T. Yu, and W.B. Tsai, *Modulation of alignment and differentiation of skeletal myoblasts by submicron ridges/grooves surface structure.* Biotechnology and bioengineering, 2010. **106**(2): p. 285-294.
131. Martinez, E., et al., *Effects of artificial micro-and nano-structured surfaces on cell behaviour.* Annals of Anatomy-Anatomischer Anzeiger, 2009. **191**(1): p. 126-135.
132. Miller, D.C., et al., *Endothelial and vascular smooth muscle cell function on poly (lactic-co-glycolic acid) with nano-structured surface features.* Biomaterials, 2004. **25**(1): p. 53-61.
133. Tao, N.J., *Electron transport in molecular junctions.* Nature nanotechnology, 2006. **1**(3): p. 173-181.

134. Reed, M.A., et al., *The electrical measurement of molecular junctions.* Annals of the New York Academy of Sciences, 1998. **852**(1): p. 133-144.
135. Chen, F., et al., *Measurement of single-molecule conductance.* Annu. Rev. Phys. Chem., 2007. **58**: p. 535-564.
136. Zhou, C., et al., *Microfabrication of a mechanically controllable break junction in silicon.* Applied physics letters, 1995. **67**: p. 1160.
137. Iqbal, S.M., et al., *Direct current electrical characterization of ds-DNA in nanogap junctions.* Applied Physics Letters, 2005. **86**: p. 153901.
138. Park, H., et al., *Fabrication of metallic electrodes with nanometer separation by electromigration.* Applied Physics Letters, 1999. **75**: p. 301.
139. Bezryadin, A. and C. Dekker, *Nanofabrication of electrodes with sub-5 nm spacing for transport experiments on single molecules and metal clusters.* Journal of Vacuum Science & Technology B: Microelectronics and Nanometer Structures, 1997. **15**: p. 793.
140. Choi, J., K. Lee, and D.B. Janes, *Nanometer scale gap made by conventional microscale fabrication: step junction.* Nano Letters, 2004. **4**(9): p. 1699-1703.
141. Chang, H., et al., *DNA counterion current and saturation examined by a MEMS-based solid state nanopore sensor.* Biomedical Microdevices, 2006. **8**(3): p. 263-269.
142. Singer, A., et al., *Nanopore Based Sequence Specific Detection of Duplex DNA for Genomic Profiling.* Nano Letters, 2010. **10**(2): p. 738-742.
143. Smeets, R.M.M., et al., *Salt dependence of ion transport and DNA translocation through solid-state nanopores.* Nano Lett, 2006. **6**(1): p. 89-95.
144. Lo, C.J., T. Aref, and A. Bezryadin, *Fabrication of symmetric sub-5 nm nanopores using focused ion and electron beams.* Nanotechnology, 2006. **17**: p. 3264.
145. Lanyon, Y.H., et al., *Fabrication of nanopore array electrodes by focused ion beam milling.* Anal. Chem, 2007. **79**(8): p. 3048-3055.
146. Alers, G.B., et al., *Nitrogen plasma annealing for low temperature TaO films.* Applied Physics Letters, 1998. **72**: p. 1308.
147. King, J.C. and C. Hu, *Effect of low and high temperature anneal on process-induced damage of gate oxide.* Electron Device Letters, IEEE, 2002. **15**(11): p. 475-476.
148. Ferrari, A.C., et al., *Stress reduction and bond stability during thermal annealing of tetrahedral amorphous carbon.* Journal of Applied Physics, 1999. **85**: p. 7191.
149. Kaczer, B., et al., *The influence of elevated temperature on degradation and lifetime prediction of thin silicon-dioxide films.* Electron Devices, IEEE Transactions on, 2002. **47**(7): p. 1514-1521.
150. Lanxner, M., C.L. Bauer, and R. Scholz, *Evolution of hole size and shape in {100},{110} and {111} monocrystalline thin films of gold.* Thin Solid Films, 1987. **150**(2-3): p. 323-335.
151. Taylor, G.I. and D.H. Michael, *On making holes in a sheet of fluid.* Journal of Fluid Mechanics, 1973. **58**(04): p. 625-639.
152. Mathe, J., et al., *Orientation discrimination of single-stranded DNA inside the -hemolysin membrane channel.* Proceedings of the National Academy of Sciences, 2005. **102**(35): p. 12377.
153. Muthukumar, M. and C.Y. Kong, *Simulation of polymer translocation through protein channels.* Proceedings of the National Academy of Sciences, 2006. **103**(14): p. 5273.
154. Benson, D.E., et al., *Design of bioelectronic interfaces by exploiting hinge-bending motions in proteins.* Science, 2001. **293**(5535): p. 1641.
155. Bhattacharyya, D., et al., *A new class of thin film hydrogels produced by plasma polymerization.* Chemistry of materials, 2007. **19**(9): p. 2222-2228.
156. Chapman, C.L., et al., *Plasma polymer thin film depositions to regulate gas permeability through nanoporous track etched membranes.* Journal of Membrane Science, 2008. **318**(1-2): p. 137-144.
157. Beamson, G. and D. Briggs, *High resolution XPS of organic polymers: the Scienta ESCA300 database*. 1992: Wiley, Chichester [England]; New York.

158. Roy, S., et al., *Modeling gas flow through microchannels and nanopores.* Journal of Applied Physics, 2003. **93**: p. 4870.
159. Tang, Y.W., I. Szalai, and K.Y.U. Chan, *Diffusivity and conductivity of a primitive model electrolyte in a nanopore.* Molecular Physics, 2001. **99**(4): p. 309-314.
160. Siwy, Z., et al., *Conical-nanotube ion-current rectifiers: the role of surface charge.* Journal of the American Chemical Society, 2004. **126**(35): p. 10850.
161. Anderson, J.A., C.D. Lorenz, and A. Travesset, *General purpose molecular dynamics simulations fully implemented on graphics processing units.* Journal of Computational Physics, 2008. **227**(10): p. 5342-5359.
162. Schatz, M., et al., *High-throughput sequence alignment using Graphics Processing Units.* BMC bioinformatics, 2007. **8**(1): p. 474.
163. Hussong, R., et al., *Highly accelerated feature detection in proteomics data sets using modern graphics processing units.* Bioinformatics, 2009. **25**(15): p. 1937-1943.
164. Cao, Y., et al. *Towards chip-on-chip neuroscience: fast mining of neuronal spike streams using graphics hardware*. in *Proceedings of the 7th ACM international conference on Computing frontiers*. 2010. New York, USA: ACM.
165. Rafique, M.M., et al. *CellMR: A framework for supporting mapreduce on asymmetric cell-based clusters*. in *In Proceedings of the 23rd IEEE International Parallel and Distributed Processing Symposium (IPDPS)*. 2009. Rome, Italy: IEEE.
166. Rafique, M.M., A.R. Butt, and D.S. Nikolopoulos. *Designing accelerator-based distributed systems for high performance*. in *In the Proceedins of 10th IEEE/ACM International Symposium on Cluster, Cloud and Grid Computing*. 2010. Melbourne, Australia: IEEE.
167. Lewicki, M.S., *A review of methods for spike sorting: the detection and classification of neural action potentials.* Network-Computation in Neural Systems, 1998. **9**(4): p. R53-R78.
168. Hafeez, A., et al., *GPU-based real-time detection and analysis of biological targets using solid-state nanopores.* Medical and Biological Engineering and Computing, 2012: p. 1-11.
169. Invest, J.C., et al., *1. Paget S: The distribution of secondary growths in cancer of the breast.* Lancet, 1889. **1**: p. 571-572.
170. Kohn, E.C. and L.A. Liotta, *Molecular insights into cancer invasion: strategies for prevention and intervention.* Cancer Research, 1995. **55**(9): p. 1856.
171. Loberg, R.D., et al., *Detection and isolation of circulating tumor cells in urologic cancers: a review.* Neoplasia (New York, NY), 2004. **6**(4): p. 302.
172. Soria, J.C., et al., *The molecular detection of circulating tumor cells in bladder cancer using telomerase activity.* The Journal of urology, 2002. **167**(1): p. 352-356.
173. Fu, A.Y., et al., *A microfabricated fluorescence-activated cell sorter.* Nature biotechnology, 1999. **17**(11): p. 1109-1111.
174. Adams, A.A., et al., *Highly efficient circulating tumor cell isolation from whole blood and label-free enumeration using polymer-based microfluidics with an integrated conductivity sensor.* Journal of the American Chemical Society, 2008. **130**(27): p. 8633-8641.
175. Chang, W.C., L.P. Lee, and D. Liepmann, *Biomimetic technique for adhesion-based collection and separation of cells in a microfluidic channel.* Lab on a Chip, 2005. **5**(1): p. 64-73.
176. Terstappen, L.W., et al., *Peripheral blood tumor cell load reflects the clinical activity of the disease in patients with carcinoma of the breast.* International journal of oncology, 2000. **17**(3): p. 573.
177. Ghossein, R.A., et al., *Detection of prostatic specific membrane antigen messenger RNA using immunobead reverse transcriptase polymerase chain reaction.* Diagnostic Molecular Pathology, 1999. **8**(2): p. 59.

178. Watkins, N., et al., *A robust electrical microcytometer with 3-dimensional hydrofocusing.* Lab on a Chip, 2009. **9**(22): p. 3177-3184.
179. Asghar, W., et al., *Electrical Fingerprinting, 3D Profiling and Detection of Tumor Cells with Solid-state Micropores.* Lab on a Chip, 2012.
180. Biela, S.A., et al., *Different sensitivity of human endothelial cells, smooth muscle cells and fibroblasts to topography in the nano-micro range.* Acta Biomaterialia, 2009. **5**(7): p. 2460-2466.
181. Bacakova, L., et al., *Modulation of cell adhesion, proliferation and differentiation on materials designed for body implants.* Biotechnology Advances, 2011. **29**(6): p. 739-767.
182. Fujihara, K., M. Kotaki, and S. Ramakrishna, *Guided bone regeneration membrane made of polycaprolactone/calcium carbonate composite nano-fibers.* Biomaterials, 2005. **26**(19): p. 4139-4147.
183. Ferrari, A. and M. Cecchini, *Cells on Patterns.* Generating Micro and Nanopatterns on Polymeric Materials, 2011: p. 267-290.
184. Yang, F., et al., *Fabrication of nano-structured porous PLLA scaffold intended for nerve tissue engineering.* Biomaterials, 2004. **25**(10): p. 1891-1900.
185. Subramanian, A., U.M. Krishnan, and S. Sethuraman, *Fabrication of uniaxially aligned 3D electrospun scaffolds for neural regeneration.* Biomedical Materials, 2011. **6**(2): p. 025004.
186. Yoshii, T., et al., *Synthesis, characterization of calcium phosphates/polyurethane composites for weight bearing implants.* Journal of Biomedical Materials Research Part B: Applied Biomaterials, 2011. **00**(00): p. 000-000.
187. Soleymani, L., et al., *Programming the detection limits of biosensors through controlled nanostructuring.* Nature Nanotechnology, 2009. **4**(12): p. 844-848.
188. Dylewicz, R., et al., *Nanotexturing of GaN light-emitting diode material through mask-less dry etching.* Nanotechnology, 2011. **22**(5): p. 055301.
189. Wan, Y., et al., *Nanotextured substrates with immobilized aptamers for cancer cell isolation and cytology.* Cancer, 2011. **117**(20).
190. Park, T.H. and M.L. Shuler, *Integration of cell culture and microfabrication technology.* Biotechnology Progress, 2003. **19**(2): p. 243-253.
191. Yukna, R.A. and C.N. Yukna, *A 5 year follow up of 16 patients treated with coralline calcium carbonate (Biocoral™) bone replacement grafts in infrabony defects*.* Journal of clinical periodontology, 1998. **25**(12): p. 1036-1040.
192. Velich, N., et al., *Long-term results with different bone substitutes used for sinus floor elevation.* Journal of Craniofacial Surgery, 2004. **15**(1): p. 38.
193. Coughlin, M.J., J.S. Grimes, and M.P. Kennedy, *Coralline hydroxyapatite bone graft substitute in hindfoot surgery.* Foot & ankle international/American Orthopaedic Foot and Ankle Society [and] Swiss Foot and Ankle Society, 2006. **27**(1): p. 19.
194. Walsh, W.R., et al., *Response of a calcium sulfate bone graft substitute in a confined cancellous defect.* Clinical orthopaedics and related research, 2003. **406**(1): p. 228.
195. Liao, H., et al., *Tissue responses to natural aragonite (Margaritifera shell) implants in vivo.* Biomaterials, 2000. **21**(5): p. 457-468.
196. Anderson, J.R., et al., *Fabrication of topologically complex three-dimensional microfluidic systems in PDMS by rapid prototyping.* Analytical Chemistry, 2000. **72**(14): p. 3158-3164.
197. Duffy, D.C., et al., *Rapid prototyping of microfluidic systems in poly (dimethylsiloxane).* Analytical Chemistry, 1998. **70**(23): p. 4974-4984.
198. Dertinger, S.K.W., et al., *Gradients of substrate-bound laminin orient axonal specification of neurons.* Proceedings of the National Academy of Sciences, 2002. **99**(20): p. 12542.

199. Siva Rama Krishna, D., et al., *A novel route for synthesis of nanocrystalline hydroxyapatite from eggshell waste.* Journal of Materials Science: Materials in Medicine, 2007. **18**(9): p. 1735-1743.
200. Tsai, W.T., et al., *Development and Characterization of mesoporosity in eggshell ground by planetary ball milling.* Microporous and Mesoporous Materials, 2008. **111**(1-3): p. 379-386.
201. Tavangar, A., B. Tan, and K. Venkatakrishnan, *Synthesis of three-dimensional calcium carbonate nanofibrous structure from eggshell using femtosecond laser ablation.* Journal of Nanobiotechnology, 2011. **9**(1): p. 1.
202. losarczyk, A., et al., *New bone implant material with calcium sulfate and Ti modified hydroxyapatite.* Journal of Achievements in Materials and Manufacturing Engineering, 2010. **43**(1): p. 170-177.
203. Clark, P., et al., *Cell guidance by ultrafine topography in vitro.* Journal of Cell Science, 1991. **99**(1): p. 73.
204. Moreland, J. and J.W. Ekin, *Electron tunneling experiments using Nb-Sn "break" junctions.* Journal of applied physics, 1985. **58**(10): p. 3888-3895.
205. Widawsky, J.R., et al. *Conductance of Molecular Wires Measured by STM-Break Junction*. 2009.
206. Brugger, J., et al., *Silicon micro/nanomechanical device fabrication based on focused ion beam surface modification and KOH etching.* Microelectronic engineering, 1997. **35**(1): p. 401-404.
207. Reyntjens, S. and R. Puers, *A review of focused ion beam applications in microsystem technology.* Journal of Micromechanics and Microengineering, 2001. **11**: p. 287.
208. Schmuki, P. and L.E. Erickson, *Selective high-resolution electrodeposition on semiconductor defect patterns.* Physical review letters, 2000. **85**(14): p. 2985-2988.
209. Asghar, W., et al., *Rapid Nanomanufacturing of Metallic Break Junctions Using Focused Ion Beam Scratching and Electromigration.* Journal of Manufacturing Science and Engineering, 2010. **132**(3): p. 030911.
210. Ramachandran, P.P., S.M. Christensen, and S.M. Iqbal. *Electronic detection of selective proteins using non antibody-based CMOS chip*. in *Life Science Systems and Applications Workshop, LiSSA, IEEE/NIH* 2009: IEEE.
211. Noor, M.R., et al., *Electrical detection of single-base DNA mutation using functionalized nanoparticles.* Applied Physics Letters, 2009. **95**: p. 073703.
212. Demarchi, D., et al., *Electrothermal modelling for EIBJ nanogap fabrication.* Electrochimica Acta, 2009. **54**(25): p. 6003-6009.
213. Liu, B., et al., *Controllable nanogap fabrication on microchip by chronopotentiometry.* Electrochimica acta, 2005. **50**(15): p. 3041-3047.
214. Mahapatro, A.K., S. Ghosh, and D.B. Janes, *Nanometer scale electrode separation (nanogap) using electromigration at room temperature.* Nanotechnology, IEEE Transactions on, 2006. **5**(3): p. 232-236.
215. Park, J., et al., *Coulomb blockade and the Kondo effect in single-atom transistors.* Nature, 2002. **417**(6890): p. 722-725.
216. Wan, Y., et al., *Surface-immobilized aptamers for cancer cell isolation and microscopic cytology.* Cancer research, 2010. **70**(22): p. 9371.
217. Ali, M., et al., *Modifying the surface charge of single track-etched conical nanopores in polyimide.* Nanotechnology, 2008. **19**: p. 085713.
218. Chu, T.C., et al., *Aptamer: toxin conjugates that specifically target prostate tumor cells.* Cancer research, 2006. **66**(12): p. 5989.
219. Kitahata, M.M., et al., *Effect of early versus deferred antiretroviral therapy for HIV on survival.* New England Journal of Medicine, 2009.
220. Miller, V., et al., *CD4 lymphocyte count as a predictor of the duration of highly active antiretroviral therapy-induced suppression of human immunodeficiency virus load.* The Journal of infectious diseases, 1999. **180**(2): p. 530-533.

221. Lepri, A.C., et al., *When to start highly active antiretroviral therapy in chronically HIV-infected patients: evidence from the ICONA study.* Aids, 2001. **15**(8): p. 983.

BIOGRAPHICAL INFORMATION

Waseem Asghar was born in Sahiwal, Pakistan. He completed his high school at Cadet College Hasan Abdal Attock, Pakistan. He moved to Lahore for his undergrad education. He received his Bachelor in Science (B.Sc.) degree in Electrical Engineering from University of Engineering and Technology, Lahore, Pakistan in September 2007. After his engineering degree, he joined Faculty of Engineering at University of Central Punjab Lahore as lecturer from 2007 to 2008. He moved to Arlington, Texas for his Ph.D. He is a doctoral candidate under the supervision of Dr. Samir M. Iqbal in the Department of Electrical Engineering, University of Texas at Arlington (UTA), Texas, USA since September of 2008. Since joining graduate school at UTA in 2008, he is working as Graduate Research Associate in Nano-Bio Laboratory, Nanotechnology Research and Teaching Facility at UTA. He was awarded couple of prestigious fellowships including “I Mentor Fellowship” which requires advising undergrad students in their research projects. He was also selected for “Nanofab Best Graduate Student Award” for year 2012. This award is given to only one graduate student every year based on his/her research contribution to scientific community. He has published about 20 peer reviewed journal and conference publications. He has also contributed one book chapter published in 'Nanopores: Sensing and Fundamental Biological Interactions' (Eds. R. Bashir, S. Iqbal); ISBN: 978-1-4419-8251-3, Springer, NY, USA (2011). He is serving as a guest editor for “Micro and Nanosystems (MNS)” Journal. His areas of interest are cancer diagnosis and prognosis, nano-bio sensors, nano-textured surfaces, proteomics and biomaterials.